The Thesis Committee for Blake Elliott Simon
Certifies that this is the approved version of the following thesis:

Analysis of Model Equations for Lucassen Waves and Other Nonlinear Fractional Diffusive Waves

APPROVED BY

SUPERVISING COMMITTEE:

Mark F. Hamilton, Supervisor

John M. Cormack

Michael R. Haberman

Analysis of Model Equations for Lucassen Waves and Other Nonlinear Fractional Diffusive Waves

by

Blake Elliott Simon

THESIS

Presented to the Faculty of the Graduate School of

The University of Texas at Austin

in Partial Fulfillment

of the Requirements

for the Degree of

MASTER OF SCIENCE IN ENGINEERING

THE UNIVERSITY OF TEXAS AT AUSTIN

December 2020

To my parents, Karen and Steve Simon.

Acknowledgments

There are many people that have assisted me at The University of Texas at Austin. I would like to specifically thank a few of my important mentors here. First and foremost, I want to thank my adviser, Dr. Mark Hamilton, for sharing his passion for acoustics and constantly inspiring me as a prospective researcher. Thanks to Dr. Charles Bradley for bringing nonlinear Lucassen waves to our attention. I would like to thank Dr. Marcia Isakson for mentoring me as an undergraduate student at the Applied Research Laboratories and exposing me to the field of acoustics. I would also like to thank Dr. Michael Haberman and Dr. Preston Wilson for their dedication to me and the other students in the acoustics program. Thanks to Dr. John Cormack for his insight and feedback. Thank you to the Applied Research Laboratories at UT Austin for financially supporting my graduate education with the Chester M. McKinney Graduate Fellowship in Acoustics. The support given by The University of Texas at Austin with the Thrust 2000 Uniden Endowed Graduate Fellowship in Engineering was also instrumental in this work. Finally, I would like to thank my parents. They have always supported and loved me and none of this would be possible without them.

Analysis of Model Equations for Lucassen Waves and Other Nonlinear Fractional Diffusive Waves

Blake Elliott Simon, M.S.
The University of Texas at Austin, 2020

Supervisor: Mark F. Hamilton

This thesis investigates the nature of "fractional waves", i.e., physical processes that are described by a fractional derivative. Fractional calculus is an extension of traditional calculus to include integrals and derivatives of non-integer order. In fractional wave models, the fractional derivative is used to model attenuation and dispersion during waveform propagation. Fractional wave equations interpolate between the diffusion (heat) equation and the conventional wave equation. A specific physical example of a fractional wave is the Lucassen wave. Lucassen waves are longitudinal disturbances that propagate along an elastic layer coupled to a fluid half-space and are modeled by a fractional wave equation with a fractional time derivative. The equation describing the propagation of linear Lucassen waves is derived in this work. Nonlinear Lucassen waves were first described by Kappler et al. [J. Kappler, S. Shrivastava, M. F. Schneider, and R. R. Netz, "Nonlinear fractional waves at elastic interfaces," Phys. Rev. Fluids **2**, 114804 (2017)] and have been connected to the mechanical wave that accompanies the electric action potential

during nerve pulse propagation. Two evolution equations for progressive nonlinear Lucassen waves are derived in the present work from the equation of Kappler et al. These evolution equations are of reduced differential order and are thus easier to solve numerically. The evolution equations are also used to obtain additional physical insight. An alternate evolution equation for nonlinear Lucassen waves that accounts for viscosity in the interface is derived as well. This evolution equation is more accurate for propagation along interfaces with viscosity that is significant compared with that of the liquid half-space to which it is coupled. The possibility of vertical tangent (shock) formation is explored for general fractional wave evolution equations. The evolution equations derived in this work are transformed into the intrinsic coordinates originally introduced by Hammerton and Cirghton [P. W. Hammerton and D. G. Crighton, "Overturning of nonlinear acoustic waves. Part 1: A general method," J. Fluid Mech. **252**, 585–599 (1993)] in order to analyze the propagation of nonlinear waveforms with large gradients approximating shock fronts. It is shown that the evolution equation that accounts for viscosity in the interface is the most stable for numerical calculations of the propagation of these nonlinear waveforms with large gradients.

Table of Contents

List of Tables

List of Figures

Chapter 1

Introduction

1.1 How the brain led to fractional diffusive waves

In April of 2018 an article by Douglas Fox titled *The Brain, Reimagined* was published by Scientific American.[1] Based primarily on the work of Ichiji Tasaki, Thomas Heimburg, and Matthias Schneider, this article promulgates the groundbreaking idea that nerve cells communicate with mechanical pulses, not electric ones as conventionally thought. The subtitle of the article reads, "The physicists who have revived experiments from 50 years ago say nerve cells communicate with mechanical pules, not electric ones."[1] The prevailing theory of nerve pulse propagation since the 1950s is the Hodgkin-Huxley model,[2] which is purely electrochemical in nature, and for which Hodgkin and Huxley were awarded the Nobel Prize in Physiology or Medicine in 1963. To suggest that nerve cell communication is primarily mechanical in nature, as Fox does in the subtitle of his Scientific American article, is truly a disruptive hypothesis for the neurophysiology community. Although this main point of the Scientific American article was described as a slight misrepresentation by a researcher that works closely with Schneider,[3] the controversy had already begun. In Fox's article, one neurobiologist says[1] "It strikes me as this business that physicists do, saying, 'We can approximate this cow as a single point'" to

describe their perceived superiority complex of the physicist that strides into a different field telling other scientists how they ought to think.

As researchers in the field of acoustics, we were very intrigued by the possibility that a nonlinear mechanical wave may play a significant role in nerve cell communication. The seemingly most well-known thermodynamically-based model for nerve impulse propagation has been proposed by Heimburg and Jackson,[4] which explicitly accounts for the mechanical variations in the neural axon membranes. However, the idea that the coupling of the mechanical wave to the action potential is important for understanding nerve pulse propagation goes back to at least Kaufman in 1989.[5] While reaction to the Scientific American article by some within the neuroscience community has been, at best, skeptical, what is indisputable is that some kind of mechanical disturbance accompanies the electric action potential, which has been demonstrated in experiments over the last few decades.[6–11] The question is what role, if any, does this mechanical wave play in cell-to-cell communication. Acousticians are not qualified to take a side in this debate, but perhaps our perspective can provide better physical understanding of the mechanical wave in nerve axons.

This leads us to the experimental work of Schneider, Griesbauer, and Shrivastava among others[12–17] which investigates the propagation of mechanical waves on Dipalmitoylphosphatidylcholine (DPPC) lipid monolayers. These lipid interfaces have physical properties similar to those of biological membranes of the kind found in nerve axons.[14] It was shown that the mechanical waves in these layers share attributes with neural action potentials, such as the

all-or-none principle[14,18] and the collision and annihilation of pulses traveling in opposite directions.[16] Coupling between the action potential, the mechanical surface wave on the cell membrane, and the pressure wave in the nerve axoplasm has also been considered by Engelbrecht.[19]

A derivation from first principles of a mathematical model describing a nonlinear mechanical wave that propagates along elastic interfaces, such as the DPPC monolayer, was presented by Kappler, Shrivastava, Schneider and Netz.[20] This wave is identified as a Lucassen wave, because the linear behavior of the wave was first described in the frequency domain by Lucassen,[21,22] who was interested in the properties of a wide variety of surface waves. Nonlinear Lucassen waves are thought to possibly be the mechanical waves in nerve axons because they have propagation speeds that are comparable to those of nerve pulse propagation in unmyelinated axons.[14,16,20] They also exhibit an amplitude threshold phenomenon, both analytically and experimentally, that is analogous to the aforementioned all-or-none principle of action potentials.[18,20]

The Lucassen wave is one example of a class of solutions for a linear, semi-infinite, viscoelastic medium;[23] more specifically, the Lucassen wave is a longitudinal disturbance that propagates along interfaces formed by an elastic layer that is coupled to an incompressible viscous liquid. These surface waves are said to be longitudinal because unlike waves on the free surface of a liquid or Rayleigh waves in an elastic half-space, the particle motion adjacent to the surface is approximately parallel to the surface rather than following an elliptical orbit.[24]

What is perhaps most interesting about the Lucassen wave is that its linear propagation is not described by a traditional wave equation. While the equation for Lucassen waves possesses a space derivative of second order as in a traditional wave equation, its time derivative is of fractional order. The fractional derivative is an extension of the ordinary derivative to non-integer order. For Lucassen waves, the fractional derivative describes the attenuation and dispersion associated with their propagation. Fractional waves of this type, including the Lucassen wave, are strongly damped on the scale of a wavelength, and as a result they are sometimes called "fractional diffusive waves."[25]

Therefore what started in the brain led to Lucassen waves, which exposed us to the nontraditional world of fractional calculus. Fractional calculus is not a new field, as it was first posited by Leibniz in the 17th century,[26] but it has remained in relative obscurity until a few decades ago, when it was used with increasing frequency in a number of different applications (see Chap. 2). Fractional calculus has been used in the field of acoustics to model loss of waves exhibiting power-law attenuation.[27] In fact, a book by Holm[28] that is entirely on the subject of power-law attenuated waves was published recently. However, much of the focus in this thesis is directed towards fractional waves.[25,29] Unlike models for acoustic waves with power-law attenuation, fractional wave equations lack a d'Alembertian term and thus the fractional derivative is directly responsible for propagation (whereas for power-law attenuated waves, the fractional derivative is *only* responsible for attenuation and dispersion.) A

significant purpose of this thesis is to expose the field of acoustics to fractional wave theory and try to interpret the propagation of fractional waves from an acoustician's point of view. A variety of unique and unintuitive properties of fractional wave propagation are explored in the present work. It would not be surprising in the near future to witness a significant increase in the number of modeling applications using fractional calculus for wave motion. Indeed, at the December 2020 virtual meeting of the Acoustical Society of America there will be a special session titled Fractional Calculus Models of Compressional and Shear Waves for Medical Ultrasound.

Another goal of this thesis is to increase the understanding of nonlinear Lucassen wave propagation as a contribution to the debate surrounding mechanical waves and nerve pulse propagation. Perhaps Lucassen wave theory will one day help explain the contribution of mechanical disturbances to signaling in nerve axons.

1.2 Order of chapters

Chapter 2 introduces a formalism for fractional calculus, and the nature of fractional waves is explored in this chapter. Multiple different analytic solutions and interpretations for the compound fractional wave equation are presented as well.

Chapter 3 analyzes specifically Lucassen waves. A derivation of the model equation for Lucassen waves, as well as for Lucassen waves with interface viscosity included, is presented. The nonlinear model equation for

Lucassen waves developed recently by Kappler et al.[20] is recast as two different nonlinear evolution equations of reduced differential order. A separate nonlinear evolution equation is derived that includes interface viscosity. The benefits of each of these new evolution equations is discussed.

In Chap. 4, the evolution equations presented in Chap. 3 are analyzed to understand the behavior of these equations subject to very nonlinear conditions. It is known that the lossless nonlinear Burgers equation, ubiquitous in the study of nonlinear acoustics, under certain conditions, namely low loss, allows for vertical tangent formation in the waveform (shock formation), but it is not clear if this can occur with fractional wave models. Therefore the possibility of vertical tangent formation in fractional waves is discussed from both numerical and analytical points of view in Chap. 4.

Chapter 5 presents a brief conclusion summarizing our results. Finally, Appendix A describes various numerical algorithms used in the present work and Appendix B offers an interpretation of the possibility of shock formation based on fractional wave evolution equations by generalizing an analysis due to Whitham.[30]

Chapter 2

Fractional calculus and fractional wave equations

2.1 Introduction to fractional derivatives

Derivatives are essential components of mathematical models for physical processes that depend on variations in any properties of the system under consideration. Traditional derivatives are conventionally regarded as local, discrete operations on continuous functions. Taking the first, second, third, or higher derivative of a continuous function is well defined. However, what if one were to take the 0.5th derivative of a function? One of the patriarchs of the Western formalism of calculus, Gottfried Wilhelm Leibniz, pondered this very question in a letter to Guillaume de l'Hôpital in 1695. Leibniz said that the operation itself leads to a paradox, but also noted, "There will seem to be some very useful consequences one day of these paradoxes, because there is hardly a paradox without utility."[26]

There is more than one way to validly extend the meaning of discrete derivatives to fractional order. This fact partly explains the paradoxical nature of the fractional derivative operation alluded to by Leibniz. In the study of wave physics, such as physical acoustics, fractional derivatives are often used to

capture dispersion relationships; for example, they are convenient for modeling waves in media with power-law attenuation in the time domain.[28] Waves of this type exhibit attenuation and dispersion that conveniently satisfies the Kramers-Kronig causality relations.[31]

Dispersion relations are usually expressed in the frequency domain and, because of this, the most fundamental definition for the fractional derivative of order η in the study of wave physics is also expressed in the frequency domain:

$$\mathcal{F}_\omega \left\{ \frac{d^\eta f(t)}{dt^\eta} \right\} = (-i\omega)^\eta \mathcal{F}_\omega \{f(t)\} \tag{2.1}$$

where $\mathcal{F}_\omega$ is the Fourier transform operator. This definition is entirely consistent with that of the traditional discrete derivative. Equation (2.1) is written for a time fractional derivative, though a fractional derivative in space would look the same albeit in wavenumber space as opposed to the frequency domain. The Caputo fractional derivative definition[32] is used exclusively throughout the present work:

$${}_a^C D_t^\eta f(t) = \frac{1}{\Gamma(m-\eta)} \int_a^t \frac{d^m f(t')/d(t')^m}{(t-t')^{\eta+1-m}} dt' \ , \quad m = \lceil \eta \rceil \tag{2.2}$$

where Γ is the Gamma function. Equation (2.2) is a convolution integral that can be thought of as a generalization of the Cauchy integration formula at negative fractional order.[25] Equations (2.2) and (2.1) are consistent for bounded, continuous functions only if the lower integration limit is given by $a = -\infty$. However, for any transient waveform this lower bound can be chosen as the beginning of the dynamical event, i.e., $a = t_0 = 0$. In the present work

the lower limit $a = 0$ is chosen, and the following convention is employed:

$$\frac{d^\eta f(t)}{dt^\eta} \triangleq {}_0^C D_t^\eta f(t) \tag{2.3}$$

The arbitrary choice of the lower integration limit a in Eq. (2.2) is another hint of the paradoxical nature of the fractional derivative operation referred to by Leibniz. There is no rigorous requirement for the choice of a; in this work $a = 0$ by choice, but it depends on the physical problem of interest. This, combined with the various inconsistent, yet valid-in-their-own-right, definitions of other types of fractional derivatives[25,33] can lead to paradoxical results. But as Leibniz also noted, there are very useful consequences in physical modeling when fractional derivatives are employed correctly.

2.2 Linear fractional differential equation models

The first example of a linear "fractional model" to be considered is the fractional version of the simple harmonic oscillator (SHO). The conventional SHO with natural frequency ω_2 is described by the following second-order linear differential equation:

$$\frac{\partial^2 x}{\partial t^2} + \omega_2^2 x = 0 \tag{2.4}$$

Extended to fractional order, with a fractional natural frequency ω_η, the differential equation for the fractional harmonic oscillator has the form

$$\frac{\partial^\eta x}{\partial t^\eta} + \omega_\eta^2 x = 0 \tag{2.5}$$

Notice that ω_η must have dimensions of $\mathrm{T}^{-\eta/2}$ in terms of time T, which is why the different subscript is used. The general solution of Eq. (2.5) is in terms of Mittag-Leffler functions, which are generalizations of the ordinary exponential function:[25]

$$x(t) = C_1 E_\eta(-\omega_\eta^2 t^\eta) + C_2 t E_{\eta,2}(-\omega_\eta^2 t^\eta) \tag{2.6}$$

where $E_\eta(z)$ and $E_{\eta,\beta}(z)$ are the Mittag-Leffler functions of one and two parameters, respectively,[34,35] and are defined by

$$E_\eta(z) = \sum_{n=0}^{\infty} \frac{z^n}{\Gamma(\eta n + 1)} \tag{2.7a}$$

$$E_{\eta,\beta}(z) = \sum_{n=0}^{\infty} \frac{z^n}{\Gamma(\eta n + \beta)} \tag{2.7b}$$

Returning to Eq. (2.5), let a particle be at $x(0) = 1$ initially at rest such that $\dot{x}(0) = 0$, where the dot indicates the first derivative with respect to time. Because $E_\eta(0) = 1$ it can be shown that $C_1 = 1$ and $C_2 = 0$. The solution of this initial-value problem is thus

$$x(t) = E_\eta(-\omega_\eta^2 t^\eta) \tag{2.8}$$

For $\eta = 2$ (i.e., the conventional SHO) in Eq. (2.5), Eq. (2.8) reduces to $x(t) = E_2(-\omega_\eta^2 t^2) = \cos \omega_\eta t$ as expected. Plots of Eq. (2.8) for different values of η are shown in Fig. 2.1. For $\eta < 2$ the oscillations of the particle $x(t)$ decrease in amplitude as t increases. For $\eta = 1$ the system returns to steady state quickly; in fact, for $\eta = 1$ Eq. (2.8) is exactly the same as the solution for a critically damped harmonic oscillator under the same initial conditions because

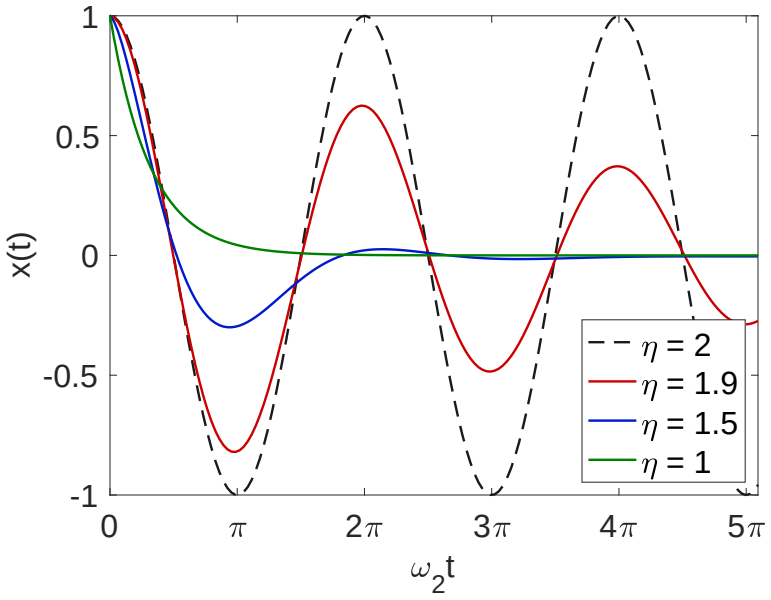

Figure 2.1: Plot of Eq. (2.8) for different values of η. For $\eta = 2$, the solution is the same as that for a conventional SHO. The time axis is scaled by the natural frequency for the conventional SH0 ω_2.

$E_1(-\omega_\eta^2 t) = e^{-\omega_\eta^2 t}$. Thus according to Eq. (2.8) the fractional harmonic oscillator interpolates between critically damped and undamped harmonic motion for $1 \leq \eta \leq 2$. Or stated in another way, Eq. (2.5) is a composite dynamical relation that interpolates between amplitude decay and oscillation.[36]

2.3 The fractional diffusion-wave equation

A natural extension of the fractional harmonic oscillator is the linear fractional wave equation. Begin with the conventional wave equation in 1D

(this work will consider exclusively 1D motion) with constant wave speed c:

$$\frac{\partial^2 \xi}{\partial t^2} = c^2 \frac{\partial^2 \xi}{\partial x^2} \tag{2.9}$$

For a solution of the form

$$\xi = \xi_0 e^{i(\tilde{k}x - \omega t)} \tag{2.10}$$

where $\tilde{k}$ is the wavenumber, possibly complex, and ω is the angular frequency, the dispersion relation associated with Eq. (2.9) is

$$\tilde{k}^2 = k^2 = \frac{\omega^2}{c^2} \tag{2.11}$$

where k is the real part of the complex wavenumber $\tilde{k}$ (i.e., $k = \mathrm{Re}\{\tilde{\mathrm{k}}\}$). In the case of Eq. (2.11) the complex wavenumber is purely real so $k = \tilde{k}$. Now consider the fractional wave equation in 1D where the time derivative has a fractional order $1 \leq \eta \leq 2$ and the coefficient c_η is a physical parameter with dimensions of $\mathrm{L} \cdot \mathrm{T}^{-\eta/2}$ in terms of length L and time T:

$$\frac{\partial^\eta \xi}{\partial t^\eta} = c_\eta^2 \frac{\partial^2 \xi}{\partial x^2} \tag{2.12}$$

In Eq. (2.12) for $\eta = 2$ the wave equation [Eq. (2.9)] is recovered. For $\eta = 1$ Eq. (2.12) becomes the diffusion equation (also called the heat equation). In general the x derivative can also have its own fractional order. However, only space derivatives of integer order are encountered in the present work. For a solution in the form of Eq. (2.10) the dispersion relation associated with Eq. (2.12) is

$$\tilde{k}^2 = -\frac{(-i\omega)^\eta}{c_\eta^2} \tag{2.13}$$

Many types of fractional wave equations arise from first deriving a dispersion relation like Eq. (2.13) in the frequency domain and then finding the equivalent time-domain fractional wave equation [like Eq. (2.12)].[20] If $\alpha = \mathrm{Im}\{\tilde{\mathrm{k}}\}$ is defined to be the attenuation coefficient, then $\tilde{k} = k(\omega) + i\alpha(\omega)$ where

$$k(\omega) = \sin(\eta\pi/4)\frac{\omega^{\eta/2}}{c_\eta} \qquad \alpha(\omega) = \cos(\eta\pi/4)\frac{\omega^{\eta/2}}{c_\eta} \tag{2.14}$$

Fractional waves are attenuated with distance over a length scale on the order the wavelength: $\alpha\lambda = 2\pi\alpha/k = 2\pi\cot(\eta\pi/4)$, which corresponds to $\frac{40\pi}{\ln 10}\cot(\eta\pi/4)$ dB per wavelength. The inherent attenuation and dispersion over a specific propagation distance is a defining feature of a fractional wave. Because of their intrinsically dissipative nature, fractional waves for which $1 < \eta < 2$ with a traditional space derivative of second order are referred to as "fractional diffusive waves"[29] and "superdiffusion processes."[37] For $0 < \eta < 1$ the physical systems are referred to as "subdiffusion processes."[37] For particles randomly dispersed in some medium, superdiffusion corresponds to particle displacement that increases in variance over time, while subdiffusion corresponds to particle displacement that decreases in variance over time. In the present work, subdiffusion processes ($\eta < 1$) are not considered. The phase speed of the wave c_{ph} is determined by the relation $c_{\mathrm{ph}} = \omega/k$. By using Eq. (2.14) the phase speed of fractional waves can be written as

$$c_{\mathrm{ph}}(\omega) = c_\eta \csc(\eta\pi/4)\omega^{1-\eta/2} \tag{2.15}$$

The dispersion relations, Eqs (2.14) and (2.15), satisfy the Kramers-Kronig

relations when $0 < \eta < 2$ [this is seen by substitution of Eqs (2.14) and (2.15) into the equations of Table II in Waters[31] while letting $\omega_0 \to \infty$.]

Fractional calculus is also used for modeling wave propagation in lossy media. It can be used to model viscoelastic materials or other materials that exhibit properties between those of an ideal solid or liquid.[38] For example, the fractional generalization of the Kelvin-Voigt constitutive stress-strain relation with a time constant τ_σ leads to the following dispersion relation:[39]

$$\tilde{k}^2 - \frac{\omega^2}{c^2} + (-i\tau_\sigma\omega)^\eta \tilde{k}^2 = 0 \tag{2.16}$$

with the equivalent time domain representation

$$\frac{\partial^2 \xi}{\partial x^2} - \frac{1}{c^2}\frac{\partial^2 \xi}{\partial t^2} + \tau_\sigma^\eta \frac{\partial^\eta}{\partial t^\eta}\frac{\partial^2 \xi}{\partial x^2} = 0 \tag{2.17}$$

It is important to note that Eq. (2.17) is not a "fractional wave equation" of the canonical form of Eq. (2.12). Equation (2.17) implies a fractional time derivative to model the energy loss and dispersion exhibited by an acoustic wave with power-law attenuation.[28] The distinguishing feature is that Eq. (2.17) possesses a d'Alembertian wave operator (the first two terms) whereas (2.12) does not. Therefore, propagation of a fractional wave is associated with the fractional operator itself, whereas propagation for an acoustic wave with power-law attenuation is associated with the d'Alembertian operator. The fractional derivative in Eq. (2.17) is a correction term that accounts for attenuation and dispersion of the otherwise traditional wave. Behavior of this sort can be observed for acoustic waves propagating in a medium with multiple relaxation processes.[28,40]

2.3.1 Solution using normal mode analysis

The general solution of the conventional wave equation, Eq. (2.9), is

$$\xi(x,t) = f(x-ct) + g(x+ct) \tag{2.18}$$

where $f(z)$ and $g(z)$ are arbitrary functions that represent a rightward and leftward traveling wave, respectively. The functions $f(z)$ and $g(z)$ are chosen to satisfy the initial and boundary conditions of the problem. An analytic solution as simple as Eq. (2.18) is not available for the fractional wave equation, Eq. (2.12), when η is not an integer.

To consider possible solutions of Eq. (2.12) one must specify initial and boundary conditions:

$$\xi(0,t) = \xi(L,t) = 0, \qquad t > 0 \tag{2.19a}$$

$$\xi(x,0) = \xi_0(x), \qquad 0 < x < L \tag{2.19b}$$

$$\frac{\partial \xi}{\partial t}(x,0) = \xi_{t,0}(x), \qquad 0 < x < L \tag{2.19c}$$

Equations (2.19a)–(2.19c) may describe a string of length L that is fixed at both ends, with an initial shape $\xi_0(x)$ and initial velocity distribution $\xi_{t,0}(x)$. The initial and boundary conditions, Eqs. (2.19a)–(2.19c), for the fractional wave equation, Eq. (2.12), nearly describes a Cauchy problem,[25] except that in a Cauchy problem the domain for x is infinite ($-\infty < x < \infty$) rather than finite.

The problem can be solved using the method of normal modes.[41] To begin, separation of variables is employed with the separation constant k^2. Let

$\xi(x,t) = X(x)T(t)$, in which case Eq. (2.12) becomes

$$\frac{1}{c_\eta^2 T}\frac{d^\eta T}{dt^\eta} = \frac{1}{X}\frac{d^2 X}{dx^2} = -k^2 \tag{2.20}$$

Equation (2.20) separates into the following two ordinary differential equations:

$$\frac{d^2 X}{dx^2} + k^2 X = 0 \tag{2.21a}$$

$$\frac{d^\eta T}{dt^\eta} + k^2 c_\eta^2 T = 0 \tag{2.21b}$$

Equation (2.21a) is of the same form as Eq. (2.4). It is a linear homogenous second-order differential equation with the following general solution:

$$X(x) = A_1 \cos kx + A_2 \sin kx \tag{2.22}$$

with arbitrary constants $A_{1,2}$. Equation (2.21b) is equivalent to the fractional harmonic oscillator problem solved previously, the solution of which is Eq. (2.6). Based on that result, the general solution of Eq. (2.21b) with $1 \leq \eta \leq 2$ is

$$T(t) = B_1 E_\eta(-\omega_\eta^2 t^\eta) + B_2 t E_{\eta,2}(-\omega_\eta^2 t^\eta) \tag{2.23}$$

where $B_{1,2}$ are arbitrary constants, and $\omega_\eta^2 = k^2 c_\eta^2$ is referred to as the fractional natural frequency (squared) that was first introduced in Eq. (2.5). Using (2.19a) it can be shown that $A_1 = 0$ and

$$\sin kL = 0 \tag{2.24}$$

which is an eigenvalue problem that is satisfied for

$$k = \frac{\pi}{L},\ \frac{2\pi}{L},\ \ldots,\ \frac{n\pi}{L} \tag{2.25}$$

Therefore the general solution of Eq. (2.12) is

$$\xi_n(x,t) = X(x)T(t) = \sin\frac{n\pi x}{L}\left[a_n E_\eta(-\omega_{\eta,n}^2 t^\eta) + b_n t E_{\eta,2}(-\omega_{\eta,n}^2 t^\eta)\right] \tag{2.26}$$

such that

$$\begin{aligned}\xi(x,t) &= \sum_{n=1}^{\infty}\xi_n(x,t) \\ &= \sum_{n=1}^{\infty}\sin\frac{n\pi x}{L}\Big[a_n E_\eta(-\omega_{\eta,n}^2 t^\eta) + b_n t E_{\eta,2}(-\omega_{\eta,n}^2 t^\eta)\Big]\end{aligned} \tag{2.27}$$

where $a_n = A_2B_1$ and $b_n = A_2B_2$. Now the initial conditions, Eq. (2.19b) and (2.19c), are applied, beginning with the displacement:

$$\xi(x,0) = \sum_{n=1}^{\infty} a_n \sin\frac{n\pi x}{L} \tag{2.28}$$

Orthogonality of the eigenfunctions yields

$$a_n = \frac{2}{L}\int_0^L \xi_0(x)\sin\frac{n\pi x}{L}\,dx \tag{2.29}$$

$$b_n = -\frac{2}{L\omega_{\eta,n}^2}\int_0^L \xi_{t,0}(x)\sin\frac{n\pi x}{L}\,dx \tag{2.30}$$

where Eq. (2.30) is obtained using the following identity:

$$\frac{d}{dt}\left[tE_{\eta,2}(-\omega_{\eta,n}^2 t^\eta)\right]_{t=0} = -\omega_{\eta,n}^2 E_\eta(-\omega_{\eta,n}^2 t^\eta)\Big|_{t=0} = -\omega_{\eta,n}^2 \tag{2.31}$$

As an example consider a waveform initially at rest [$\xi_{t,0}(x) = 0$] in the shape of a Gaussian function centered at $x = L/2$ with unit amplitude and a radius x_r:

$$\xi_0(x) = e^{-\frac{1}{2}\left(\frac{x-L/2}{x_r}\right)^2} \tag{2.32}$$

This is the traditional "plucked-string" scenario. By inspection $b_n = 0$ because the string begins at rest. With Eq. (2.32) substituted into Eq. (2.29), a_n can be determined and substituted into Eq. (2.27). Since the coefficients a_n cannot be expressed in terms of elementary functions for this choice of $\xi_0(x)$ they are calculated numerically. The fractional coefficient in Eq. (2.12) c_η is chosen to be unity. Figure 2.2 displays plots of Eq. (2.27) with $x_r = L/20$ for $\eta = 1$ (left column, blue), $\eta = 3/2$ (middle column, green), and $\eta = 2$ (right column, red).

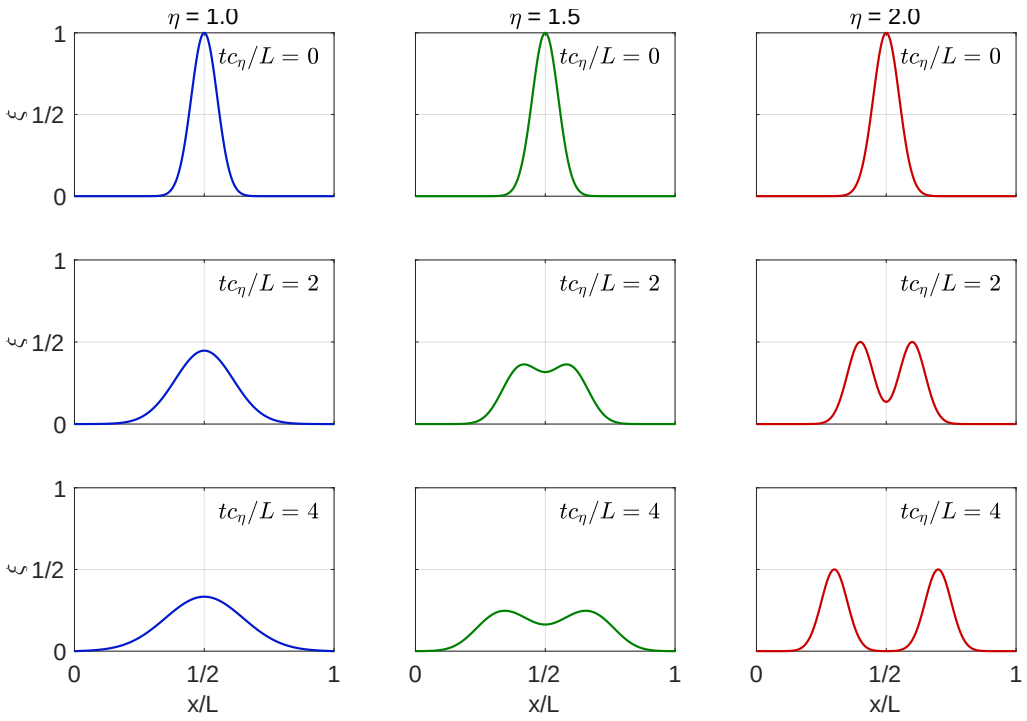

Figure 2.2: Plots of Eq. (2.27) at different times for different values of η with initial displacement given by Eq. (2.32) ($x_r = L/20$) and zero initial velocity. The time coordinate is scaled by the quantity L/c_η.

As mentioned previously, for $\eta = 1$ Eq. (2.12) becomes the diffusion equation. In the left column of Fig. 2.2, as time increases the initial Gaussian profile is reduced in amplitude and increased in length. For $\eta = 2$ Eq. (2.12) becomes the conventional wave equation, Eq. (2.9). In the right column of Fig. 2.2 the initial Gaussian waveform separates into two identical Gaussian waveforms, having exactly half the amplitude of the initial waveform, that propagate in opposite directions, which is consistent with the general solution of the wave equation, Eq. (2.38). Finally, for $\eta = 3/2$ Eq. (2.12) is in between the diffusion equation and the wave equation. In the middle column of Fig. 2.2 the initial waveform separates into two waveforms that both propagate and diffuse as a function of time. The diffusive waves neither separates completely into two independent waveforms as in the right column, nor do their peak amplitudes remain centered at $x = 0$ as in the left column. This suggests that the pulses remain coupled for $t > 0$. Any other value of η would lead to behavior that is closer to wave propagation or diffusion depending on whether η is closer to 2 or 1, respectively. This dualistic feature is why Eq. (2.12) is sometimes referred to as a fractional "diffusion-wave" equation.

2.3.2 Solutions using Green's functions

The fractional wave equation, Eq. (2.12), can also be solved using Green's functions. Green's functions have also been used to solve the conventional linear wave equation with additional fractional derivative terms modeling power law attenuation.[42] Rather than being restricted to initial conditions

for a system released from rest, the problem can be formulated such that the waveform originates from a boundary with the disturbance moving away from the boundary in the $+x$ direction. In this case the boundary condition serves as a source function for Eq. (2.12):

$$\xi(0,t) = S(t), \qquad t > 0 \tag{2.33a}$$

$$\xi(\infty,t) = 0, \qquad t > 0 \tag{2.33b}$$

$$\xi(x,0) = \frac{\partial \xi}{\partial t}(x,0) = 0, \qquad x > 0 \tag{2.33c}$$

where $S(t)$ is the source function. The formulation of Eqs. (2.33a)–(2.33c) is called a signaling problem for a fractional partial differential equation.[25] A solution is found by convolving the source condition $S(t)$ on the boundary at $x = 0$ with the appropriate Green's function $G_\eta(x,t)$, where the subscript η indicates the order of the fractional time derivative:

$$\xi(x,t) = \int_0^t G_\eta(x, t-t')S(t')\,dt' \tag{2.34}$$

For analytical simplicity, the source function incorporated in the boundary condition is chosen to be a Gaussian function centered at a time $t_0 > 0$ with unit amplitude and a radius t_r:

$$S(t) = e^{-\frac{1}{2}\left(\frac{t-t_0}{t_r}\right)^2} \tag{2.35}$$

The value t_0 is chosen such that $S(t)$ is negligibly small at the boundary $t = 0$ to avoid any significant jumps after the initial condition (2.33c) is enforced.

For $\eta = 1$, Eq. (2.12) once again is the diffusion equation, and the Green's function for this case is

$$G_1(x,t) = \frac{x}{c_1\sqrt{4\pi t^3}} e^{-x^2/4c_1^2 t} \tag{2.36}$$

A solution of the diffusion equation is obtained by substituting the Green's function in Eq. (2.34). With the initial condition given by Eq. (2.35), Eq. (2.34) cannot be evaluated analytically in terms of elementary functions.

For $\eta = 2$, Eq. (2.12) is the conventional wave equation. The appropriate Green's function is a delta function, and therefore evaluation of the convolution integral in Eq. (2.34) is trivial. The Green's function and corresponding solution, respectively, for the conventional wave equation are

$$G_2(x,t) = \delta(t - x/c_2) \tag{2.37}$$

$$\xi(x,t) = e^{-(t-x/c_2-t_0)^2} \tag{2.38}$$

When η is not an integer, the associated Green's function $G_\eta(x,t)$ is not as simple as Eq. (2.36) or (2.37). The general Green's function for $0 < \eta \leq 2$ is[25,43]

$$G_\eta(x,t) = \frac{1}{t}\sum_{n=1}^{\infty} \frac{(-1)^n |x/(c_\eta t^{\eta/2})|^n}{n!\ \Gamma(-\eta n/2)} \tag{2.39}$$

Equation (2.39) can be calculated numerically, although the infinite series converges very slowly, often requiring asymptotic expressions to evaluate the series.[25] No analytic solution for the convolution integral in Eq. (2.34) with $G_\eta(x,t)$ defined by Eq. (2.39) has been reported; therefore, Eq. (2.34) must also be evaluated numerically when η is a noninteger .

Figure 2.3 shows solutions of Eq. (2.12) subject to conditions (2.33a)–(2.33c) with $S(t)$ given by Eq. (2.35) for $\eta = 1$ (left column, blue), $\eta = 3/2$ (middle column, green), and $\eta = 2$ (right column, red), and with $c_\eta = 1$ m/sec in all cases as before. For the diffusion process in Fig. 2.3, $\eta = 1$

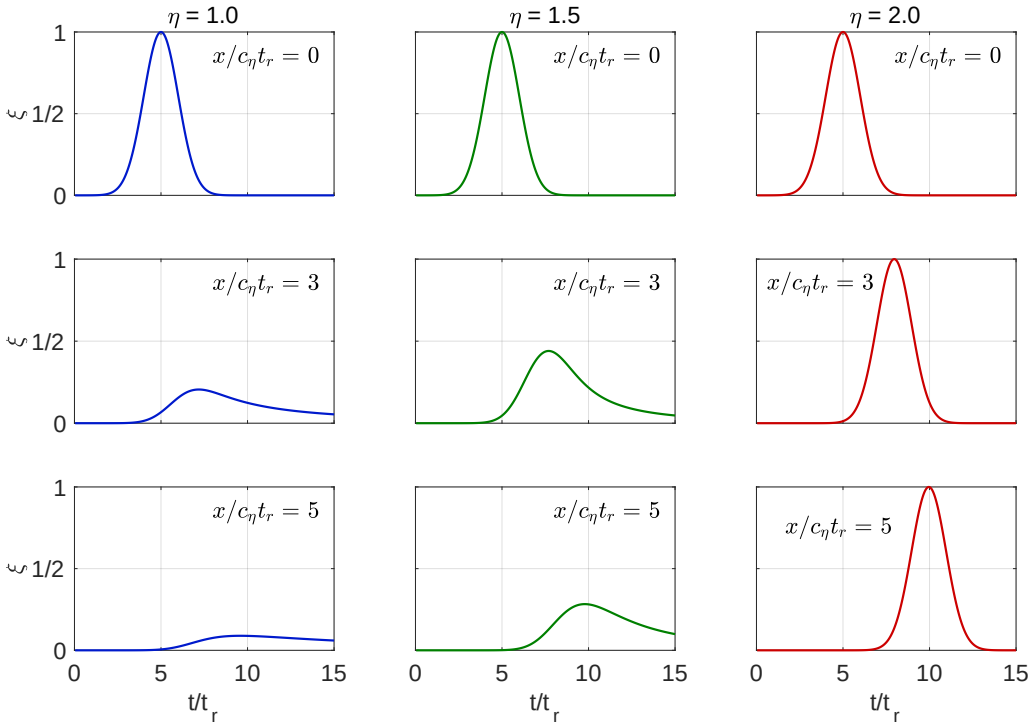

Figure 2.3: Plots of Eq. (2.34) at different distances for different values of η with the source function described by Eq. (2.35) with $t_0 = 5$ secs and $t_r = 1$ sec. The Green's functions used in Eq. (2.34) are determined in general by Eq. (2.39), although Eqs. (2.36) and (2.37) were used for $\eta = 1$ and $\eta = 2$, respectively. The distance is scaled by the quantity $c_\eta t_r$.

(left column), the initial Gaussian pulse is attenuated rapidly as it spreads out in space. For wave propagation, $\eta = 2$ (right column), the Gaussian

pulse propagates unattenuated with speed $c_2 = 1$ m/sec. For $\eta = 3/2$ (middle column), the waveform exhibits features of both propagation and diffusion. As the waveform propagates, it both attenuates and increases in duration. This result is consistent with the the previous analysis summarized in Fig. 2.2.

2.4 Conclusion

Solutions of the fractional wave equation provide insights similar to those revealed by solutions of the fractional harmonic oscillator equation. In the fractional wave equation, the fractional time derivative interpolates between diffusion and wave propagation while for the fractional harmonic oscillator, the fractional time derivative interpolates between undamped and critically damped motion. In addition to the applications already discussed (modeling lossy harmonic motion and modeling attenuation and dispersion in viscoelastic material), fractional calculus is also used to model diffusion in complex systems,[44] attenuation and dispersion in media with multiple relaxation processes,[40] electrodiffusion in nerve cells,[45] dynamics in financial markets,[46] and propagation of nonlinear shallow water waves.[47] With fractional calculus still considered a relatively new modeling tool for complex physical systems, it is not unreasonable to expect a dramatic increase in its applications in the near future.

Chapter 3

Lucassen waves

3.1 Introduction

This chapter considers a specific physical example of a fractional diffusive wave, the Lucassen wave. First described by Lucassen[21,22] in the frequency domain, these waves are primarily longitudinal disturbances that can propagate along viscoelastic interfaces formed by an elastic layer that is coupled to an incompressible viscous liquid. The Lucassen wave is one example of a class of surface wave solutions for a semi-infinite viscoelastic medium bounded by a 2D viscoelastic interface medium.[23] As mentioned in Chap. 1, Lucassen wave theory may explain the mechanical disturbance that accompanies the action potential in nerve axons.

3.2 Derivation of linear Lucassen wave equation

While energy-based variational methods have been used to succinctly derive dispersion relations for water surface waves,[48] a Newtonian based derivation is more convenient for the class of interface waves to which Lucassen waves belong. The beginning of this derivation follows the work of Dias et al.,[49] while the conclusion follows the logic of the original derivation by Lucassen.[21] Kap-

pler et al.[23] also derived a class of solutions for viscoelastic surface waves which includes Lucassen waves.

Let the spatial coordinates of the system be (x, y, z) with $z < 0$ defining the half-space occupied by a viscous liquid and let $z = 0$ be the location of the interface in equilibrium. It is assumed that the impedance presented by the half-space $z > 0$ at the interface with the viscous liquid is sufficiently negligible that the upper medium can be considered a vacuum. The plane strain assumption is made, i.e., motion will only be considered in two dimensions, (x, z), corresponding to propagation in the x direction.

Now let the particle velocities in the x and z directions be $u(x, z, t)$ and $w(x, z, t)$, respectively. Helmholtz decomposition in 2D is employed to express the velocities as

$$u = \frac{\partial \Phi}{\partial x} - \frac{\partial A}{\partial z} \tag{3.1a}$$

$$w = \frac{\partial \Phi}{\partial z} + \frac{\partial A}{\partial x} \tag{3.1b}$$

where Φ and A are the curl-free component and divergence-free component of the velocity field, also referred to as the velocity potential and stream function, respectively. Additionally, let ρ and μ be the density and dynamic viscosity of the liquid, respectively.

Incompressible flow is assumed and the amplitude of the velocity field is assumed to be small enough that the linearized Navier-Stokes equations can be used. These assumptions lead to the following equations:

$$\frac{\partial u}{\partial x} + \frac{\partial w}{\partial z} = 0 \tag{3.2}$$

$$\frac{\partial u}{\partial t} = -\frac{\partial p}{\partial x} + \frac{\mu}{\rho}\left(\frac{\partial^2 u}{\partial x^2} + \frac{\partial^2 u}{\partial z^2}\right) \tag{3.3a}$$

$$\frac{\partial w}{\partial t} = -\frac{\partial p}{\partial z} + \frac{\mu}{\rho}\left(\frac{\partial^2 w}{\partial x^2} + \frac{\partial^2 w}{\partial z^2}\right) - g \tag{3.3b}$$

where g in Eq. (3.3b) is the magnitude of the acceleration due to gravity. Equation (3.2) is the incompressible flow condition that follows from the continuity equation, and Eqs. (3.3a) and (3.3b) are the x and z components, respectively, of the linearized Navier-Stokes equations for an incompressible liquid. From Eqs. (3.1a) and (3.1b), Eqs. (3.2), (3.3a), and (3.3b) are satisfied when the following relations hold:

$$\frac{\partial A}{\partial t} = \frac{\mu}{\rho}\left(\frac{\partial^2 A}{\partial x^2} + \frac{\partial^2 A}{\partial z^2}\right) \tag{3.4}$$

$$\frac{\partial \Phi}{\partial t} = \frac{p_0 - p}{\rho} - gz \tag{3.5}$$

$$\nabla_{2\mathrm{D}}^2 \Phi = 0 \tag{3.6}$$

where p is the pressure in the liquid and p_0 the equilibrium pressure in the half-space $z > 0$. Equation (3.4) is the linearized vorticity equation for incompressible flow, Eq. (3.5) is a statement of Bernoulli's principle for incompressible flow, and Eq. (3.6) is Laplace's equation, which enforces the condition of incompressibility.

Now assume a periodic solution that is proportional to $e^{i(\tilde{k}x - \omega t)}$ with a wavenumber $\tilde{k}$ that is possibly complex. A general solution of Eq. (3.4) is

$$A = A_0 e^{mz} e^{i(\tilde{k}x - \omega t)} \tag{3.7}$$

where amplitude A_0 is a constant of integration and

$$m^2 = \tilde{k}^2 - \frac{i\omega\rho}{\mu} \tag{3.8}$$

Solution of Eq. (3.6) requires boundary conditions on the liquid half-space. First, stipulate that u and w vanish in the limit $z \to -\infty$. Then a periodic solution of Eq. (3.6) with amplitude Φ_0 is

$$\Phi = \Phi_0 e^{|\tilde{k}|z} e^{i(\tilde{k}x - \omega t)} \tag{3.9}$$

The kinematic and dynamic boundary conditions at the surface are now applied. Let $\chi(z,t)$ and $\zeta(x,t)$ be the horizontal and vertical displacements of the surface, respectively, whereby the surface in the presence of wave motion is located at $(x,z) = (\chi,\zeta)$. The linearized kinematic boundary conditions at $z = 0$ are

$$u = \frac{\partial \chi}{\partial t} \tag{3.10a}$$

$$w = \frac{\partial \zeta}{\partial t} \tag{3.10b}$$

Next, the normal and tangential stresses must be balanced at the interface of the liquid and vacuum half-spaces. Using the notation of Kappler et al.,[20] let μ_{2D}, ρ_{2D}, K_{2D}, and γ_s be material properties of the interface that describe its viscosity, density, elastic modulus, and surface tension, respectively. The linearized normal stress balance at the interface, $z = 0$, is

$$\rho_{2D}\frac{\partial^2 \zeta}{\partial t^2} = \gamma_s \frac{\partial^2 \zeta}{\partial x^2} + \mu_{2D}\frac{\partial^2}{\partial x^2}\left(\frac{\partial \zeta}{\partial t}\right) - 2\mu\frac{\partial w}{\partial z} - (p_0 - p) \tag{3.11}$$

Equation (3.11) is an expression of Newton's second law for the normal acceleration of the interface. The Bernoulli equation, Eq. (3.5), is now substituted into Eq. (3.11) in place of the term $(p_0 - p)$. With ζ substituted for z in the Bernoulli equation since Eq. (3.11) is applied at the interface, one obtains

$$\rho_{2D}\frac{\partial^2\zeta}{\partial t^2} = \gamma_s\frac{\partial^2\zeta}{\partial x^2} + \mu_{2D}\frac{\partial^2}{\partial x^2}\left(\frac{\partial\zeta}{\partial t}\right) - 2\mu\frac{\partial w}{\partial z} - \rho\frac{\partial\Phi}{\partial t} - \rho g\zeta \tag{3.12}$$

The kinematic boundary condition, Eq. (3.10b), is used to express ζ in terms of w. Finally, Eq. (3.1b) is used to substitute Φ and A for w, which yields

$$\begin{aligned}\rho_{2D}\left(\frac{\partial^2\Phi}{\partial z\partial t} + \frac{\partial^2 A}{\partial x\partial t}\right) = \gamma_s\frac{\partial^2}{\partial x^2}\int\left(\frac{\partial\Phi}{\partial z} + \frac{\partial A}{\partial x}\right)dt + \mu_{2D}\left(\frac{\partial^3\Phi}{\partial x^2\partial z} + \frac{\partial^3 A}{\partial x^3}\right)\\ - 2\mu\left(\frac{\partial^2\Phi}{\partial z^2} + \frac{\partial^2 A}{\partial x\partial z}\right) - \rho\frac{\partial\Phi}{\partial t} - \rho g\int\left(\frac{\partial\Phi}{\partial z} + \frac{\partial A}{\partial x}\right)dt\end{aligned} \tag{3.13}$$

The tangential stress balance at the interface, i.e., expression of Newton's second law for tangential interfacial acceleration, is

$$\rho_{2D}\frac{\partial^2\chi}{\partial t^2} = K_{2D}\frac{\partial^2\chi}{\partial x^2} + \mu_{2D}\frac{\partial^2}{\partial x^2}\left(\frac{\partial\chi}{\partial t}\right) - \mu\left(\frac{\partial u}{\partial z} + \frac{\partial w}{\partial x}\right) \tag{3.14}$$

As in the derivation of Eq. (3.13), the kinematic boundary condition, Eq. (3.10a), is used to replace χ with u in Eq. (3.14). The variables Φ and A are substituted for u and w using Eqs. (3.1a) and (3.1b), respectively. Equation (3.14) thus becomes

$$\begin{aligned}\rho_{2D}\left(\frac{\partial^2\Phi}{\partial x\partial t} - \frac{\partial^2 A}{\partial z\partial t}\right) = K_{2D}\frac{\partial^2}{\partial x^2}\int\left(\frac{\partial\Phi}{\partial x} - \frac{\partial A}{\partial z}\right)dt + \mu_{2D}\left(\frac{\partial^3\Phi}{\partial x^3} - \frac{\partial^3 A}{\partial x^2\partial z}\right)\\ - 2\mu\left(\frac{\partial^2\Phi}{\partial x\partial z} - \frac{\partial^2 A}{\partial z^2} + \frac{\partial^2 A}{\partial x^2}\right)\end{aligned} \tag{3.15}$$

Following substitution of the proposed periodic solution defined by Eqs. (3.7)–(3.9) into the normal and tangential stress balance equations, Eqs. (3.13) and (3.15), respectively, the following system of two equations for the three unknowns Φ_0, A_0, and $\tilde{k}$ defines the dispersion relation for a class of interface waves:

$$\left[-i\omega\rho + \frac{i\rho g|\tilde{k}|}{\omega} + 2\mu\tilde{k}^2 + \frac{i\gamma_s|\tilde{k}|^3}{\omega} + \mu_{2\mathrm{D}}|\tilde{k}|^3 - i\rho_{2\mathrm{D}}\omega|\tilde{k}|\right]\Phi_0 + \left[-\frac{\rho g\tilde{k}}{\omega} + i2\mu m\tilde{k} - \frac{\gamma_s\tilde{k}^3}{\omega} + i\mu_{2\mathrm{D}}\tilde{k}^3 + \rho_{2\mathrm{D}}\omega\tilde{k}\right]A_0 = 0 \quad (3.16)$$

$$\left[i2\mu\tilde{k}|\tilde{k}| - \frac{K_{2\mathrm{D}}\tilde{k}^3}{\omega} + i\mu_{2\mathrm{D}}\tilde{k}^3 + \rho_{2\mathrm{D}}\omega\tilde{k}\right]\Phi_0 + \left[-\mu\left(m^2 + \tilde{k}^2\right) - \frac{iK_{2\mathrm{D}}m\tilde{k}^2}{\omega} - \mu_{2\mathrm{D}}m\tilde{k}^2 + i\rho_{2\mathrm{D}}\omega m\right]A_0 = 0 \quad (3.17)$$

Setting the determinant equal to zero to ensure a nontrivial solution (nonzero values for Φ_0 and A_0) provides the dispersion relation for $\tilde{k}$ as a function of ω. After choosing the value of either Φ_0 or A_0, the particle displacement fields for the proposed solutions, Eqs. (3.7) and (3.9), can be evaluated using Eqs. (3.1a) and (3.1b), where the complex wavenumber $\tilde{k}$ is calculated numerically. Figure 3.1 shows several displacement fields and particle trajectories for a DPPC monolayer coupled to a bulk water medium. Numerical values for the physical constants of the monolayer are similar to those used by Kappler et al.[20] For reference, Fig. 3.2 shows the displacement field for a Rayleigh surface wave in a medium with physical values characteristic of an elastic material.[50]

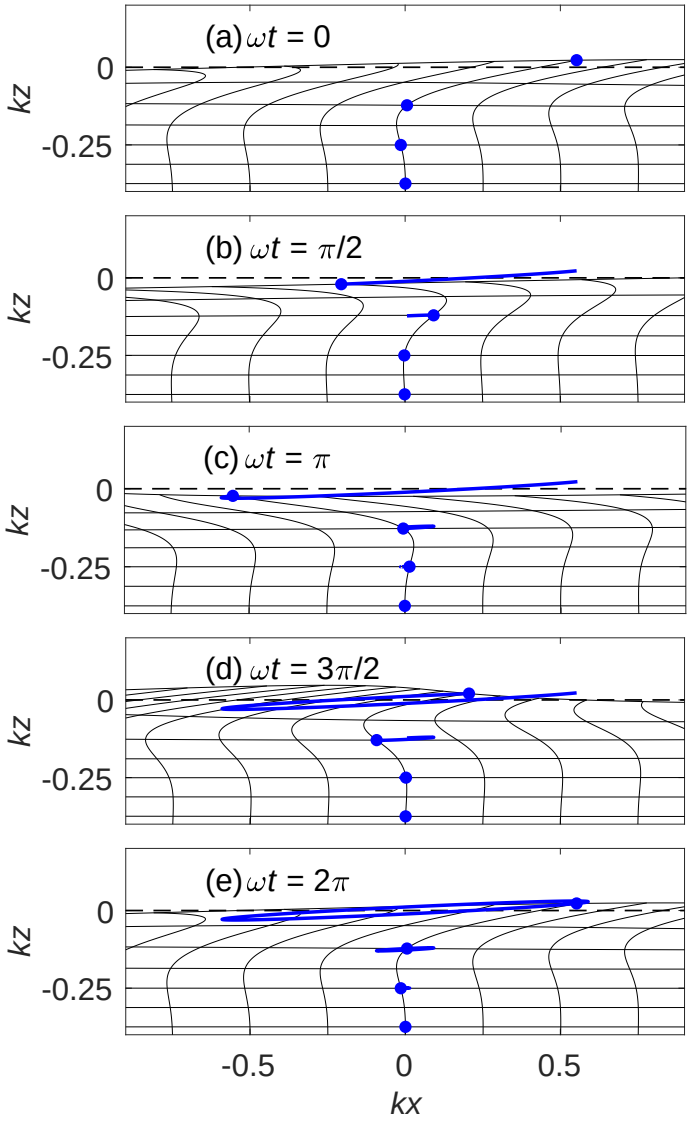

Figure 3.1: Particle displacements for a harmonic solution that satisfies Eqs. (3.16) and (3.17) with $\omega = 1000 \times 2\pi$ rad/s, $\rho = 1000$ kg/m^3, $\mu = 0.001$ Pa $\cdot$ s, $\rho_{2D} = 1 \times 10^{-6}$ kg/m^2, $\mu_{2D} = 1 \times 10^{-9}$ Pa $\cdot$ s $\cdot$ m, $K_{2D} = 0.03$ N/m, $g = 9.81$ m/s^2, and $\gamma_s = 0.07$ N/m. The wavenumber k is obtained numerically with $k = \mathrm{Re}\{\tilde{k}\}$. Plot is approximately to scale.

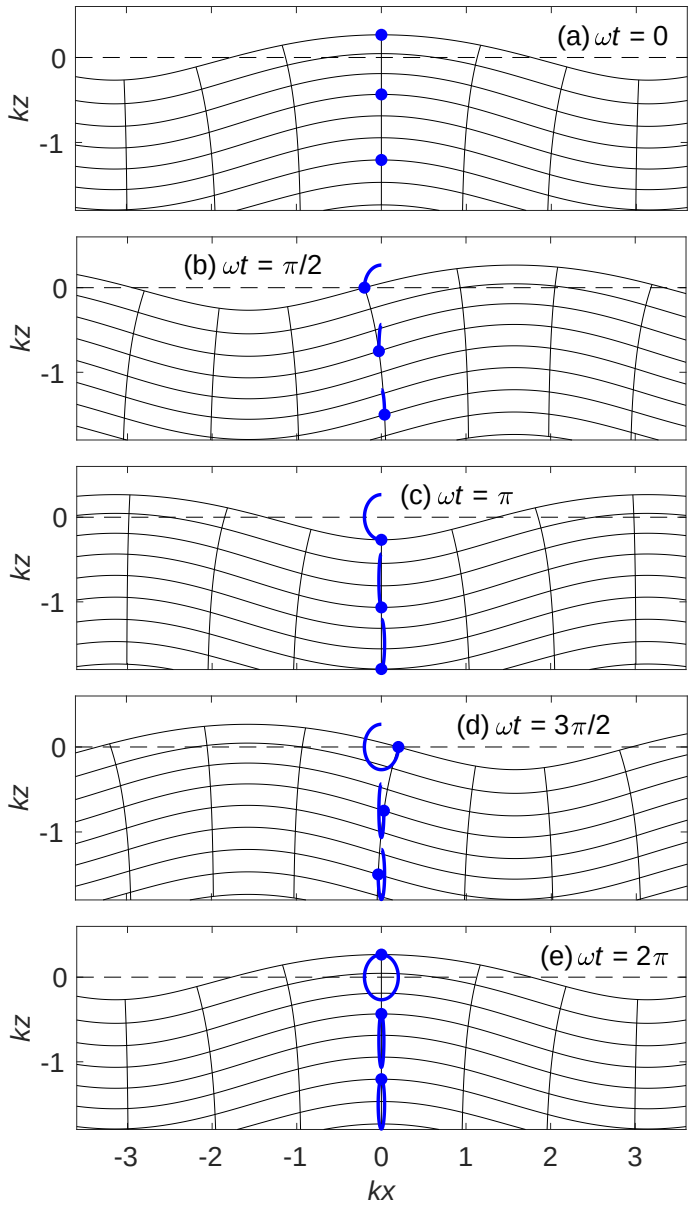

Figure 3.2: Particle displacement plots for Rayleigh waves with $\omega = 1000 \times 2\pi$ rad/s, Poisson's ratio $\nu = 0.3$, transverse wave speed $c_t = 2100$ m/s, and longitudinal wave speed $c_l = 5700$ m/s. Plot is approximately to scale.

As seen in Fig. 3.1, the harmonic wave solutions that satisfy the dispersion relations (3.16) and (3.17) exhibit primarily longitudinal particle motion (the amplitude of the horizontal motion amplitude is more than ten times greater than that of the vertical motion). That is, the particle motion is mainly horizontal as opposed to vertical. This motion is distinctly different from that of the particle trajectories in Fig. 3.2 for a Rayleigh wave, which are elliptical with non-negligible motion in both directions. Physically, the resistance to motion perpendicular to the interface is due to the additional normal stress provided by the presence of interfacial elasticity.[21]

The primarily longitudinal motion of the surface waves satisfying the dispersion relations in Eqs. (3.16) and (3.17) permit a more simple and analytically manageable dispersion relation to be obtained by allowing additional assumptions to be made. The first assumption is that, because the particle velocity is primarily longitudinal, the vertical particle velocity w is negligible relative to the horizontal particle velocity u near the interface, i.e.,

$$|w| \ll |u| \tag{3.18}$$

Substitute Eqs. (3.1b) and (3.1a) into Eq. (3.18) to obtain

$$\left|\frac{\partial \Phi}{\partial z} + \frac{\partial A}{\partial x}\right| \ll \left|\frac{\partial \Phi}{\partial x} - \frac{\partial A}{\partial z}\right| \tag{3.19}$$

Next, substitution of Eqs. (3.7) and (3.9) into Eq. (3.19) at the interface $z = 0$ yields

$$\left|\tilde{k}|\Phi_0 + i\tilde{k}A_0\right| \ll \left|i\tilde{k}\Phi_0 - mA_0\right| \tag{3.20}$$

In Eq. (3.20) the terms $|\tilde{k}|\Phi_0$ and $i\tilde{k}\Phi_0$ are of the same order of magnitude. Therefore, the statement in Eq. (3.20) implies that the magnitude of the term mA_0 is much larger than that of the other terms in Eq. (3.20), i.e.,

$$|mA_0| \gg |\tilde{k}\Phi_0|, |\tilde{k}A_0|, |\tilde{k}\Phi_0| \tag{3.21}$$

A consequence of Eq. (3.21) is that $|m| \gg |\tilde{k}|$, which is typically true. For most liquids of practical interest, the following inequality holds

$$\sqrt{\frac{\omega\rho}{\mu}} \gg |\tilde{k}| \tag{3.22}$$

For example, for numerical values of the physical quantities that yield the particle trajectories shown in Fig. 3.1, the left-hand side of Eq. (3.22) is approximately 20 times larger than the right-hand side. Equations (3.8) and (3.22) then yield

$$m \simeq \sqrt{-i\omega\rho/\mu} \tag{3.23a}$$

$$|m| \gg |\tilde{k}| \tag{3.23b}$$

which is consistent with Eq. (3.21). Equation (3.21) is used to show that, at the interface ($z = 0$), the horizontal particle velocity can be approximated as dependent only on the stream function, A:

$$|u| \simeq |mA_0| = \left|\frac{\partial A}{\partial z}\right| \tag{3.24}$$

Since the motion at the interface is primarily longitudinal, it is also assumed that the vertical displacement at the surface ζ is negligible relative

to the horizontal displacement at the surface χ, i.e.,

$$|\zeta| \ll |\chi| \tag{3.25}$$

Because every term of the normal stress equation, Eq. (3.11), except for $(p_0 - p)$ depends on the partial derivatives of the small quantities w and ζ, while most terms in the tangential stress equation, Eq. (3.14), depend on the much larger quantities u and χ, it follows that normal stresses are small compared to tangential stresses. This is consistent with the physical intuition that particle motion that is primarily parallel to an interface will cause greater shear stress than normal stress.

In summary, Eqs. (3.18) and (3.24) demonstrate that the particle motion is mainly horizontal and primarily described by the stream function A (compared to the velocity potential Φ). According to Eqs. (3.18) and (3.25), the magnitudes of w and ζ are very small compared to u and χ at the interface, respectively, which implies that the tangential stress dominates normal stress at the interface [see the discussion following Eq. (3.25)]. Therefore, to obtain a leading-order understanding of the dispersion relation for a wave with these properties, only the stream function component of the tangential stress balance [i.e., the second line of Eq. (3.17)] must be set equal to zero. These assumptions are qualitatively reinforced by Fig. 3.1, which depicts predominantly horizontal wave motion. Thus, the reduced dispersion relation, which is simply the second line of Eq. (3.17) set equal to zero, for these longitudinal waves is

$$-\mu\big(m^2 + \tilde{k}^2\big) - \frac{iK_{2\mathrm{D}} m\tilde{k}^2}{\omega} - \mu_{2\mathrm{D}} m\tilde{k}^2 + i\rho_{2\mathrm{D}}\omega m = 0 \tag{3.26}$$

Relations (3.23a) and (3.23b) are substituted into Eq. (3.26) to obtain

$$\tilde{k}^2 = \frac{\sqrt{i\omega^3\rho\mu} + \rho_{2\mathrm{D}}\omega^2}{K_{2\mathrm{D}} - i\omega\mu_{2\mathrm{D}}} \tag{3.27}$$

Equation (3.27) was presented previously by Kappler, Shrivastava, Schneider, and Netz.[20] In the absence of viscosity in the both the fluid and the interface ($\mu = 0$ and $\mu_{2\mathrm{D}} = 0$) Eq. (3.27) reduces to the dispersion relation for a traditional wave on a membrane with properties $\rho_{2\mathrm{D}}$ and $K_{2\mathrm{D}}$ determining the wave speed.

Equation (3.27) can be associated with a wave equation by rearranging as follows:

$$K_{2\mathrm{D}}\left(-\tilde{k}^2\right) + \mu_{2\mathrm{D}}\left(-\tilde{k}^2\right)(-i\omega) = \sqrt{\rho\mu}\,(-i\omega)^{3/2} + \rho_{2\mathrm{D}}(-i\omega)^2 \tag{3.28}$$

An equivalent version of Eq. (3.28) for particle displacement ξ in the time domain and in physical space is thus

$$K_{2\mathrm{D}}\frac{\partial^2\xi}{\partial x^2} + \mu_{2\mathrm{D}}\frac{\partial^3\xi}{\partial t\partial x^2} = \sqrt{\rho\mu}\frac{\partial^{3/2}\xi}{\partial t^{3/2}} + \rho_{2\mathrm{D}}\frac{\partial^2\xi}{\partial t^2} \tag{3.29}$$

Lucassen[21] assumed that the interface density $\rho_{2\mathrm{D}}$ and viscosity $\mu_{2\mathrm{D}}$ are negligible. For $\rho_{2\mathrm{D}} = 0$ and $\mu_{2\mathrm{D}} = 0$, Eq. (3.27) reduces to the dispersion relation that Lucassen derived, which is the traditional dispersion relation for what are commonly referred to as Lucassen waves:

$$\tilde{k} = \frac{\left(i\omega^3\rho\mu\right)^{1/4}}{\sqrt{K_{2\mathrm{D}}}} \tag{3.30}$$

Likewise, Eq. (3.29) reduces to the same fractional wave equation presented by Kappler:[20]

$$K_{2\mathrm{D}}\frac{\partial^2\xi}{\partial x^2} = \sqrt{\rho\mu}\frac{\partial^{3/2}\xi}{\partial t^{3/2}} \tag{3.31}$$

In Eq. (3.30), the complex quantity $\tilde{k}$ can be expressed in terms of its real and imaginary component parts, $\tilde{k} = k + i\alpha$, where k is the wavenumber and α is the attenuation coefficient. Using Eq. (2.14), these quantities can be written explicitly as

$$k = \sin(3\pi/8) \left(\rho\mu/K_{2\mathrm{D}}^2\right)^{1/4} \omega^{3/4} \tag{3.32a}$$

$$\alpha = \cos(3\pi/8) \left(\rho\mu/K_{2\mathrm{D}}^2\right)^{1/4} \omega^{3/4} \tag{3.32b}$$

Equations (3.32a) and (3.32b) indicate that Lucassen waves are strongly damped on the scale of a wavelength. From Eq. (2.14) one obtains $\alpha\lambda = 2\pi \cot(3\pi/8) \simeq 2.6$, where $\lambda = 2\pi/k$ is wavelength. This in turn corresponds to attenuation of 22.6 dB per wavelength. The phase speed, which can be calculated using Eq. (2.15), is given by

$$c_{\mathrm{ph}}(\omega) = \frac{\omega}{k} = \csc(3\pi/8)(K_{2\mathrm{D}}^2/\rho\mu)^{1/4}\, \omega^{1/4} \tag{3.33}$$

Figure 3.3 shows the dispersion relation $\tilde{k}(\omega)$ obtained from Eq. (3.27) with numerical values provided by Kappler et al.[20] for a DPPC layer coupled to a bulk water medium. Four cases are shown: the traditional Lucassen wave dispersion without interface density $\rho_{2\mathrm{D}}$ or viscosity $\mu_{2\mathrm{D}}$ (red), dispersion with interface density included but not interface viscosity (blue), dispersion with interface viscosity included but not interface density (green), and dispersion with both interface density and viscosity included (black). For $\omega < 10^6$ rad/s, the Lucassen dispersion relation Eq. (3.30) is in close agreement with the other curves, validating Lucassen's original assumption that the interface density

and viscosity are negligible. Prior experiments[14] performed on a DDPC layer primarily considered $\omega \lesssim 10^3$ rad/s, which falls in this low frequency range. For $10^6 < \omega < 10^7$ rad/s inclusion of the viscosity $\mu_{2\mathrm{D}}$ in the interface yields a clear difference. In the region $\omega > 10^7$ rad/s, the curves further differentiate from one another. It should be noted that for sufficiently large ω the linearity assumption for the Navier-Stokes equations [Eqs. (3.3a) and (3.3b)] begins to break down depending on the initial amplitude of the waveform [see discussion surrounding Eq. (S103) in Kappler et al.[20]]. For the frequency range shown in Fig. 3.3, the interface density $\rho_{2\mathrm{D}}$ produces very little changes in the curves (i.e., the red and green curves are in very close agreement with the blue and black curves, respectively). The inclusion of interface viscosity (in addition to liquid viscosity) for nonlinear Lucassen waves is considered in Sec. 3.4.

3.3 Nonlinear Lucassen waves

Nonlinearity in Lucassen surface waves was first taken into account by Kappler, Shrivastava, Schneider, and Netz.[20] The nonlinearity was introduced by allowing the elastic modulus of the interface to vary with particle displacement, such that $K_{2\mathrm{D}} = K_{2\mathrm{D}}(\xi)$ in Eq. (3.31). Their Eq. (23), henceforth referred to as the KSSN equation, is expressed here in the form

$$\left[\kappa_0 + \kappa_1 \frac{\partial \xi}{\partial x} + \kappa_2 \left(\frac{\partial \xi}{\partial x}\right)^2\right] \frac{\partial^2 \xi}{\partial x^2} = \sqrt{\rho\mu}\, \frac{\partial^{3/2} \xi}{\partial t^{3/2}} \tag{3.34}$$

where $\kappa_{0,1,2}$ are experimentally determined elastic constants that describe the nonlinear elasticity of the interface. These constants are defined by the fol-

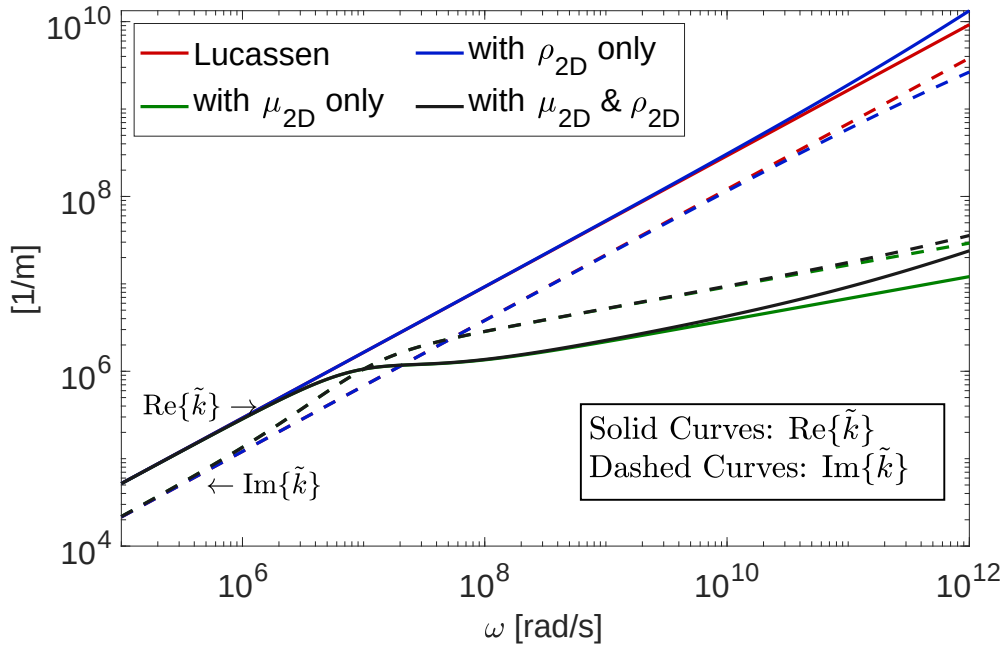

Figure 3.3: Plots of $\tilde{k}(\omega)$ given by the dispersion relation, Eq. (3.27), with $\rho = 10^3$ kg/m^3, $\mu = 10^{-3}$ Pa·s, and $K_{2D} = 1\times10^{-2}$ N/m. The solid curves represent the real part of $\tilde{k}$ and the dashed curves represent the imaginary part of $\tilde{k}$. The red curve corresponds to $\rho_{2D} = \mu_{2D} = 0$, which is the dispersion relation for Lucassen waves, the blue curve corresponds to $\rho_{2D} = 1\times10^{-6}$ kg/m^2 and $\mu_{2D} = 0$, the green curve corresponds to $\rho_{2D} = 0$ and $\mu_{2D} = 1\times10^{-9}$ Pa·s·m, and the black curve corresponds to $\rho_{2D} = 1\times10^{-6}$ kg/m^2 and $\mu_{2D} = 1\times10^{-9}$ Pa·s·m.

lowing relations:

$$\kappa_0 = K_{2D}^{(0)} + K_{2D}^{(2)}(\overline{a} - a_0)^2 \qquad \kappa_1 = 2K_{2D}^{(2)}\overline{a}(\overline{a} - a_0) \qquad \kappa_2 = K_{2D}^{(2)}\overline{a}^2 \quad (3.35)$$

where $\overline{a}$ and a_0 have dimensions of area. Kappler et al. report numerical values for $K_{2D}^{(0)}$, $K_{2D}^{(2)}$, $\overline{a}$, and a_0 corresponding to a DPPC lipid monolayer at an air-water interface. Nonlinearity in the Navier-Stokes equation describing the incompressible liquid, estimated by Kappler et al. to be negligible com-

pared with nonlinearity of the elastic interface, is not taken into account by Eq. (3.34).

We are interested in formulating Eq. (3.34) as a signaling problem (briefly discussed in Sec. 2.3.2) in which the interface is initially at equilibrium [$u = 0$ and $\partial u/\partial t = 0$ at $t = 0$] with a known displacement u or gradient $\partial u/\partial x$ at $x = 0$ and the interface remaining at rest at $x = \infty$ [$u(\infty, t) = 0$]. The second boundary condition [$u(\infty, t) = 0$] signifies that the initial signal at $x = 0$ will completely dissipate after an infinite distance due to the attenuation introduced by the fractional derivative in Eq. (3.34). However, in any conventional numerical algorithm the physical domain must be finite, requiring an arbitrary distance L to be chosen such that an initial waveform will be sufficiently attenuated over length L to be considered an accurate approximation of the true signaling problem formulation in which infinite propagation distances are considered. This presents two difficulties, the first of which is that it is difficult to know exactly what value L should be chosen to obtain a sufficiently accurate approximation of the signaling problem for Eq. (3.34). Second, the user is required to calculate the solution of Eq. (3.34) for large x even if the user is only interested in behavior near the source (i.e., $x \ll L$). The fact that Eq. (3.34) is nonlinear and includes a fractional derivative creates even more numerical difficulties. To facilitate numerical computation, a simplified form of Eq. (3.34) for progressive waves is considered in which a single initial condition at $x = 0$ can be evolved forward by incrementally stepping in x. For a discussion of the finite difference scheme used to solve Eq. (3.34) in the

present work, see Sec. A.3.

3.3.1 Evolution equation in a fixed reference frame

The desired equation is first order in the partial derivative with respect to x and describes the nonlinear evolution of a progressive wave propagating in the $+x$ direction. To develop such a nonlinear evolution equation, it is convenient first to reorganize Eq. (3.34) by collecting the linear terms on the left and the nonlinear terms on the right:

$$\frac{\partial^2 \xi}{\partial x^2} - \frac{\sqrt{\rho\mu}}{\kappa_0}\frac{\partial^{3/2}\xi}{\partial t^{3/2}} = -\frac{\kappa_1}{\kappa_0}\frac{\partial \xi}{\partial x}\frac{\partial^2 \xi}{\partial x^2} - \frac{\kappa_2}{\kappa_0}\left(\frac{\partial \xi}{\partial x}\right)^2 \frac{\partial^2 \xi}{\partial x^2} \tag{3.36}$$

Now set the right-hand side to zero and consider the linear form of this equation, which is equivalent to Eq. (3.31) and rewritten here as

$$\left[\frac{\partial}{\partial x} + \left(\frac{\rho\mu}{\kappa_0^2}\right)^{1/4}\frac{\partial^{3/4}}{\partial t^{3/4}}\right]\left[\frac{\partial}{\partial x} - \left(\frac{\rho\mu}{\kappa_0^2}\right)^{1/4}\frac{\partial^{3/4}}{\partial t^{3/4}}\right]\xi = 0 \tag{3.37}$$

The factorization creates two wave-like operators, the first for propagation in the $+x$ direction, and the second for propagation in the $-x$ direction. Choosing the first operator for propagation in the $+x$ direction yields

$$\frac{\partial \xi}{\partial x} + \left(\frac{\rho\mu}{\kappa_0^2}\right)^{1/4}\frac{\partial^{3/4}\xi}{\partial t^{3/4}} = 0 \tag{3.38}$$

from which the linear dispersion relation Eq. (3.30) is recovered for $\xi = \xi_0 e^{i(\tilde{k}x - \omega t)}$. Equations (3.31) (with $K_{2\mathrm{D}} = \kappa_0$) and (3.38) thus admit equivalent solutions for linear evolution of a waveform propagating in the $+x$ direction.

From Eq. (3.38) it is observed that the time and space derivatives for

linear propagation in the $+x$ direction are related as follows:

$$\left(\frac{\rho\mu}{\kappa_0^2}\right)^{1/4}\frac{\partial^{3/4}}{\partial t^{3/4}} = -\frac{\partial}{\partial x} \tag{3.39}$$

By factoring the left-hand side of Eq. (3.36) as in Eq. (3.37) and using Eq. (3.39) to approximate the second fractional time derivative with a space derivative, one arrives at the following approximate form of Eq. (3.36) for wave propagation in the $+x$ direction:

$$2\left[\frac{\partial}{\partial x} + \left(\frac{\rho\mu}{\kappa_0^2}\right)^{1/4}\frac{\partial^{3/4}}{\partial t^{3/4}}\right]\frac{\partial\xi}{\partial x} = -\frac{\kappa_1}{\kappa_0}\frac{\partial\xi}{\partial x}\frac{\partial^2\xi}{\partial x^2} - \frac{\kappa_2}{\kappa_0}\left(\frac{\partial\xi}{\partial x}\right)^2\frac{\partial^2\xi}{\partial x^2} \tag{3.40}$$

Introduction of the new wave variable $\psi = -\partial\xi/\partial x$ and rearrangement of the result yields the following evolution equation:

$$\frac{\partial\psi}{\partial x} = -\frac{(\rho\mu/\kappa_0^2)^{1/4}}{1-(\kappa_1/2\kappa_0)\psi+(\kappa_2/2\kappa_0)\psi^2}\frac{\partial^{3/4}\psi}{\partial t^{3/4}} \tag{3.41}$$

Equation (3.38) is recovered for linear propagation ($\kappa_1 = \kappa_2 = 0$).

The quantity ψ characterizes the compression of the interface in the direction of propagation. In terms of the corresponding particle velocity $u = \partial\xi/\partial t$, for linear propagation of the harmonic wave $\xi = \xi_0 e^{i(\tilde{k}x-\omega t)}$ one obtains $\psi = (1+i\alpha/k)u/c_{\rm ph}$. Since $\alpha/k = 0.414$ for a Lucassen wave, the magnitude of ψ exceeds that of $u/c_{\rm ph}$ by 8.24% and its phase differs by 22.5°. By comparison, for a sound wave in a viscous compressible fluid the quantity α/k is normally exceedingly small compared with unity and one obtains $\psi = u/c_{\rm ph}$.

3.3.2 Evolution equation in a moving reference frame

An alternative nonlinear evolution equation, obtained in a moving reference frame, is developed here for comparison with traditional evolution equa-

tions in nonlinear acoustics. Begin by rewriting Eq. (3.41) in the form

$$\left(\frac{\rho\mu}{\kappa_0^2}\right)^{1/4}\frac{\partial^{3/4}\psi}{\partial t^{3/4}} = -\left(1-\frac{\kappa_1}{2\kappa_0}\psi+\frac{\kappa_2}{2\kappa_0}\psi^2\right)\frac{\partial\psi}{\partial x} \tag{3.42}$$

The desired evolution equation is based on a reference frame moving at the nominal phase speed of the wave. Let $c_0 = c_{\rm ph}(\omega_0)$ be the phase speed at a characteristic frequency $\omega = \omega_0$ of the waveform, e.g., the center frequency of a narrowband signal, and introduce the retarded time $\tau = t - x/c_0$. Next, assume slow variations of the waveform in the reference frame translating at speed c_0 and transform Eq. (3.42) from the coordinates (x,t) into the new coordinates $(x_1,\tau) = (\epsilon x, t - x/c_0)$, where the dimensionless parameter $\epsilon \ll 1$ characterizes the slowness of changes as a function of x_1 in the (x_1,τ) coordinate system. With the derivatives transformed according to the relations

$$\frac{\partial^{3/4}}{\partial t^{3/4}} = \frac{\partial^{3/4}}{\partial\tau^{3/4}} \qquad \frac{\partial}{\partial x} = \epsilon\frac{\partial}{\partial x_1} - \frac{1}{c_0}\frac{\partial}{\partial\tau} \tag{3.43}$$

Eq. (3.42) becomes

$$\left(\frac{\rho\mu}{\kappa_0^2}\right)^{1/4}\frac{\partial^{3/4}\psi}{\partial\tau^{3/4}} = -\epsilon\frac{\partial\psi}{\partial x_1} + \left(1-\frac{\kappa_1}{2\kappa_0}\psi+\frac{\kappa_2}{2\kappa_0}\psi^2\right)\frac{1}{c_0}\frac{\partial\psi}{\partial\tau} + O(\epsilon\psi^2,\epsilon\psi^3) \tag{3.44}$$

The $O(\epsilon\psi^2,\epsilon\psi^3)$ nonlinear terms (not shown explicitly), together with nonlinear terms containing higher powers of ϵ, are discarded based on their smallness relative to the preceding $O(\psi^2,\psi^3)$ nonlinear terms (shown explicitly). With the original coordinate x reinstated in place of x_1/ϵ in Eq. (3.44), the following evolution equation is obtained:

$$\frac{\partial\psi}{\partial x} = \left(1-\frac{\kappa_1}{2\kappa_0}\psi+\frac{\kappa_2}{2\kappa_0}\psi^2\right)\frac{1}{c_0}\frac{\partial\psi}{\partial\tau} - \left(\frac{\rho\mu}{\kappa_0^2}\right)^{1/4}\frac{\partial^{3/4}\psi}{\partial\tau^{3/4}} \tag{3.45}$$

Like Eq. (3.41), without nonlinearity ($\kappa_1 = \kappa_2 = 0$), Eq. (3.45) is equivalent to Eq. (3.38). In the absence of the fractional derivative, Eq. (3.45) becomes an evolution equation for a simple wave, the implicit solution for which is of the form $\psi = f[\tau + (b_0 + b_1\psi + b_2\psi^2)x]$.

3.3.3 Dimensionless formulation

It is convenient for analysis to recast Eqs. (3.34), (3.41), and (3.45) in dimensionless form by defining

$$U = \xi/\xi_0 \qquad \Psi = \psi/\psi_0 \qquad X = k_0 x \qquad \phi = \omega_0 t \qquad \theta = \omega_0 \tau \tag{3.46}$$

Particle displacement ξ and its negative gradient $\psi = -\partial\xi/\partial x$ are scaled by the characteristic amplitudes ξ_0 and ψ_0, respectively. The variable U, which is chosen to represent dimensionless particle displacement, is not be confused with the dimensional particle velocity u. The variable U is chosen to follow the original notation of Kappler et al.[20] Time and distance are scaled by the characteristic frequency ω_0 and corresponding wavenumber $k_0 = k(\omega_0) = \omega_0/c_0$. Owing to the strong viscous attenuation of a Lucassen wave, relevant propagation distances in terms of the scaled coordinate X are $O(1)$. The following three dimensionless equations are obtained.

KSSN equation, Eq. (3.34):

$$\left[1 - 2N_2\frac{\partial U}{\partial X} + 2N_3\left(\frac{\partial U}{\partial X}\right)^2\right]\frac{\partial^2 U}{\partial X^2} = \gamma^2\frac{\partial^{3/2} U}{\partial \phi^{3/2}} \tag{3.47}$$

Fixed-frame evolution equation, Eq. (3.41):

$$\frac{\partial \Psi}{\partial X} = -\frac{\gamma}{1 + N_2\Psi + N_3\Psi^2}\frac{\partial^{3/4}\Psi}{\partial \phi^{3/4}} \tag{3.48}$$

Moving-frame evolution equation, Eq. (3.45):

$$\frac{\partial \Psi}{\partial X} = (1 + N_2 \Psi + N_3 \Psi^2) \frac{\partial \Psi}{\partial \theta} - \gamma \frac{\partial^{3/4} \Psi}{\partial \theta^{3/4}} \tag{3.49}$$

In each equation appears one numerical coefficient, which is determined using Eqs. (3.32a) and (3.32b),

$$\gamma = \sqrt{1 + (\alpha/k)^2} = \frac{2}{\sqrt{2 + \sqrt{2}}} \simeq 1.0824 \tag{3.50}$$

and two nonlinearity parameters that depend on wave amplitude,

$$N_2 = \beta_2 \psi_0 \qquad N_3 = \beta_3 \psi_0^2 \tag{3.51}$$

where

$$\beta_2 = -\frac{\kappa_1}{2\kappa_0} \qquad \beta_3 = \frac{\kappa_2}{2\kappa_0} \tag{3.52}$$

are the coefficients of quadratic and cubic nonlinearity associated with the elastic interface, respectively.

The sign conventions employed for β_2 and β_3 in Eq. (3.52) correspond to their traditional interpretation in nonlinear acoustics insofar as positive (negative) values indicate that the compression phase of a waveform propagates faster (slower) than predicted by linear theory due to the corresponding quadratic or cubic nonlinearity.

The nonlinearity parameters N_2 and N_3 defined in Eq. (3.51) are proportional to Gol'dberg numbers employed in nonlinear acoustics, which characterize the importance of nonlinearity relative to energy dissipation for the

propagation of a progressive plane wave in a thermoviscous fluid.[51] The traditional Gol'dberg number for quadratic nonlinearity may be expressed as $\Gamma_2 = \beta_2 \epsilon_0 k_0/\alpha_0$, where $\epsilon_0 = u_0/c_0$ is the acoustic Mach number associated with the characteristic particle velocity u_0, and $\alpha_0 = \alpha(\omega_0)$ is the attenuation coefficient at the characteristic frequency ω_0. For a Lucassen wave $\epsilon_0 \simeq 0.924\psi_0$ [recall discussion following Eq. (3.41)] and $k_0/\alpha_0 \simeq 2.414$, such that one obtains the relation $\Gamma_2 \simeq 2.2N_2$. The corresponding Gol'dberg number for cubic nonlinearity is $\Gamma_3 = \beta_3 \epsilon_0^2 k_0/\alpha_0$, such that $\Gamma_3 \simeq 2.1N_3$. For an initially sinusoidal compressional wave subject to quadratic nonlinearity in a thermoviscous fluid, nonlinear distortion of the waveform is negligible for $\Gamma_2 \lesssim 1$, and for $\Gamma_2 \gg 1$ the waveform develops thin shocks that may be approximated by discontinuities.[52] The parameters N_2 and N_3 play a similar role in terms of indicating the degree of nonlinear distortion in Lucassen waves.

It is important to note that in order for N_2 and N_3 to have the same definition in Eq. (3.47) as in Eqs. (3.48) and (3.49) one must stipulate in Eq. (3.47) that $\psi_0 \equiv k_0 u_0$. A consequence of this stipulation when nonlinearity is taken into account is that a source condition must be specified in terms of Ψ rather than U when solutions of Eq. (3.47) are to be compared with those of Eqs. (3.48) and (3.49). That is, Eq. (3.47) must be formulated as a boundary value problem in X with Neumann boundary conditions.

3.3.4 Comparison of three model equations

Numerical solutions of the KSSN equation (3.47), the fixed-frame evolution equation (3.48), and the moving-frame evolution equation (3.49) are compared in Fig. 3.4. In all three panels the dashed black curve is the source waveform

$$\Psi(0,\phi) = \exp[-(\phi/4\pi)^6]\sin\phi \tag{3.53}$$

and the solid black curve is the solution of the KSSN equation at $X = 1$ for $N_2 = -0.78$ and $N_3 = 1.02$ corresponding to $\psi_0 = 0.1$, $\bar{a} = 78.4$ Å^2, $a_0 = 75.4$ Å^2. The physical values of $\bar{a}$ and a_0 describe a DPPC membrane with an equilibrium area per lipid just past the phase transition region.[20] The values for $K_{2\mathrm{D}}^{(0)}$ and $K_{2\mathrm{D}}^{(2)}$ used in Fig. 3.4 are given by Kappler et al.[20]

Compared in Fig. 3.4(a) are the solution of the nonlinear KSSN equation (black curve) and the same linear solution that is obtained from each of Eqs. (3.47), (3.48), and (3.49) (red curve). Besides waveform distortion, the comparison reveals that nonlinearity in the KSSN equation generates a negative DC component, which is absent in the linear solution. Figure 3.4(b) compares solutions of the nonlinear KSSN equation (black curve) and the nonlinear fixed-frame evolution equation (red curve), for which reasonable agreement is observed. Figure 3.4(c) indicates that the solutions of the nonlinear KSSN equation (black curve) and the nonlinear moving-frame evolution equation (red curve) are not in as good agreement. The discrepancy is due mainly to the inability of the moving-frame evolution equation to account for nonlinear

generation of a DC component. A discussion of some of the numerical techniques used to solve the KSSN equation, the fixed-frame evolution equation, and the moving-frame evolution equation is presented in Appendix A.

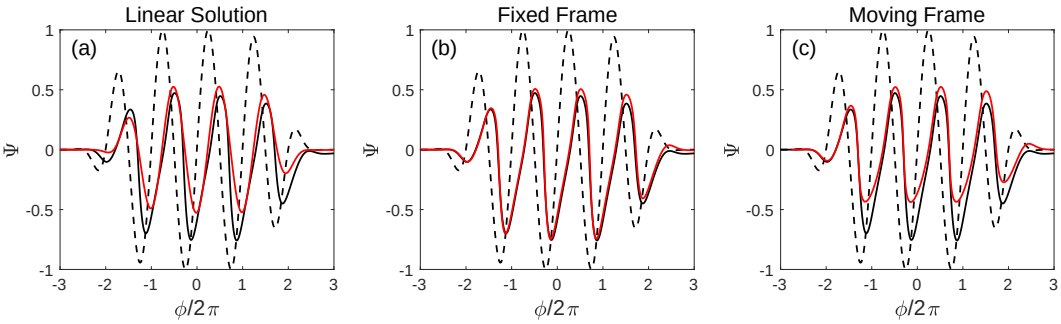

Figure 3.4: In all three panels, the dashed black curve is the source waveform at $X = 0$ and the solid black curve is the numerical solution of the KSSN equation, Eq. (3.47), at $X = 1$ for $N_2 = -0.78$ and $N_3 = 1.02$. (a) Comparison with linear theory at $X = 1$ (red curve, corresponding to $N_2 = N_3 = 0$), which is the same for all three model equations: Eqs. (3.47), (3.48), and (3.49). (b) Comparison with the fixed-frame evolution equation (red curve), Eq. (3.48), and (c) comparison with the moving-frame evolution equation (red curve), Eq. (3.49), in each case with $X = 1$, $N_2 = -0.78$, and $N_3 = 1.02$.

3.3.5 Threshold phenomena in nonlinear Lucassen waves

From their numerical solutions of Eq. (3.34), Kappler et al.[20] observed that "For $\overline{a} < a_0$ [such that, in our notation, $\kappa_1 < 0$ and $\beta_2 > 0$ from Eqs. (3.35) and (3.52), respectively] nonlinear effects lead to a monotonic and smooth increase of the wave speed as a function of the driving amplitude $\xi_0^{\max}$, while for $\overline{a} > a_0$ [thus $\kappa_1 > 0$ and $\beta_2 < 0$] the speed decreases slightly and then abruptly increases at a threshold amplitude of about $\xi_0^{\max} = 2$ mm." A possible explanation of these observations is the competition between quadratic and

cubic nonlinearity.

The wave speed referred to by Kappler et al. is related to the finite-amplitude propagation speed, which varies from point to point along the waveform. Insight into the amplitude dependence of the propagation speed is facilitated by ignoring the effects of attenuation and dispersion, which is accomplished most easily using the moving-frame evolution equation, Eq. (3.45).

Retaining only the nonlinear terms on the right-hand side of Eq. (3.45) and designating $\hat{\psi}$ as the solution of the resulting equation yields, following introduction of the coefficients of nonlinearity defined in Eq. (3.52),

$$\frac{\partial \hat{\psi}}{\partial x} = (\beta_2 \hat{\psi} + \beta_3 \hat{\psi}^2) \frac{1}{c_0} \frac{\partial \hat{\psi}}{\partial \tau} \tag{3.54}$$

The quantity $(\beta_2 \hat{\psi} + \beta_3 \hat{\psi}^2)/c_0$ is the rate, per unit distance, at which a point on the waveform identified by its local amplitude $\hat{\psi}$ advances or recedes in the retarded time frame $\tau = t - x/c_0$ associated with the reference frame moving at speed c_0. This behavior is most easily understood by considering the characteristics associated with Eq. (3.54), which are obtained by setting the total differential $d\hat{\psi} = (\partial \hat{\psi}/\partial x)dx + (\partial \hat{\psi}/\partial \tau)d\tau$ equal to zero [i.e., $\hat{\psi}(x, \tau) = \text{const}$]:

$$\left.\frac{d\tau}{dx}\right|_{\hat{\psi}=\text{const}} = -\left.\frac{\partial \hat{\psi}/\partial x}{\partial \hat{\psi}/\partial \tau}\right|_{\hat{\psi}=\text{const}} = -(\beta_2 \hat{\psi} + \beta_3 \hat{\psi}^2)/c_0 \tag{3.55}$$

For $\beta_2 \hat{\psi} + \beta_3 \hat{\psi}^2 > 0$ the given point on the waveform arrives earlier per unit distance and thus travels faster than c_0, and for $\beta_2 \hat{\psi} + \beta_3 \hat{\psi}^2 < 0$ it arrives later and thus travels slower.

The wave speed discussed by Kappler et al.[20] [see their Eq. (30) and Fig. 5] is the velocity of the positive peak amplitude (say $\psi = \psi_0$) in the waveform. With the velocity of the positive peak labeled $c_{\rm pk}^+$ and with $(d\tau/dx)_{\psi_0} = 1/c_{\rm pk}^+ - 1/c_0$, making use of Eq. (3.55) evaluated for $\hat{\psi} = \psi_0 \geq 0$ yields

$$c_{\rm pk}^+ = \frac{c_0}{1 - \beta_2\psi_0 - \beta_3\psi_0^2} \tag{3.56}$$

Interpretation of the threshold phenomenon discussed by Kappler et al. in connection with their Fig. 6(c) follows from examining the dependence of $c_{\rm pk}^+$ on the wave amplitude ψ_0. For $\overline{a} < a_0$ both β_2 and β_3 are positive, and therefore increasing ψ_0 produces a "monotonic and smooth increase" in $c_{\rm pk}^+$. But for $\overline{a} > a_0$, β_2 is negative while β_3 remains positive and therefore as ψ_0 increases from zero, $c_{\rm pk}^+$ initially "decreases slightly and then abruptly increases at a threshold amplitude", the value of which may be determined by setting $\beta_2\psi_0 + \beta_3\psi_0^2 = 0$ to obtain

$$\psi_0^{\rm th} = -\frac{\beta_2}{\beta_3} = \frac{\kappa_1}{\kappa_2} \qquad \frac{\kappa_1}{\kappa_2} > 0 \tag{3.57}$$

In other words, for negative β_2, positive β_3, and ψ_0 sufficiently below threshold, the speed decreases approximately linearly as a function of ψ_0 according to $c_{\rm pk}^+ \simeq c_0(1 - |\beta_2|\psi_0)$, whereas for ψ_0 sufficiently above threshold, the speed increases approximately quadratically according to $c_{\rm pk}^+ \simeq c_0(1 + \beta_3\psi_0^2)$.

Note that a different conclusion is reached regarding the threshold phenomenon if the peak negative amplitude in the waveform is considered rather than the peak positive amplitude. Setting $\hat{\psi} = -\psi_0$ in Eq. (3.55) yields

$$c_{\rm pk}^- = \frac{c_0}{1 + \beta_2\psi_0 - \beta_3\psi_0^2} \tag{3.58}$$

in place of Eq. (3.56). The condition for the threshold phenomenon is now reversed, occurring for $\overline{a} < a_0$ (positive β_2) rather than $\overline{a} > a_0$ (negative β_2).

The difference in wave speed is especially important for fractional waves because of their high attenuation. The attenuation length scale is on the order of a wavelength, so nonlinear fractional pulses that travel much faster will have a longer characteristic length scale and thus will attenuate less over a specified distance. This is to say that a nonlinear, fast-traveling fractional wave will arrive at a point in space much less attenuated than a slower traveling pulse arriving at the same point. This conclusion is illustrated in Fig. 3.5, which shows the evolution of an initially unipolar pulse defined by

$$\Psi(0, \theta) = \operatorname{sech}(\phi - 2\pi) \tag{3.59}$$

based on the fixed-frame evolution equation, Eq. (3.48). For amplitudes below and at the threshold, Fig. 3.5(a) and (b), respectively, the pulse arrives at the point $X = 5$ with similar amplitudes. The amplitudes at $X = 5$ are significantly below the source amplitude $\Psi_{\max}(\phi, 0) = 1$. However, well past the threshold, as seen in Fig. 3.5(c), the pulse travels significantly faster and thus arrives at the point $X = 5$ with a much higher amplitude, nearly equivalent to the initial amplitude. This threshold behavior of nonlinear Lucassen waves is another connection to the nerve pulses, which exhibit an "all-or-none" behavior.[18] This connection is discussed in greater detail in Chapter 1.

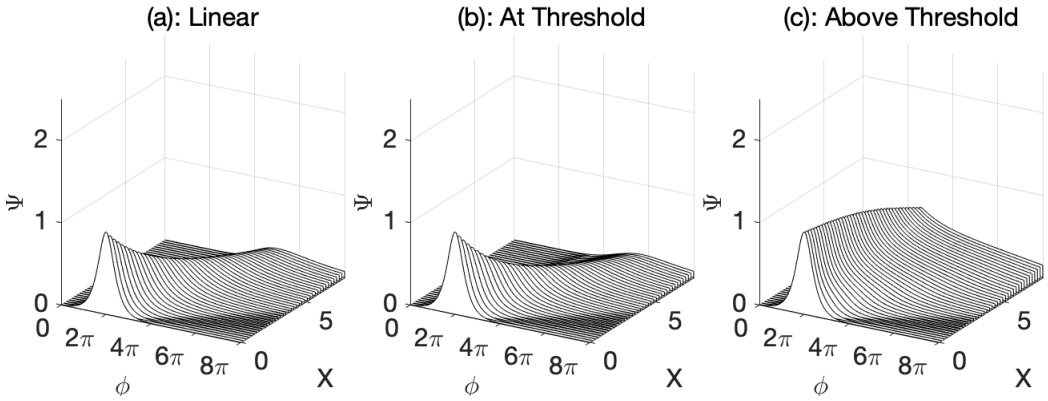

Figure 3.5: Waterfall plots of propagation beginning with the initial condition $\Psi(\theta, 0) = \mathrm{sech}(\phi - 2\pi)$ based on the fixed-frame evolution equation, Eq. (3.48). Here $\beta_2 = -4$ and $\beta_3 = 16$; according to Eq. (3.57), $\psi_0^{\mathrm{th}} = 1/4$. Plot (a) shows linear propagation with $\psi_0 = 0$, (b) shows propagation at the threshold amplitude $\psi_0 = \psi_0^{\mathrm{th}}$, and (c) shows propagation well beyond the threshold with $\psi_0 = 1 = 4\psi_0^{\mathrm{th}}$.

3.3.6 Possibility of shock formation

The evolution equation given by Eq. (3.49), which yields an attenuation coefficient that is proportional to ω^ν with $0 \leq \nu \leq 1$, provides insufficient attenuation and dispersion to stabilize shock formation when the amplitude of a nonlinear waveform exceeds a critical value.[53] A model equation for nonlinear propagation in such a medium yields invalid solutions when the critical amplitude is exceeded and the wave propagates beyond the distance at which a vertical tangent first appears in the waveform, signifying the point of shock formation. The moving-frame evolution equation, Eq. (3.49), falls in this category and thus fails beyond the shock formation distance. Therefore, Eq. (3.49) should only be used for modest values of nonlinearity characterized

by N_2 and N_3. Specific limits on the nonlinearity of the moving-frame evolution equation are discussed in Sec. 4.3.3.

It is not immediately clear if the conclusions regarding the moving-frame evolution equation apply to the fixed-frame evolution equation, Eq. (3.48), or the KSSN equation, Eq. (3.47). While the attenuation is proportional to $\omega^{3/4}$ for Eqs. (3.48) and (3.47), the equations have different functional forms. The fixed-frame evolution equation is less stable numerically for waveforms with high gradients, although this fact alone does not prove whether or not vertical tangent formation, or ultimately a multivalued waveform, are possible. The possibility of waveform overturning for the fixed-frame evolution equation, Eq. (3.48), is discussed in Chap. 4.

3.4 Lucassen waves with interfacial viscosity

Nonlinearity can produce very steep gradients in propagating waveforms with large amplitudes, which can lead to numerical instability for model equations such as (3.47), (3.48), and (3.49). The moving-frame evolution equation has the particular problem of failing at vertical tangent formation for sufficiently high initial amplitudes, as discussed in Sec. 3.3.6. Therefore, it is sometimes useful to reintroduce the interface viscosity that was discarded in Sec. 3.2. The extra attenuation from the interface viscosity will more strongly attenuate the higher harmonics that are generated during nonlinear propagation effects at high amplitudes. This, in turn, can improve numerical stability when describing the steep gradients associated with the shock formation in

the time domain and harmonic generation in the frequency domain. Practical measurement techniques of lipid membrane interfacial viscosity and some interfacial viscosity physical values for various membranes are discussed by Homel et al.[54]

We thus return to Eq. (3.29) and again ignore the term with the interface density ρ_{2D} but now retain the term with the interface viscosity μ_{2D} to obtain

$$K_{2D}\frac{\partial^2\xi}{\partial x^2} + \mu_{2D}\frac{\partial^3\xi}{\partial t\partial x^2} = \sqrt{\rho\mu}\frac{\partial^{3/2}\xi}{\partial t^{3/2}} \tag{3.60}$$

The corresponding evolution is obtained by first rewriting Eq. (3.60) as follows:

$$\left(1 + \tau_{2D}\frac{\partial}{\partial t}\right)\frac{\partial^2\xi}{\partial x^2} = \frac{\sqrt{\rho\mu}}{K_{2D}}\frac{\partial^{3/2}\xi}{\partial t^{3/2}} \tag{3.61}$$

where

$$\tau_{2D} = \frac{\mu_{2D}}{K_{2D}} \tag{3.62}$$

is the time constant associated with the viscoelastic behavior of the interface. Equation (3.61) can now be written in the form

$$\tau_{2D}\dot{y}(t) + y(t) = f(t) \tag{3.63}$$

where

$$y(t) = \frac{\partial^2\xi(t)}{\partial x^2} \qquad f(t) = \frac{\sqrt{\rho\mu}}{K_{2D}}\frac{\partial^{3/2}\xi(t)}{\partial t^{3/2}} \tag{3.64}$$

and the dot in Eq. (3.63) signifies a time derivative. The particular solution of Eq. (3.63) is

$$y(t) = \frac{1}{\tau_{2D}}\int_{-\infty}^{t} f(t')e^{-(t-t')/\tau_{2D}}\,dt' \tag{3.65}$$

which permits an explicit solution of Eq. (3.61) to be expressed as

$$\frac{\partial^2 \xi}{\partial x^2} = \frac{\sqrt{\rho\mu}}{K_{2\mathrm{D}}\tau_{2\mathrm{D}}} \frac{\partial^{3/2}\xi}{\partial t^{3/2}} * e^{-t/\tau_{2\mathrm{D}}} \tag{3.66}$$

where the asterisk $*$ denotes convolution:

$$f(t) * g(t) \triangleq \int_{-\infty}^{\infty} f(t')g(t-t')dt' \tag{3.67}$$

Equation (3.66) can be factored in a way similar to Eq. (3.37) in order to arrive at an evolution equation. Because the fractional operator is a convolution integral in the time domain, Fubini's theorem,[55] which allows the order of integration to be changed, can be used to rearrange the convolutions as follows:

$$\left[\frac{\partial}{\partial x} + \frac{(\rho\mu)^{1/4}}{\sqrt{\mu_{2\mathrm{D}}}} \frac{e^{-t/\tau_{2\mathrm{D}}}}{\sqrt{\pi t}} * \frac{\partial^{3/4}}{\partial t^{3/4}}\right]\left[\frac{\partial}{\partial x} - \frac{(\rho\mu)^{1/4}}{\sqrt{\mu_{2\mathrm{D}}}} \frac{e^{-t/\tau_{2\mathrm{D}}}}{\sqrt{\pi t}} * \frac{\partial^{3/4}}{\partial t^{3/4}}\right]\xi = 0 \tag{3.68}$$

As with Eq. (3.37), choosing the first operator yields an evolution equation for propagation in the $+x$ direction:

$$\frac{\partial \xi}{\partial x} + \frac{(\rho\mu)^{1/4}}{\sqrt{\pi\mu_{2\mathrm{D}}}} \int_{-\infty}^{t} \frac{\partial^{3/4}\xi(t')}{\partial t'^{\,3/4}} \frac{e^{-(t-t')/\tau_{2\mathrm{D}}}}{\sqrt{t-t'}} dt' = 0 \tag{3.69}$$

Equation (3.69) does in fact produce the exact same dispersion relation given by Eq. (3.27) (with $\rho_{2\mathrm{D}}$ neglected). This is proved using the Fourier transform relation $\mathcal{F}_\omega\{e^{-t/\tau_{2\mathrm{D}}}/\sqrt{\pi t\tau_{2\mathrm{D}}}\} = 1/\sqrt{1-i\omega\tau_{2\mathrm{D}}}$ and the fact that a convolution in the time domain corresponds to multiplication in the frequency domain.

For small values of $\mu_{2\mathrm{D}}$, linear propagation predicted by the viscoelastic evolution equation, Eq. (3.69), is very similar to that of the fixed-frame

and moving-frame evolution equations, Eqs. (3.41) and (3.45), respectively. Differences in propagation typically occur only at very high frequencies. For example, for the values used to create Fig. 3.3, propagation of a sinusoidal wave predicated by the viscoelastic evolution equation will be noticeably different only for $\omega > 10^6$ rad/s. This is the point in Fig. 3.3 where the added interface viscosity causes the green and black curves to depart from the red and blue curves.

Nonlinearity is incorporated in the same way as in the derivation for the fixed-frame evolution equation; see Eqs. (3.39) and (3.40). The nonlinear viscoelastic evolution equation is thus

$$\begin{aligned}\frac{\partial\psi}{\partial x} = &-\frac{1}{1-(\kappa_1/2\kappa_0)\psi+(\kappa_2/2\kappa_0)\psi^2} \\ &\times\frac{(\rho\mu)^{1/4}}{\sqrt{\pi}\mu_{2\mathrm{D}}}\int_{-\infty}^{t}\frac{\partial^{3/4}\psi(t')}{\partial t'^{\,3/4}}\frac{e^{-(t-t')/\tau_{2\mathrm{D}}}}{\sqrt{t-t'}}dt' = 0\end{aligned} \tag{3.70}$$

The dimensionless notation from Sec. 3.3.3 is used to write the nonlinear form of Eq. (3.60) and Eq. (3.70), respectively, as

Viscoelastic KSSN equation:

$$\left[1-2N_2\frac{\partial U}{\partial X}+2N_3\left(\frac{\partial U}{\partial X}\right)^2\right]\frac{\partial^2 U}{\partial X^2}+\Omega\frac{\partial^3 U}{\partial\phi\partial X^2}=\gamma^2\frac{\partial^{3/2}U}{\partial\phi^{3/2}} \tag{3.71}$$

Viscoelastic evolution equation, Eq. (3.70):

$$\frac{\partial\Psi}{\partial X}=-\frac{1}{1+N_2\Psi+N_3\Psi^2}\frac{\gamma}{\sqrt{\Omega\pi}}\int_{-\infty}^{\phi}\frac{\partial^{3/4}\Psi}{\partial\phi'^{\,3/4}}\frac{e^{-(\phi-\phi')/\Omega}}{\sqrt{\phi-\phi'}}d\phi' \tag{3.72}$$

where

$$\Omega=\omega_0\tau_{2\mathrm{D}}=\omega_0\frac{\mu_{2\mathrm{D}}}{K_{2\mathrm{D}}} \tag{3.73}$$

is the dimensionless coefficient that characterizes the viscosity of the interface.

In the limit $\Omega \to 0$ the viscoelastic evolution equation, Eq. (3.72), becomes the fixed-frame evolution equation, Eq. (3.48). Because Ω depends on K_{2D} [see Eq. (3.73)], which is a nonlinear parameter, Ω could also be nonlinear and depend on Ψ. However, in the present work Ω is approximated as a constant for the equilibrium value of K_{2D}. For this approximation to be valid for strongly nonlinear propagation, Ω should be chosen such that $\Omega \ll 1$ because in this range the propagation of the waveform will be affected noticeably only near very high gradients in the waveform. In the present work only values for which $\Omega \lesssim 0.1$ are considered for nonlinear propagation.

For $\Omega \gtrsim 1$, linear propagation predicted by the viscoelastic evolution equation, Eq. (3.72), differs significantly from linear Lucassen wave propagation. For $\Omega \gg 1$ there is greater loss over length scales on the order of a wavelength because $\alpha > k$ (see the dispersion curves in Fig. 3.3 for $\omega > 10^6$ rad/s). However, these differences in linear propagation are not the focus of the present work because the original purpose of including interface viscosity is to more accurately model attenuation after the formation of steep gradients in the waveform associated with nonlinear propagation.

Figures 3.6 and 3.7 show comparisons of Eqs. (3.71) and (3.72) for propagation along a viscoelastic interface. The initial waveform in Figs. 3.6 and 3.7 is

$$\Psi(0,\theta) = e^{-(\phi/8)^8} \sin\phi \tag{3.74}$$

For linear propagation, the agreement between Eqs. (3.71) and (3.72) is excellent for $\Omega = 0.01$ in Fig. 3.6(a) and $\Omega = 1$ in Fig. 3.6(b). As expected, there is greater attenuation in the waveform depicted in Fig. 3.6(b) because the interface viscosity is greater.

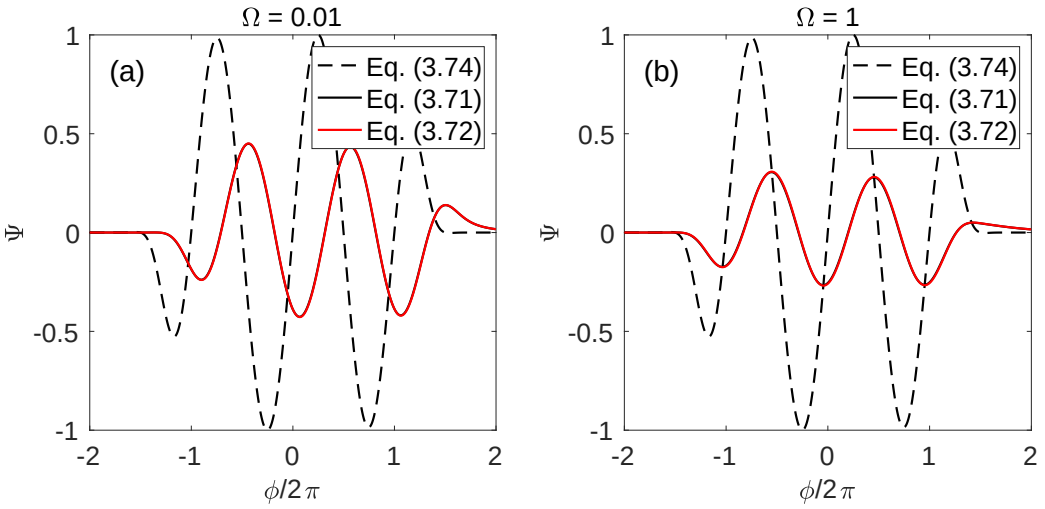

Figure 3.6: Numerical comparison of linear propagation out to $X = 2$ given by the viscoelastic KSSN equation, Eq. (3.71), (black curve) and the viscoelastic evolution equation, Eq. (3.72), (red curve) for an initial condition defined by Eq. (3.74). $\Omega = 0.01$ in (a) and $\Omega = 1$ in (b). The red curve is nearly indistinguishable from the black curve, which is plotted beneath the red curve.

For the nonlinear propagation depicted in Fig. 3.7 the value $\Omega = 0.1$ is chosen because it is large enough to visualize the effects of the interface viscosity but still small enough for Ω to be accurately approximated as a constant for nonlinear propagation (as previously discussed). The agreement in Fig. 3.7 is very reasonable.

The effects of the interface viscosity are better highlighted by consid-

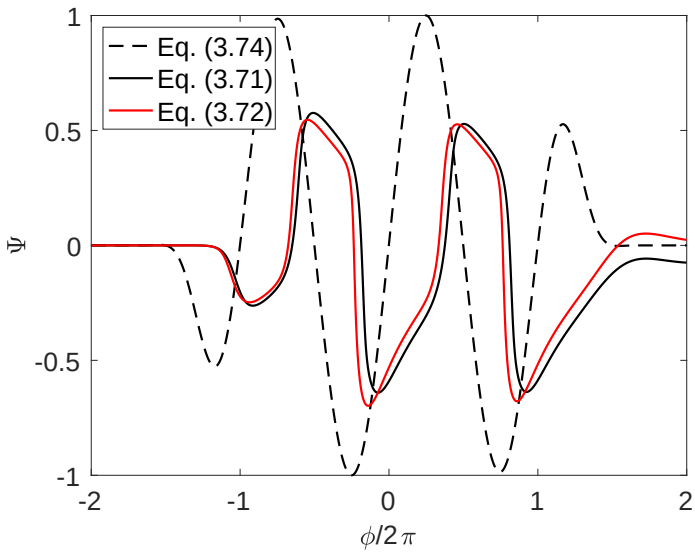

Figure 3.7: Numerical comparison of nonlinear propagation out to $X = 3$ given by the viscoelastic KSSN equation (3.71) and the viscoelastic evolution equation (3.72) for an initial condition defined by Eq. (3.74). In the present case $N_2 = -1$, $N_3 = 5$, and $\Omega = 0.1$.

ering the propagation of a waveform that initially contains a steep gradient. Consider the initial condition

$$\Psi(\phi, 0) = \frac{1}{2}\left[1 + \tanh(20\phi)\right] \tag{3.75}$$

that is nearly a step shock. Figure 3.8 shows the propagation of a waveform that starts out as Eq. (3.75) based on the fixed-frame evolution equation, Eq. (3.48), and which does not account for interface viscosity, and propagation based on the viscoelastic evolution equation, Eq. (3.72), with $\Omega = 0.1$. Even with this seemingly small amount of interface viscosity, Fig. 3.8(a) reveals noticeable differences in the waveforms at $X = 2$ predicted by each equation. The viscoelastic evolution equation predicts a smoother waveform due to the

additional attenuation at high frequencies. This is more evident in Fig. 3.8(b), which shows the time derivatives (gradients) of the predicated waveforms. The fixed-frame evolution equation predicts the step to steepen (i.e., the gradient to increase) in comparison with the step predicted by the viscoelastic evolution equation, which smooths out during propagation (i.e., the gradient decreases). This comparison demonstrates that a small amount of interface viscosity can make a large difference when there are steep gradients in the waveform.

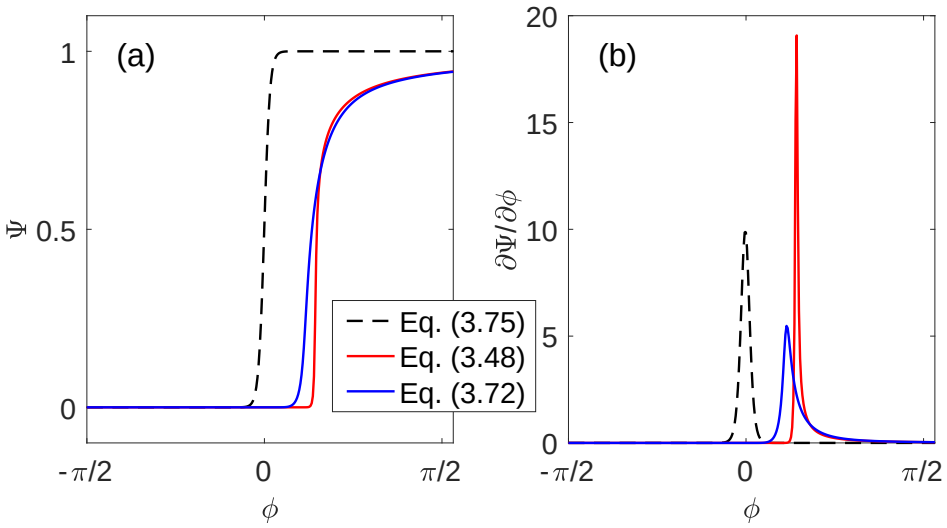

Figure 3.8: Numerical comparison of the fixed-frame evolution equation (3.48) and the viscoelastic evolution equation (3.72) for the initial condition defined by Eq. (3.75). Plot (a) shows the interface compression Ψ while plot (b) shows the time gradient of the compression $\partial\Psi/\partial\phi$. Propagation is carried out to $X = 2$ for $N_2 = -2$, $N_3 = 10$, and $\Omega = 0.1$.

It is also worth noting that evaluating the viscoelastic evolution equation, Eq. (3.72), to produce the results in Fig. 3.8 required about a quarter of the function evaluations needed to evaluate the fixed-frame evolution equa-

tion, Eq. (3.48), using a Runge-Kutta method for the X integration, with a finite-difference approximation for the ϕ derivatives, and with the same tolerance requirement for each equation. This increase in stability that comes from the inclusion of viscosity in the interface is useful even when the viscosity does not lead to significantly different results. Other numerical benefits of including interface viscosity are discussed in Chap. 4 and Appendix A.

3.5 Conclusion

Derivations of model equations for linear Lucassen waves and Lucassen waves with interface viscosity have been presented. Nonlinearity was incorporated by allowing the interfacial bulk modulus to be dependent on the compression of the interface. Corresponding evolution equations have also been derived. These evolution equations are much easier to solve numerically and they facilitate physical understanding of nonlinear Lucassen waves, such as the threshold phenomenon. While linear Lucassen waves are highly attenuated on the scale of a wavelength, nonlinear Lucassen waves with an initial amplitude beyond threshold are significantly less attenuated over the same absolute distance. This fact has been used to connect Lucassen interface waves with the mechanical surface wave that accompanies the action potential during nerve pulse propagation.

The two evolution equations for Lucassen waves introduced in this work, the fixed-frame and moving-frame evolution equations, suffer shortcomings for strongly nonlinear propagation. The fixed-frame evolution equation

becomes numerically unstable and the moving-frame evolution equation fails at the moment a vertical tangent emerges in the waveform. These issues motivated the inclusion of viscosity in the interface. The intended purpose of including interface viscosity is to more accurately model attenuation of steep gradients in propagating waveforms. The viscoelastic evolution equation does exhibit greater attenuation for steep gradients and is more numerically stable than the fixed-frame evolution equation, even for a relatively small amount of viscosity. The behavior of these evolution equations near shock formation is investigated further in Chap. 4.

Chapter 4

The possibility of waveform overturning in selected nonlinear fractional models

4.1 Introduction

The formation of shocks, i.e., the formation of a nearly vertical tangent in propagating waveforms is a classical area of study in nonlinear acoustics. Model equations that allow for the formation of a true vertical tangent typically allow unphysical multivalued solutions as well. One such example is the lossless nonlinear Burgers equation. By analogy with waves on the surface of the ocean, the terminology "waveform overturning" was introduced to describe the unphysical waveforms implied by such model equations when the shock formation distance is exceeded.[56,57] Whereas water waves overturn and become multivalued due to their topology, a phenomenon familiar to surfers when the water surface is simultaneously beneath their feet and above their head, a longitudinal wave cannot be multivalued and possess more than one value of particle displacement at the same point in space. Prediction of a multivalued waveform indicates that essential physics, namely a mechanism that provides sufficient attenuation or dispersion, is not represented in the mathematical model. Without the addition of a term that provides sufficient attenuation or dispersion, the model equation fails beyond the point of shock formation.

Mathematical models that predict waveform overturning and thus multivalued waveforms rather than shock formation are not new. The exact equations for finite-amplitude sound in ideal fluids suffer from exactly this deficiency and perplexed the leading mathematical physicists of the 18th and 19th centuries until Stokes pointed out that viscosity is required to prevent waveform overturning. See Blackstock[58] for discussion of the controversies surrounding this matter in the early history of nonlinear acoustics.

Understanding which model equations allow for the formation of a vertical tangent is critical when performing numerical calculations. Traditional numerical approaches involving finite differencing techniques such as Runge-Kutta methods will fail beyond the formation of the vertical tangent in the waveform. For example, such algorithms cannot produce the multivalued waveforms predicted by the lossless nonlinear Burgers equation. Instead, the waveform predicted will appear reasonable to the user, but will nonetheless be incorrect and different from the result of evaluating the nonlinear Burgers equation with a very small amount of viscosity (which prevents vertical tangent formation).

As a specific example, consider Fig. 4.1, which shows numerical solutions of the moving-frame evolution equation, Eq. (3.49), for an initially sinusoidal waveform in the frequency and time domain for different distances. A description of frequency domain computational methods for evolution equations is given by Ginsberg and Hamilton[59] while a description of time domain methods is found in Sec. A.2. As discussed briefly in Sec. 3.3.6, the moving-

frame evolution equation will fail beyond some X for sufficient nonlinearity (bounds for uniformly valid solutions of the moving-frame evolution equation will be established in Sec. 4.3.3). In Fig. 4.1, the nonlinearity is chosen such that vertical tangent formation in the moving-frame evolution equation is possible,[51] at which point the moving-frame evolution equation fails.

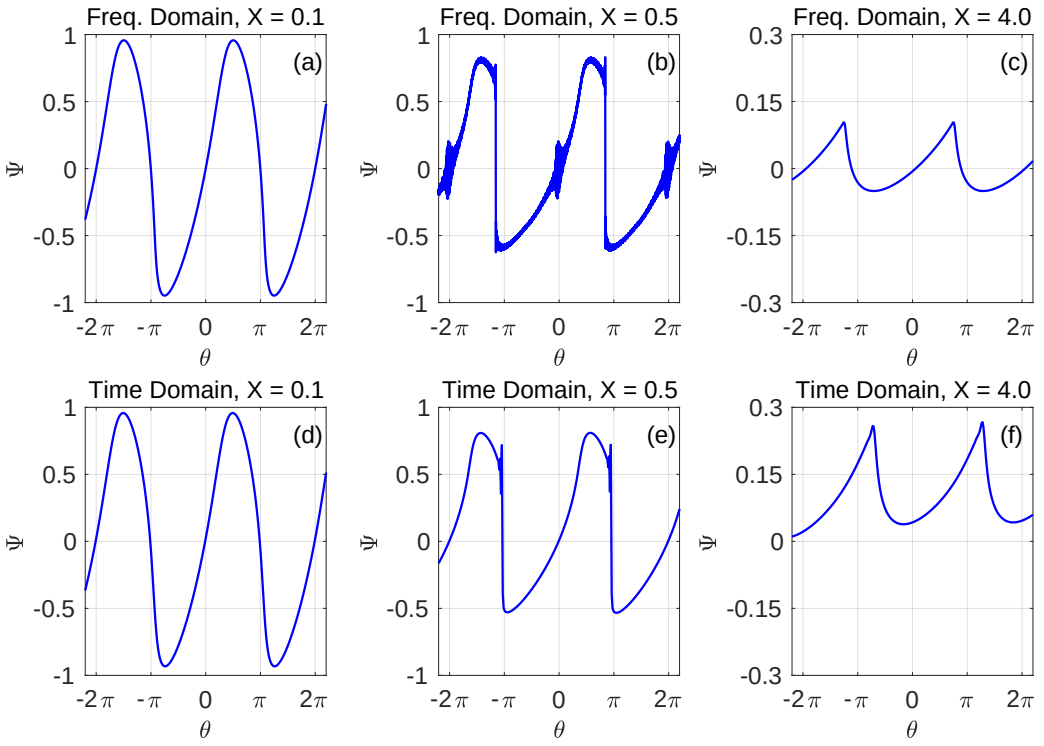

Figure 4.1: Numerical solution of the moving-frame evolution equation, Eq. (3.49), with $N_2 = -4$ and $N_3 = 4$ in the frequency domain [(a), (b), and (c)] and the time domain [(d), (e), and (f)]. The initial condition for the frequency domain algorithm is a sinusoid: $\Psi(0,\theta) = -\sin\theta$. In the time domain the initial condition is also a sinusoid, although it is windowed by a super Gaussian function: $\Psi(0,\theta) = -e^{-(\theta/12)^{12}}\sin\theta$.

Prior to shock formation, at $X = 0.1$ [Fig. 4.1(a) and (d)], solutions

obtained in both the frequency and time domain agree. However, at $X = 0.5$ [Fig. 4.1(b) and (e)] obvious indications of error begin to emerge. For the frequency domain solution, Fig. 4.1(b), spurious oscillations occur throughout the waveform. Because most conventional frequency domain algorithms cannot produce multivalued solutions, any computation past vertical tangent formation will artificially increase the amplitude of the higher harmonics, leading to spurious oscillations that are neither physical nor even valid as mathematical solutions of the original equation. At $X = 0.5$ for the time domain solution, Fig. 4.1(e), the visual indication of error is localized at the shock front. Conventional time domain approximations of derivatives, such as forward or backward finite difference approximations, fail at vertical tangent formation, leading to error that can manifest as oscillations near the vertical tangent as seen in Fig. 4.1(e). In the case of Fig. 4.1(e), a backward difference approximation is used to approximate the discrete derivative in the moving-frame evolution equation.

At $X = 4.0$ in Fig. 4.1(c) and (f) the predicted waveforms looks reasonable for both the frequency and time domain (i.e., there are no obvious indications of model failure). It is plausible that one might calculate a solution of the moving-frame evolution equation like the one presented in Fig. 4.1(c) or (f) without realization that vertical tangent formation has already occurred, and thus the model had failed by producing an invalid result even though the final result may appear valid. Also, notice that the predicted solutions of the frequency domain, Fig. 4.1(c), and the time domain, Fig. 4.1(f), do not agree

at $X = 4.0$ because of the numerical errors that occurred for both solutions before $X = 4.0$.

In the case of the frequency domain solution, it should be emphasized that the instability observed in Fig. 4.1(b) is not due to an insufficient number of frequencies used in numerical calculation (400 total frequencies are used for the frequency domain simulation in Fig. 4.1). Similarly, the failure of the time domain solution observed in Fig. 4.1(e) is not due to an insufficient time step. Rather, it is due to the fact that there is insufficient attenuation and dispersion in the model to prevent multivalued solutions from occurring, Most frequency and time domain numerical algorithms cannot produce such multivalued solutions. This example highlights why it is important to know if vertical tangent formation is possible, and thus subtle numerical failure is also possible, for a given nonlinear model equation.

The present chapter analyzes nonlinear waveforms with large gradients to determine if waveform overturning, and thus the possibility of failure for conventional numerical algorithms, is possible for fractional evolution equations. One could begin analysis with an equation that has the same form as the nonlinear Lucassen wave (KSSN) equation, Eq. (3.47), written here in the general form

$$\frac{\partial^\eta \xi}{\partial t^\eta} = c_{\eta,0}^2 \frac{\partial^2 \xi}{\partial x^2} + f\left(\xi, \frac{\partial \xi}{\partial t}, \frac{\partial \xi}{\partial x}, \ldots\right) \tag{4.1}$$

where the coefficient $c_{\eta,0}$ controls the rate at which the physical process evolves in time ($c_{\eta,0}$ can be interpreted as the small-signal sound speed for $\eta = 2$). The function f is an arbitrary function that describes the nonlinearity of the

system. In general, f could be a function of the wave variable ξ and any of its partial derivatives. However, analysis of Eq. (4.1) can be difficult. For example, forward marching numerical schemes are difficult to implement in x because Eq. (4.1) is typically formulated as a boundary value problem while marching schemes in t are inconvenient as well because traditional Runge-Kutta methods are not intended for fractional derivatives. Instead, it is much more manageable to analyze the following fractional evolution equation (also called the fractional transport equation[60]):

$$\frac{\partial^\nu \xi}{\partial t^\nu} + c_{\eta,0}\frac{\partial \xi}{\partial x} = g\left(\xi, \frac{\partial \xi}{\partial t}, \frac{\partial \xi}{\partial x}, \ldots\right) \tag{4.2}$$

where g is a function, possibly nonlinear, of ξ and its partial derivatives. The quantity ν is the order of the fractional time derivative. This new quantity is chosen because it is often different from the quantity η in Eq. (4.1).

When an evolution equation in the form of Eq. (4.2) is derived as an approximation of Eq. (4.1) one typically obtains $\nu = \eta/2$. The fixed-frame and moving-frame evolution equations, Eqs. (3.48) and (3.49), respectively, can be written in the form of Eq. (4.2). Equations in the form of (4.2) arise in numerous applications. As mentioned previously, such equations can be derived as approximations of the compound nonlinear fractional wave equation, Eq. (4.1), as is the case for the fixed-frame evolution equation. Other examples include fractional advection-dispersion equations[61] and fractional convection-diffusion equations[62] for propagation in complex media.

The present chapter considers the possibility of vertical tangent forma-

tion in solutions of the fixed-frame evolution equation, Eq. (3.48), the moving-frame evolution equation, Eq. (3.49), and the viscoelastic evolution equation, Eq. (3.72), as well as considering the general behavior of each of these equations when modeling propagation of waveforms with steep gradients. Section 4.2 investigates waveforms that develop a nearly vertical tangent when modeled using the fixed-frame and moving-frame evolution equations. Section 4.3 employs the intrinsic coordinates introduced by Hammerton and Crighton[56] to study the propagation of a waveform that is nearly a step-shock waveform. Appendix B considers the possbility of discontinuous solutions for fractional evolution equations using the formalism of Whitham.[30]

4.2 Analysis of a waveform with a nearly vertical tangent

This section analyzes the evolution of a waveform that is initially arbitrarily close to possessing a vertical tangent at $X = 0$, where X is the dimensionless spatial coordinate introduced in Eq. (3.46). The idea is to understand how the waveform changes over an infinitesimal step ΔX according to the fixed- and moving-frame evolution equations, Eqs. (3.48) and (3.49), respectively, especially to understand if a vertical tangent may occur. The fixed- and moving-frame evolution equations are presented again here for convenience.

Fixed-frame evolution equation:

$$\frac{\partial \Psi}{\partial X} = -\frac{\gamma}{1 + N_2 \Psi + N_3 \Psi^2} \frac{\partial^{3/4} \Psi}{\partial \phi^{3/4}} \tag{4.3}$$

Moving-frame evolution equation:

$$\frac{\partial \Psi}{\partial X} = (1 + N_2\Psi + N_3\Psi^2)\frac{\partial \Psi}{\partial \theta} - \gamma \frac{\partial^{3/4}\Psi}{\partial \theta^{3/4}} \tag{4.4}$$

The desired initial waveform is one that is arbitrarily close to possessing a vertical tangent, and which is simple and easy to analyze without the aid (and hinderance) of numerical approximations. A function that fits this description is a simple fractional monomial function. Consider an initial waveform that is represented by the following time waveform near $\phi = 0$:

$$\Psi_0(\phi) = \Psi(0, \phi) = \phi^a, \qquad 0 < a < 1 \qquad \text{for } \phi > 0 \tag{4.5}$$

The corresponding time derivative is thus

$$\frac{d\Psi_0}{d\phi}(\phi) = a\phi^{a-1} \tag{4.6}$$

where it is seen that a serves as a proxy for the steepness of the waveform near $\phi = 0$. As a approaches zero, the gradient defined in Eq. (4.6) is unbounded near $\phi = 0$. From the definition of Eq. (4.5), a will not equal zero exactly.

Figure 4.2 shows the initial waveform described by Eq. (4.5) for three different values of a. In Fig. 4.2, the lowest value, $a = 0.01$ (dot-dash curve), corresponds to a waveform with a larger gradient near $\phi = 0$ when compared to the largest value, $a = 0.4$ (dashed curve). Both curves approach a vertical tangent as ϕ approaches zero. As a gets closer to zero, the proximity to a vertical tangent becomes more pronounced (as $a \to 0$ the waveform more closely resembles a step shock like the dot-dash curve in Fig. 4.2).

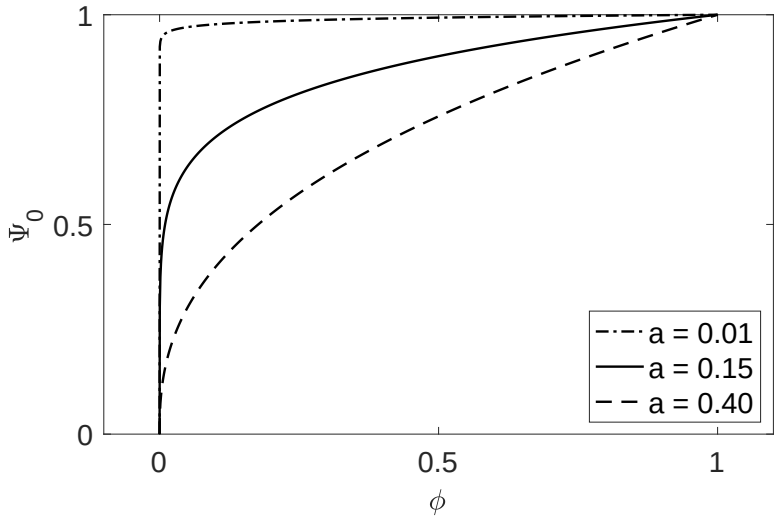

Figure 4.2: Initial waveform described by Eq. (4.5) with $a = 0.01$ (dot-dash curve), $a = 0.15$ (solid curve), and $a = 0.40$ (dashed curve.)

Equation (4.5) is valid only for $\phi > 0$, such that a true vertical tangent is not yet formed. Equation (4.5) loses physical significance for very large ϕ because $\Psi_0(\phi)$ is unbounded for $a > 0$ (i.e., $\Psi_0 \to \infty$ as $\phi \to \infty$). However, the region of interest here is only near the point of vertical tangent formation, so only the range $0 < \phi \lesssim 1$ is important. The restriction $a > 0$ is imposed on the exponent so that the function remains finite for small ϕ. Finally, the fractional derivative of Eq. (4.5) is[25]

$$\frac{\partial^\nu \Psi_0}{\partial \phi^\nu}(\phi) = \frac{\Gamma(a+1)}{\Gamma(a+1-\nu)} \phi^{a-\nu} \ , \qquad \nu > 0 \tag{4.7}$$

where Γ is the Gamma function.

As previously stated, the goal of the present analysis is to understand the evolution of initial waveforms described qualitatively by Eq. (4.5) over an

infinitesimal step in X using the fixed- and moving-frame evolution equations to see if vertical tangent formation can occur. Because the waveform described by Eq. (4.5) is already infinitesimally close to having a vertical tangent, any further increase in the gradient near $\phi = 0$ could result in the formation of a true vertical tangent.

To facilitate understanding of the behavior of the waveform it is useful to analyze the "slowness," i.e., the reciprocal of wave speed, of each point on the waveform. In general, the slowness of a forward-traveling progressive waveform with wave variable Ψ and coordinates X and ϕ is defined by[63]

$$\left.\frac{d\phi}{dX}\right|_{\Psi} = -\frac{\partial\Psi/\partial X}{\partial\Psi/\partial\phi} \tag{4.8}$$

For example, for the general fractional evolution equation given by Eq. (4.2) let $g = 0$ and $\nu = 1$ ($\eta = 2$) which yields

$$c_{2,0}\frac{\partial\xi}{\partial x} = -\frac{\partial\xi}{\partial t} \tag{4.9}$$

where $c_{2,0}$ is this context is interpreted as the sound speed. Equation (4.9) is an evolution equation for a lossless, linear, progressive wave traveling forward uniformly with speed $c_{2,0}$. With Eq. (4.8) used for the wave variable ξ in the coordinates x and t, the slowness corresponding to Eq. (4.9) for any arbitrary waveform is

$$\left.\frac{dt}{dx}\right|_{\xi} = -\frac{\partial\xi/\partial x}{\partial\xi/\partial t} = \frac{1}{c_{2,0}} \tag{4.10}$$

As expected in Eq. (4.10), the slowness for every point on the waveform is the reciprocal of the wave speed $c_{2,0}$. The slowness describes how the waveform moves in a time window relative to different propagation distances. For

increasing x (and taking increasing x to mean rightward), a positive slowness indicates rightward propagation and negative slowness indicates leftward propagation for an incremental step in x.

To understand how slowness provides insight into whether vertical tangent formation is possible during nonlinear propagation, consider as an example the sawtooth waveform in Fig. 4.3. An arbitrary slowness of the waveform is overlain in Fig. 4.3 with blue arrows indicating its magnitude and direction. A slowness dependence similar to that depicted in Fig. 4.3 could come from the function g in Eq. (4.2). The slowness depicted in Fig. 4.3 indicates that the waveform will steepen for the next small step in x. If the directions of the arrows were reversed, the waveform would relax for the next small step in x. The schematic in Fig. 4.3 demonstrates how the slowness of a waveform gives insight to the behavior of the waveform. A slowness profile similar to that depicted in Fig. 4.3 could be obtained using the lossless Burgers equation in conjunction with Eq. (4.8) (in that case the magnitudes of the arrows would not be the same as they are in Fig. 4.3).

In the case of the fractional monomial initial condition, Eq. (4.5), propagating according to the fixed- and moving-frame evolution equations, the slowness can be calculated using the ϕ derivative of the initial condition, Eq. (4.6), with the X derivative calculated using the fixed-frame and moving-frame evolution equations, Eqs. (4.3) and (4.4), respectively. Unlike the example waveform in Fig. 4.3, the fractional monomial, Eq. (4.5), is already arbitrarily close to vertical tangent formation (i.e., the waveform gradient is unbounded near

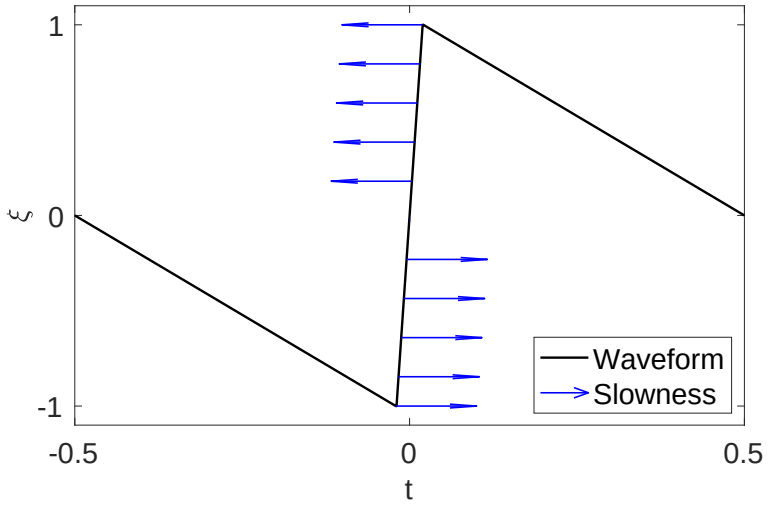

Figure 4.3: Example sawtooth waveform at some point x_0. The arrows describe an arbitrarily selected slowness that would indicate steepening the waveform for the next incremental step in x.

$\phi = 0$). Therefore, any further increase in the waveform gradient near $\phi = 0$ will indicate that vertical tangent formation is possible.

While analysis using Eq. (4.8) can be done with the retarded time θ instead of ϕ, it is convenient to recast the moving-frame evolution equation, Eq. (4.4), which is expressed as a function of of the retarded time θ, in the fixed time ϕ. The moving-frame evolution equation Eq. (4.4) expressed in fixed coordinates will be labeled the alternative fixed-frame evolution equation:

Alternative fixed-frame evolution equation:

$$\frac{\partial \Psi}{\partial X} = (N_2\Psi + N_3\Psi^2)\frac{\partial \Psi}{\partial \phi} - \gamma \frac{\partial^{3/4}\Psi}{\partial \phi^{3/4}} \tag{4.11}$$

It is important to note that the alternative fixed-frame evolution equation,

Eq. (4.11), is fundamentally linked to the moving-frame evolution equation, Eq. (4.4). The only difference is the coordinate system in which these equations are expressed. The nonlinearity, attenuation, and dispersion properties of Eqs. (4.4) and (4.11) are consistent. The significant conclusions in this section that are made concerning the alternative fixed-frame evolution equation thus apply to the moving-frame evolution equation as well. The fixed-frame and alternative fixed-frame evolution equations, Eqs. (4.3) and (4.11), are exactly the same in the linear case, i.e., $N_2 = N_3 = 0$.

The slowness of the initial waveform, Eq. (4.5), is found in the same manner as the example presented in Eq. (4.10). The slownesses predicted by Eqs. (4.3) and (4.11), respectively, are:

Slowness of fixed-frame evolution equation, Eq. (4.3):

$$\left.\frac{d\phi}{dX}\right|_{\Psi} = \frac{\gamma\Gamma(a)}{\Gamma(a+1-\nu)}\left(\frac{\phi^{1/4}}{1+N_2\phi^a+N_3\phi^{2a}}\right) \tag{4.12}$$

Slowness of alternative fixed-frame evolution equation, Eq. (4.11):

$$\left.\frac{d\phi}{dX}\right|_{\Psi} = -\left(N_2\phi^a+N_3\phi^{2a}\right) + \frac{\gamma\Gamma(a)}{\Gamma(a+1-\nu)}\phi^{1/4} \tag{4.13}$$

Equations (4.12) and (4.13) reveal that the slowness of the waveform approaches zero for $\phi \to 0$ for both the fixed- and alternative fixed-frame evolution equations, respectively. That is, the leading edge of the waveform at $\phi = 0$, as shown in Fig. 4.2, is fixed in place. Therefore, for vertical tangent formation to be possible the slowness of the initial waveform must be negative as it approaches zero, i.e., $d\phi/dX < 0$ for ϕ very close to zero.

The negative slowness would indicate that the part of the waveform in the region of ϕ very close to zero would travel backward for an incremental step in X, or equivalently, to the left. This would indicate a steepening of the waveform described by Eq. (4.5), similar to what is depicted for the sawtooth waveform in Fig. 4.3. Because the waveform is infinitesimally close to a vertical tangent near $\phi = 0$, the leftward movement of points on the waveform would increase the magnitude of the gradient in this region and would thus suggest that waveform overturning could be mathematically possible. [It should also be noted that in a fixed time coordinate, leftward movement of any part of the waveform would violate causality in addition to giving rise to a multivalued solution. Preserving causality is another important reason to understand the limits of Eqs. (4.3) and (4.11)].

The slowness of the fixed-frame evolution equation, Eq. (4.12), can only be negative if

$$1 + N_2\phi^a + N_3\phi^{2a} < 0 \tag{4.14}$$

However, for Eq. (4.14) to be satisfied, a negative elastic modulus (in the context of Lucassen waves) is required, which is prohibited on physical grounds. In fact, any region of the waveform that satisfies Eq. (4.14) would grow in amplitude because the sign of the fractional derivative in Eq. (4.3) would be reversed for that region. This amplitude growth is unphysical for nearly every real scenario, not just Lucassen waves. With the condition (4.14) prohibited, the slowness described by Eq. (4.12) cannot be negative and therefore will not produce a vertical tangent. Figure 4.4(a) shows the initial waveform, Eq. (4.5),

with arrows depicting slowness as calculated with Eq. (4.12). The rise time of the transition from $\Psi = 0$ to $\Psi = 1$ increases continuously for $\phi \leq 1$.

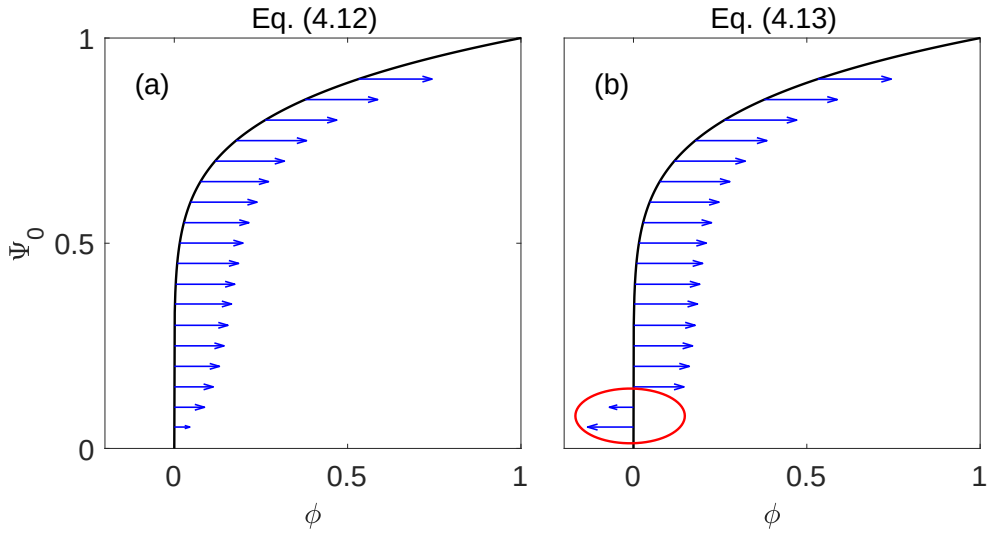

Figure 4.4: Plot of the initial waveform, Eq. (4.5), with arrows indicating the direction and approximate magnitude of the (a) the fixed-frame evolution equation slowness, Eq. (4.12), and (b) the alternative fixed-frame evolution equation slowness, Eq. (4.13). In this example, $N_2 = 0.9$ and $N_3 = 0$.

The slowness of the alternative fixed-frame evolution equation, Eq. (4.13), is negative for $a < 1/4$ in the region near $\phi = 0$ as long as N_2 is positive. For $a = 1/4$, the slowness described by Eq. (4.13) is negative for

$$N_2 > \frac{\gamma\Gamma(a)}{\Gamma(a+1-\nu)} \tag{4.15}$$

Similarly, for $N_2 = 0$ and $N_3 > 0$ then the slowness is negative for $a < 1/8$ in the region near $\phi = 0$ and for $a = 1/8$ with

$$N_3 > \frac{\gamma\Gamma(a)}{\Gamma(a+1-\nu)} \tag{4.16}$$

In general, a very small value of a (which indicates a very steep waveform) leads to leftward propagation (in the context of Fig. 4.4) near $\phi = 0$ for the alternative fixed-frame evolution equation. Therefore vertical tangent formation should be possible for the alternative fixed-frame evolution equation. This conclusion holds for the original formulation of the moving-frame evolution equation, Eq. (4.4), because the moving coordinates only produce a uniform translation of the waveform in the retarded time frame. Figure 4.4(b) shows the initial waveform, Eq. (4.5), with arrows depicting the slowness calculated with Eq. (4.13). The waveform steepens in the region near $\phi = 0$ (this region is indicated by the red circle).

The viscoelastic evolution equation, Eq. (3.72), does not have a known analytical solution for the convolution integral for the initial waveform described by Eq. (4.5). However, because the viscoelastic evolution equation has a form similar to that of the fixed-frame evolution equation (in fact, the viscoelastic evolution equation becomes the fixed frame evolution equation in the limit of zero viscosity), the behavior should be similar to that observed with the fixed-frame evolution equation; that is, vertical tangent formation would not be possible with the prescribed initial condition.

The possibility of vertical tangent formation in solutions of the moving-frame evolution equation is an expected result because it can be written in the form of a nonlinear Burgers equation with an attenuation coefficient proportional to ω^ν with exponent $\nu < 1$. Equations of this form do not provide sufficient attenuation in terms of its increase as a function of frequency to

prevent the formation of a vertical tangent in the presence of sufficiently high nonlinearity.[53]

Instead, consider a nonlinear wave with attenuation proportional to ω^ν, where $1 < \nu < 3$, modeled by the following Burgers-type equation:

$$\frac{\partial \Psi}{\partial X} = (N_2 \Psi + N_3 \Psi^2) \frac{\partial \Psi}{\partial \theta} + \gamma \frac{\partial^\nu \Psi}{\partial \theta^\nu} \tag{4.17}$$

Notice that the time coordinate θ is the moving time coordinate originally defined in Eq. (3.46). Besides the difference in the time coordinate, Eq. (4.17) has a form very similar to that of the alternative fixed-frame evolution equation, Eq. (4.11), except that the sign of the fractional time derivative is positive and the order of the fractional time derivative is taken to be $\nu > 1$. The sign change is required to prevent unphysical amplitude growth for power-law attenuation exponents $1 < \nu < 3$ because the sign of the attenuation coefficient is reversed for $\nu < 1$ versus $\nu > 1$.[53] Stated in another way, the attenuation coefficient α defined in Eq. (2.14) reverses sign at $\eta = 2$ for the compound fractional wave equation, Eq. (2.12), which for an evolution equation in the form of Eq. (4.2) corresponds to $\nu = 1$. Therefore, to model attenuation instead of unphysical exponential growth in Eq. (4.17) the sign in front of γ must be positive for $1 < \nu < 3$. A wave propagating according to Eq. (4.17) will actually go backward (to the left) relative to the moving time coordinate θ in the absence of nonlinearity ($N_2 = N_3 = 0$), which is seen in Fig. 4.5. In Fig. 4.5(a) linear propagation predicted by the alternative fixed-frame evolution equation, Eq. (4.11) (with $0 < \nu < 1$), is forward (to the right), while

in Fig. 4.5(b) linear propagation predicted by Eq. (4.17) (with $1 < \nu < 3$) is backward (to the left).

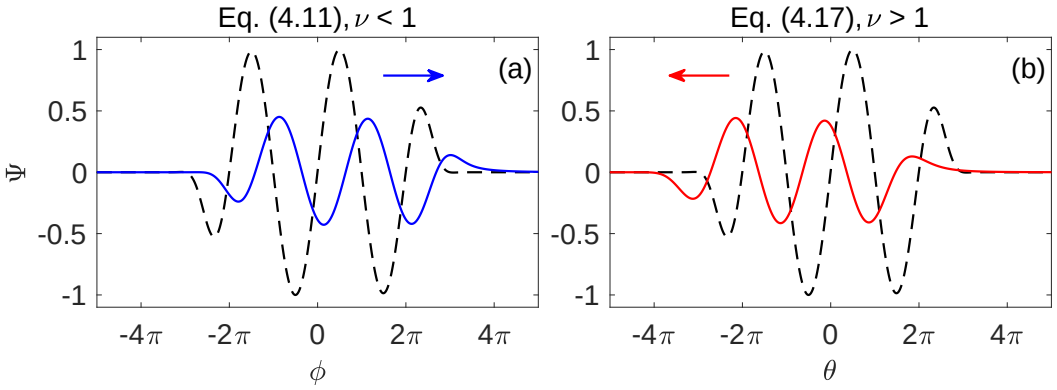

Figure 4.5: Solutions at $X = 2$ with $N_2 = N_3 = 0$ and $\gamma = 1.0842$ for the alternative fixed-frame evolution equation, Eq. (4.11), with $\nu = 0.75$ [(a), blue curve] and the evolution equation, Eq. (4.17), with $\nu = 1.25$ [(b), red curve]. The initial condition, indicated by the dashed line, is defined in Eq. (3.74). In (a), the waveform propagates forward (to the right), while in (b) the waveform propagates backward (to the left). The arrows indicate the direction of propagation.

The slowness corresponding to Eq. (4.17), which is calculated using Eq. (4.8) except that the left-hand side is positive instead of negative since the propagation is now in the opposite direction and the time coordinate is θ instead of ϕ, is

$$\left.\frac{d\phi}{dX}\right|_{\Psi} = \left(N_2\theta^a + N_3\theta^{2a}\right) + \frac{\gamma\Gamma(a+1)}{a\Gamma(a+1-\nu)}\theta^{1-\nu} \tag{4.18}$$

Equation (4.18) reveals that the slowness of the waveform now approaches $-\infty$ for $\phi \to 0$ for $a < (\nu - 1)$. This is different from the slowness near $\phi = 0$ for the fixed- and alternative fixed-frame evolution equations, Eqs. (4.12) and (4.13),

respectively, which approaches zero at the leading edge of the shock. Therefore the gradient of the waveform must decrease near the shock front regardless of the degree of nonlinearity (the values of N_2 and N_3) because the points closer to $\theta = 0$ (the location of the shock front) will always propagate faster backward (to the left) than the points behind it. It follows that the initial waveform, described by Eq. (4.5), will relax and vertical tangent formation will not occur. This is consistent with the prior result that vertical tangent formation is impossible for a nonlinear Burgers equation that exhibits power-law attenuation for which $\nu > 1$. The relation between power-law attenuation and the possibility of vertical tangent formation is discussed at length by Cormack and Hamilton.[53]

In the present section, it was shown that the fixed-frame evolution equation, Eq. (4.3), does not permit vertical tangent formation for the prescribed initial condition, Eq. (4.5). The alternative fixed-frame evolution equation, Eq. (4.11), does permit vertical tangent formation for sufficient nonlinearity. The analysis performed for the alternative fixed-frame evolution equation applies to the moving-frame evolution equation, Eq. (4.4). Finally, a generalized Burgers-type equation, Eq. (4.17), with a fractional time derivative of order $1 < \nu < 3$ that accounts for attenuation and dispersion was considered. Equation (4.17) does not permit multivalued solutions regardless of the amount of nonlinearity because the loss provided by the fractional derivative with exponent $\nu > 1$ is always sufficient to prevent vertical tangent formation.

4.3 Analysis of fractional waves using intrinsic coordinates

Another way to the investigate the possibility of vertical tangent formation in fractional waveforms is using the intrinsic coordinates introduced by Hammerton and Crighton[56] and employed subsequently by Cormack and Hamilton.[53] Intrinsic coordinates also provide insight into the numerical stability of the various evolution equations: the fixed-frame, moving-frame, and viscoelastic evolution equations.

The coordinates employed in this transformation are the arc length s along the waveform and the angle Θ of the tangent to the waveform. In the case of the general fractional evolution equation, Eq. (4.2), the spatial coordinate x is unchanged. Propagation of the waveform is described by $\Theta(x, s)$ instead of $\xi(x, t)$. The transformation is defined by

$$\Theta = \tan^{-1}(\partial\xi/\partial t) \qquad s = \int_0^t \sqrt{1 + (\partial\xi/\partial t)^2}\, dt \tag{4.19}$$

For the case of the non-dimensional coordinates used in the viscoelastic and fixed-frame evolution equations, in Eq. (4.19) replace ξ with Ψ, replace t with ϕ, and replace x with X. For the moving-frame evolution equation one would instead replace t with θ in Eq. (4.19).

Figure 4.6 provides visualization of the intrinsic coordinate transformation. The waveform in physical coordinates, shown as the blue curve in Fig. 4.6(a) and (b), is a smoothed-out step shock described locally by $\xi = t^{1/3}$. The waveform in intrinsic coordinates, determined by the transformations in

Eqs. (4.19), is shown in Fig. 4.6(c). The red point on the waveform in intrinsic coordinates in Fig. 4.6(c) corresponds to the red point on the physical waveform in Fig. 4.6(a) and (b). The arc length of the red portion of the curve depicted in Fig. 4.6(a) is the s coordinate of the red point in Fig. 4.6(c), and the angle of the tangent to the waveform depicted in Fig. 4.6(b) is the Θ coordinate for the red point in Fig. 4.6(c).

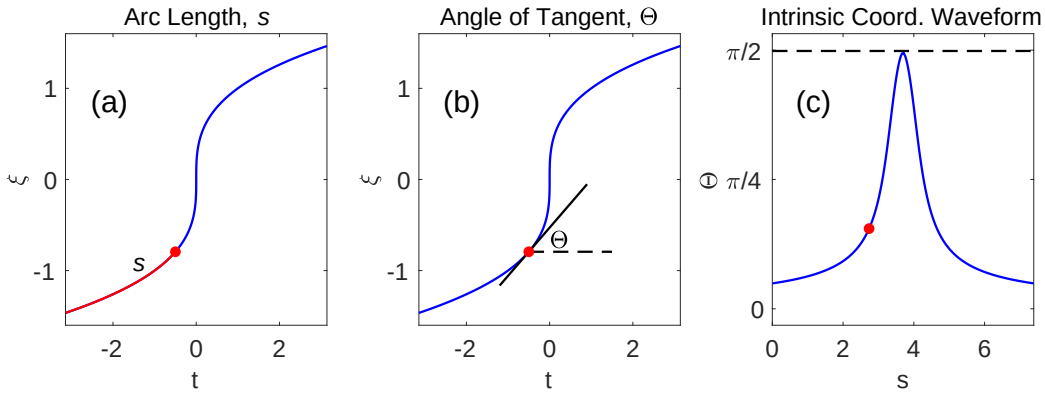

Figure 4.6: Plot of the waveform $\xi = \xi_0(t/t_0)^{1/3}$ where ξ_0 and t_0 are chosen to be unity. In plots (a) and (b) the waveform is plotted in intrinsic coordinates while in plot (c) the waveform is plotted in intrinsic coordinates. The length of the red portion of the curve in (a), which is the arc length s, and the angle Θ of the tangent in (b) are used to relate the red point in physical coordinates in (a) and (b) to the red point in intrinsic coordinates shown in (c).

Of particular interest in the present section is how vertical tangent formation is captured in intrinsic coordinates. For the waveform in physical coordinates in Fig. 4.6(a) and (b) a vertical tangent exists at $t = 0$, i.e., $\partial\xi/\partial t = \infty$ at $t = 0$. By Eq. (4.19), this point corresponds to $\Theta = \pi/2$ in intrinsic coordinates. In general, any point on a given waveform in in-

trinsic coordinates for which $|\Theta| = \pi/2$ corresponds to a vertical tangent in physical coordinates. This highlights perhaps the most significant advantage of intrinsic coordinates: while traditional numerical schemes, such as finite differencing techniques, fail at vertical tangent formation for waveform propagation in physical coordinates, the same waveform in intrinsic coordinates is still single valued. In fact, intrinsic coordinates can be used to accurately calculate multivalued solutions of the lossless nonlinear Burgers equation for $\Theta > \pi/2$ in intrinsic coordinates.[53]

The transformations in Eqs. (4.19) along with the derivations by Cormack and Hamilton[53] are used to transform the evolution equation in physical coordinates, Eq. (4.2), into the following evolution equation in intrinsic coordinates:

$$\frac{\partial \Theta}{\partial x} = \frac{\partial F}{\partial s} + \frac{\partial \Theta}{\partial s} \int F \frac{\partial \Theta}{\partial s}\, ds \tag{4.20}$$

where the function F [not directly related to f in Eq. (4.1)] depends on the exact form of the original evolution equation. As noted above, intrinsic coordinates allow for the computation of waveform propagation with very steep gradients that would otherwise be very unstable or impossible to calculate numerically.

4.3.1 Analysis of the fixed-frame evolution equation in intrinsic coordinates

Consider first the fixed-frame evolution equation, Eq. (4.3). To simplify the expressions involving F, the coefficient N_2 is set to zero. It is straightfor-

ward to incorporate the terms involving N_2, but the expressions become overly burdensome and distracting for the present purposes. This choice also has to do with the fact that there is a more strict physical restriction for N_2 in order for the left side of Eq. (4.14) to remain positive in the context of Lucassen waves. For sinusoidal waveforms with an amplitude of unity and $N_3 = 0$, the condition $|N_2| < 1$ must be fulfilled or, during propagation, the left side of Eq. (4.14) will become negative at some point in the waveform. On the other hand, if $N_2 = 0$, as long as $N_3 > -1$ then the left side of Eq. (4.14) will remain positive. Therefore, higher amplitudes (and thus greater nonlinearity) can be easily modeled when N_2 is set to zero.

While $\nu = 3/4$ in the fixed-frame evolution equation, Eq. (4.3), the more general relation $0 \leq \nu \leq 1$ is now considered. The function F for the fixed-frame evolution equation (with $N_2 = 0$) in intrinsic coordinates is

$$F = \frac{\gamma F_\nu}{1 + N_3 \left(\int \sin\Theta \; ds \right)^2} \tag{4.21}$$

where the loss function F_ν,[53] which is related to the fractional time derivative in Eq. (4.3), is

$$F_\nu = -(\cos\Theta)^{1-\nu} \frac{\partial^\nu}{\partial s^\nu} \int \sin\Theta \; ds \tag{4.22}$$

The derivatives of the functions F and F_ν with respect to s are

$$\frac{\partial F}{\partial s} = \frac{\gamma\left(\partial F_\nu/\partial s\right)\left[1+N_3\left[\left(\int \sin\Theta\ ds\right)^2\right]\right] - 2\gamma F_\nu\left(N_3 \sin\Theta \int \sin\Theta\ ds\right)}{\left[1+N_3\left(\int \sin\Theta\ ds\right)^2\right]^2} \tag{4.23}$$

$$\frac{\partial F_\nu}{\partial s} = (1-\nu)\sin\Theta\sec^\nu\Theta\frac{\partial\Theta}{\partial s}\frac{\partial^\nu}{\partial s^\nu}\int \sin\Theta\ ds - \cos^{1-\nu}\Theta\frac{\partial^{\nu+1}}{\partial s^{\nu+1}}\int \sin\Theta\ ds \tag{4.24}$$

To obtain Eq. (4.24) it was assumed that the distributive property of fractional derivatives holds.[25] As stated previously, vertical tangent formation corresponds to $|\Theta| = \pi/2$, and $|\Theta| > \pi/2$ indicates a multivalued solution. As $|\Theta|$ approaches $\pi/2$, Eqs. (4.23) and (4.24) can become unstable when solved numerically because the term $\sec\Theta$ in Eq. (4.24) approaches ∞. If vertical tangent formation is possible for the fixed-frame evolution equation for a given value of N_3, then $|\Theta|$ will equal $\pi/2$ at some finite value of X.

We now consider intrinsic coordinate waveforms with a maximum value of $\Theta = \pi/2$, i.e., at the point of vertical tangent formation in physical coordinates. The goal here is to understand properties of the fixed-frame evolution equation for nonlinear waveforms with a vertical tangent. Of particular interest is numerical stability.

Consider the tangent angle $\Theta(\overline{X}, s)$ at a distance $\overline{X}$ that is infinitesimally close to $\pi/2$. The function $\Theta(\overline{X}, s)$ will be relabeled $\overline{\Theta}(s)$ to indicate its sole dependence on s (since the analysis will take place at a fixed distance $\overline{X}$). Assume that the segment of the waveform where the angle $\overline{\Theta}$ is approaching

$\pi/2$ is concave down. Under these conditions the segment of interest in the waveform does not include an "end point" in s. See Fig. 4.7 for a graphical illustration. The first point in the waveform $\overline{\Theta}(s)$ where the angle equals $\pi/2$ is the maximum $\overline{\Theta}_{\max}$. Let the position of $\overline{\Theta}_{\max}$ in the waveform be $s = s_{\max}$. The maximum of any differentiable curve corresponds to a zero in the first derivative:

$$\left.\frac{d\overline{\Theta}}{ds}\right|_{s=s_{\max}} = 0 \tag{4.25}$$

In addition to $\overline{\Theta}$ being finite, it is also assumed that the terms $d\overline{\Theta}/ds$ and

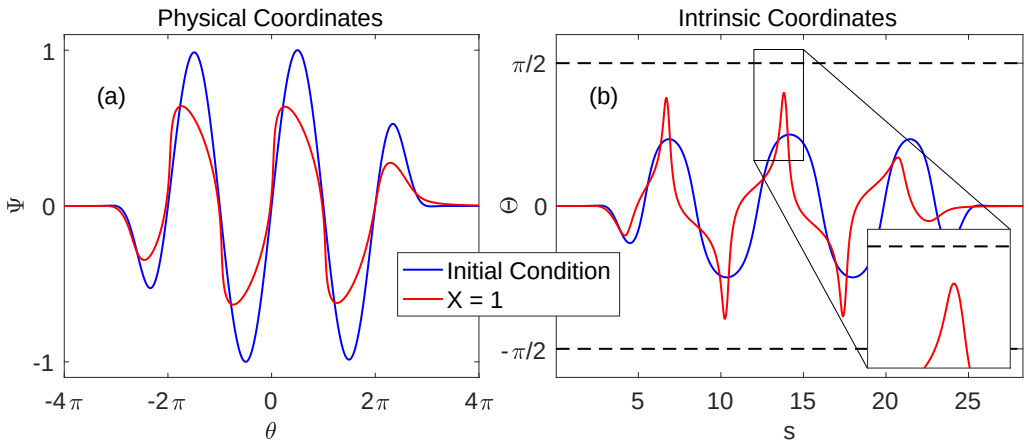

Figure 4.7: Solution of the moving-frame evolution equation with the initial condition defined in Eq. (3.74) in physical coordinates (a) and in intrinsic coordinates (b). The values $N_2 = 0$ and $N_3 = 1.5$ are used. The portion of $\Theta(s)$ at $X = 1$ in intrinsic coordinates [zoomed-in portion of the red curve in (b)] is concave down as Θ approaches $\pi/2$.

$d^2\overline{\Theta}/ds^2$ are finite everywhere in s. Therefore, $\overline{\Theta}$ is at least class C^2 smooth,

and the following quantities are finite for all s:

$$\frac{d^{\nu}}{ds^{\nu}} \int \sin \overline{\Theta} \; ds, \quad \frac{d^{\nu+1}}{ds^{\nu+1}} \int \sin \overline{\Theta} \; ds, \quad \int \sin \overline{\Theta} \; ds \tag{4.26}$$

At the point where $\overline{\Theta}_{\max} = \pi/2$ a vertical tangent has formed and $\cos \overline{\Theta} = 0$. With the assumption that all the terms in Eq. (4.26) are finite, one obtains $F_{\nu} = F = 0$. The quantities $\partial F/\partial s$ and $\partial F_{\nu}/\partial s$ are not as easy to interpret. Because $F_{\nu} = 0$, from Eq. (4.23) it can be seen that $\partial F/\partial s$ is proportional to $\partial F_{\nu}/\partial s$. Therefore, to understand behavior of the evolution equations near vertical tangent formation, investigation of the term $\partial F_{\nu}/\partial s$, Eq. (4.24), is necessary. Because $\cos \overline{\Theta} = 0$ and $\sin \overline{\Theta} = 1$ at $\overline{\Theta} = \pi/2$, Eq. (4.24) can be reduced to

$$\frac{\partial F_{\nu}}{\partial s} = (1 - \nu) \left(\frac{d\overline{\Theta}/ds}{\cos^{\nu} \overline{\Theta}} \bigg|_{\overline{\Theta}=\pi/2} \right) \frac{d^{\nu}}{ds^{\nu}} \int \sin \overline{\Theta} \; ds \quad \text{at} \quad \overline{\Theta} = \pi/2 \tag{4.27}$$

where the quantities in Eq. (4.27) are finite and nonzero except for $d\overline{\Theta}/ds$ and $(\sec \overline{\Theta})^{\nu}$ [it is assumed that the fractional derivative in Eq. (4.27) is nonzero, which is true as long as the waveform is not a precise shape such that the convolution integral in Eq. (2.2) is exactly zero]. Therefore, the behavior of $\partial F_{\nu}/\partial s$ at $\overline{\Theta} = \pi/2$, Eq. (4.27), depends on the following indeterminate ratio:

$$\frac{d\overline{\Theta}/ds}{\cos^{\nu} \overline{\Theta}} \bigg|_{\overline{\Theta}=\pi/2} \tag{4.28}$$

Equation (4.28) is indeterminate because both the numerator and denominator on the left-hand side go to zero as $\overline{\Theta} \to \pi/2$ and $d\overline{\Theta}/ds \to 0$. To

evaluate Eq. (4.28), and thus understand the behavior of the evolution equations near vertical tangent formation in intrinsic coordinates, use a Taylor series expansion for Θ about $s = s_{\max}$:

$$\overline{\Theta} = \overline{\Theta}\big|_{s=s_{\max}} + \frac{d\overline{\Theta}}{ds}\bigg|_{s=s_{\max}} (s - s_{\max}) + \frac{1}{2}\frac{d^2\overline{\Theta}}{ds^2}\bigg|_{s=s_{\max}} (s - s_{\max})^2 + ... \quad (4.29)$$

To simplify Eq. (4.29) let

$$A = \overline{\Theta}\big|_{s=s_{\max}}, \quad B = \frac{d\overline{\Theta}}{ds}\bigg|_{s=s_{\max}}, \quad C = -\frac{1}{2}\frac{d^2\overline{\Theta}}{ds^2}\bigg|_{s=s_{\max}} \quad (4.30)$$

The negative sign is introduced for the constant C in Eq. (4.30) to render the coefficient C positive because it is assumed that $\overline{\Theta}$ is concave down. Using Eq. (4.25) it can be shown that $B = 0$. Equation (4.29) at second order thus becomes

$$\overline{\Theta} = A - C(s - s_{\max})^2 + O[(s - s_{\max})^3] \quad (4.31)$$

One more Taylor expansion is necessary to properly interpret Eq. (4.28). Consider the Taylor series expansion of $(\cos\overline{\Theta})^\nu$ about $\overline{\Theta} = \pi/2$:

$$(\cos\overline{\Theta})^\nu = \left(\frac{\pi}{2} - \overline{\Theta}\right)^\nu - \frac{\nu}{6}\left(\frac{\pi}{2} - \overline{\Theta}\right)^{2+\nu} + O\left[(\pi/2 - \overline{\Theta})^{(4+\nu)}\right] \quad (4.32)$$

The point of interest is where $A = \overline{\Theta}_{\max} = \pi/2$, which corresponds to vertical tangent formation in physical coordinates. Now substitute Eq. (4.31) into Eq. (4.32) and retain only the leading order term:

$$(\cos\overline{\Theta})^\nu \approx [C(s - s_{\max})^2]^\nu \quad (4.33)$$

The Taylor series, Eq. (4.31), is differentiated with respect to s to obtain the leading order term of $d\Theta/ds$, which is written here as

$$\frac{d\overline{\Theta}}{ds} \approx -2C(s - s_{\max}) \quad (4.34)$$

We thus have expansions for both the numerator, Eq. (4.34), and denominator, Eq. (4.33), in Eq. (4.28). Substitution of the expanded numerator and denominator into Eq. (4.28) yields

$$\frac{d\overline{\Theta}/ds}{(\cos\overline{\Theta})^{\nu}} = -\frac{2C(s-s_{\max})}{[C(s-s_{\max})^2]^{\nu}} = -2C^{1-\nu}(s-s_{\max})^{1-2\nu} \tag{4.35}$$

Equation (4.35) can be used to determine the behavior of waveforms propagating according to the more general form of the fixed-frame evolution equation (with $0 < \nu < 1$) near the point $s = s_{\max}$ (i.e., exactly at the point where $\overline{\Theta} = \pi/2$ and vertical tangent formation occurs). Figure 4.8 shows the behavior of the term in Eq. (4.35) for various values of ν. For $0 < \nu < 1/2$, as $s \to s_{\max}$ the term in Eq. (4.35) approaches zero. This corresponds to the dashed curve in Fig. 4.8, for which $\nu = 0.4$. Therefore $\partial F_{\nu}/\partial s = 0$ for a vertical tangent in physical coordinates. For $\nu > 1/2$, as $s \to s_{\max}$ the term in Eq. (4.35) has no limit (it does not approach one single value); for $s < s_{\max}$ the term in Eq. (4.35) approaches ∞ while for $s > s_{\max}$ it approaches $-\infty$. The behavior of Eq. (4.35) for $\nu > 1/2$ is depicted in Fig. 4.8 with the dot-dash line. The dot-dash line corresponds to $\nu = 0.6$ and it approaches $+\infty$ from the left side but approaches $-\infty$ from the right side. The mathematical singularity in the dot-dash line indicates numerical instability near $\overline{\Theta} = \pi/2$. In the fixed-frame evolution equation one has $\nu = 3/4 > 1/2$. For $\nu = 1/2$ exactly, the term in Eq. (4.35) also does not approach a single value, and instead there is a discontinuity at $s = s_{\max}$. The curve for $\nu = 0.5$ in Fig. 4.8 approaches different finite values from the left- and right-hand sides, respectively.

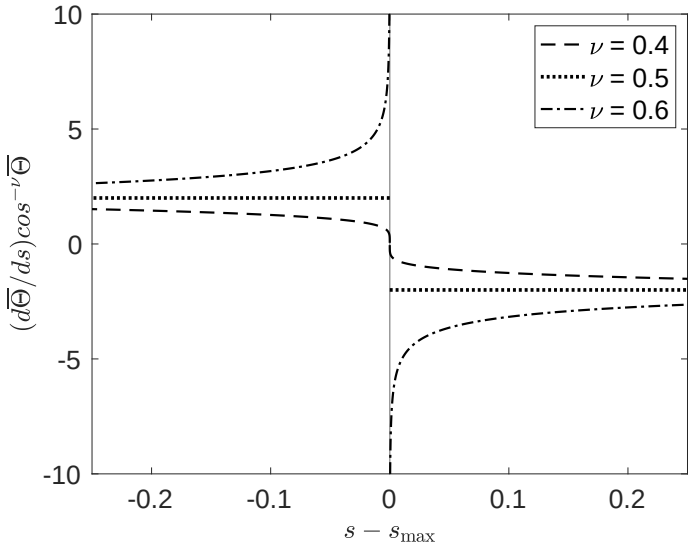

Figure 4.8: Plot of Eq. (4.35) with $C = 1$ for $\nu = 0.4$, $\nu = 0.5$, and $\nu = 0.6$.

It should be reiterated that while Fig. 4.8 only depicts the behavior of Eq. (4.35), Eq. (4.35) is directly related to $\partial F_\nu/\partial s$, which significantly impacts the X derivative of a waveform in intrinsic coordinates, described by Eq. (4.20). If the term in Eq. (4.35) does not approach a single finite value as a vertical tangent forms, then numerical solutions of wave propagation in intrinsic coordinates will not be stable for waveforms with steep gradients because, in general, numerical algorithms do not handle the mathematical singularities in the curves for $\nu = 0.5$ and $\nu = 0.6$ in Fig. 4.8 very well. Fractional diffusive waves, including the Lucassen waves modeled by the fixed-frame evolution equation, typically have a time derivative for which the order is in the range $1/2 < \nu < 1$. Therefore, the mathematical singularity at

$s = s_{\max}$ in the curve for $\nu = 0.6$ can lead to numerical instability near very steep gradients in physical coordinates.

4.3.2 Propagation of a step shock with finite rise time in intrinsic coordinates

The analysis of the fixed-frame evolution in Sec. 4.3.1 is not easily repeated for the viscoelastic and moving-frame evolutions equations because of their functional forms. Instead, the propagation of a waveform that is a step shock with a smooth transition region is considered in the present section, using the fixed-frame, moving-frame, and viscoelastic evolution equations in intrinsic coordinates. The goal is to investigate the properties of these three evolution equations for propagation of a nonlinear waveform with a large gradient. Thus consider the following initial condition defined in intrinsic coordinates:

$$\Theta(0, s) = \pi/2\,(1 - \varepsilon)\,\mathrm{sech}[(s - s_{\max})/s_0] \tag{4.36}$$

where s_0 is a constant that determines the width of the sech pulse, and $\varepsilon \ll 1$ is a dimensionless parameter that controls how close $\Theta(0, s_{\max})$ is to $\pi/2$. Equation (4.36) approximates a smooth step shock in physical coordinates. Figure 4.9(a) and (b) shows the initial condition in intrinsic and physical coordinates, respectively, while Fig. 4.9(c) shows the numerical evaluation of the derivative with respect to X according to the fixed-frame evolution equation, Eq. (4.3), using Eq. (4.20) for $\epsilon = 0$ (i.e., a vertical tangent does exist). The behavior shown in the numerically calculated curve presented in Fig. 4.9(c) is proportional to the behavior of Eq. (4.35) with $\nu > 1/2$ ($\nu = 0.6$ in Fig. 4.8), as

expected.

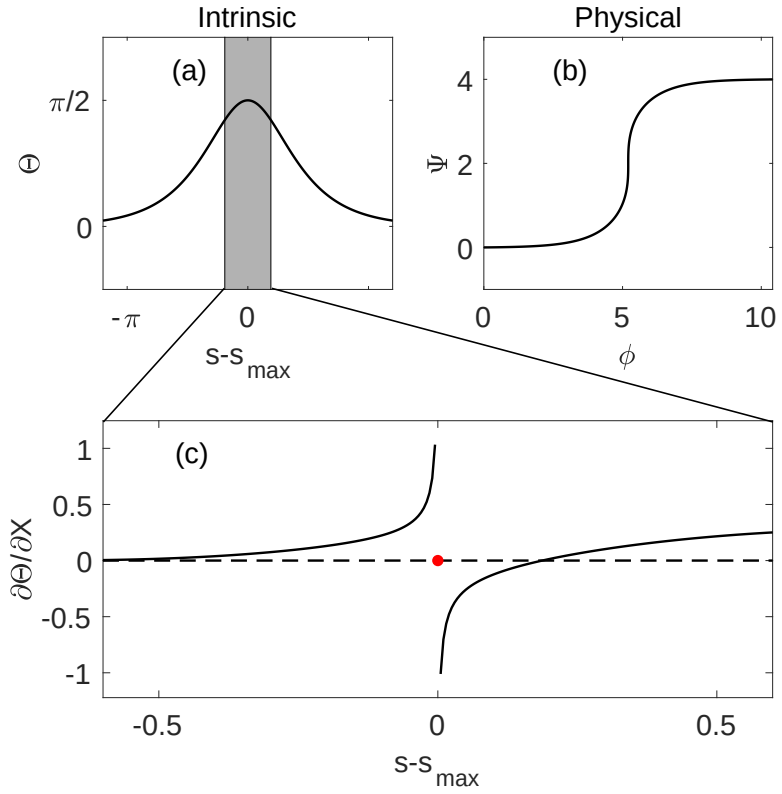

Figure 4.9: Plot (a) shows the initial condition, Eq. (4.36), with $\epsilon = 0$. Plot (b) shows the corresponding waveform in physical coordinates and (c) plot of the initial spatial gradient according to Eq. (4.20) for the fixed-frame evolution equation with $N_2 = 0$, $N_3 = 2$, and $\nu = 3/4$. The solid curve in (c) is qualitatively similar to the case $\nu = 0.6$ in Fig. 4.8.

The derivative with respect to X can also be calculated numerically with the viscoelastic evolution equation, Eq. (3.72), in intrinsic coordinates. Figure 4.10 highlights the stability advantages of the viscoelastic evolution equation. The spatial gradient of the initial condition, Eq. (4.36) with $\epsilon = 10^{-4}$, is shown for the fixed-frame evolution equation, Fig. 4.10(a), and the vis-

coelastic evolution equation, Fig. 4.10(b). This initial condition corresponds to a smooth step function that has nearly developed a vertical tangent. In Fig. 4.10(a) a discontinuity is beginning to emerge at $s = s_{\max}$, while in Fig. 4.10(b) there is no jump in the s derivative of $\Theta(0, s)$ developing at all. The point $s = s_{\max}$ is indicated by the red dot in Figs. 4.10 and 4.11. The smoother curve predicted by the viscoelastic evolution equation in Fig. 4.10(b) is indicative of the greater stability of the viscoelastic evolution equation when compared with the fixed-frame evolution equation in Fig. 4.10(a). For calculations in physical coordinates, this difference manifests itself as greater stability for the viscoelastic evolution equation for the propagation of waveforms with steep gradients.

For another example, consider the Burgers equation with an attenuation coefficient proportional to ω^{ν}, which is defined in Eq. (4.17). As stated previously in Sec. 4.2, for the Burgers equation with $\nu < 1$, formation of a vertical tangent is possible. In contrast, for $\nu > 1$, a vertical tangent cannot form, regardless of the magnitude of nonlinearity. Equation (4.20) is used to calculate spatial gradients of Eq. (4.17) with $\nu = 0.75$ [Fig. 4.11(a)] and $\nu = 1.25$ [Fig. 4.11(b)]. Recall that the sign of the fractional derivative in Eq. (4.17) flips depending on whether ν is greater than or less than one. The initial condition is once again defined by Eq. (4.36) with $\epsilon = 10^{-3}$. In Fig. 4.11(a), the spatial gradient at $s = s_{\max}$ is positive, indicating that an infinitesimal step forward in X will result in the angle Θ increasing. An increase in Θ corresponds to the curve steepening in physical coordinates closer to true vertical

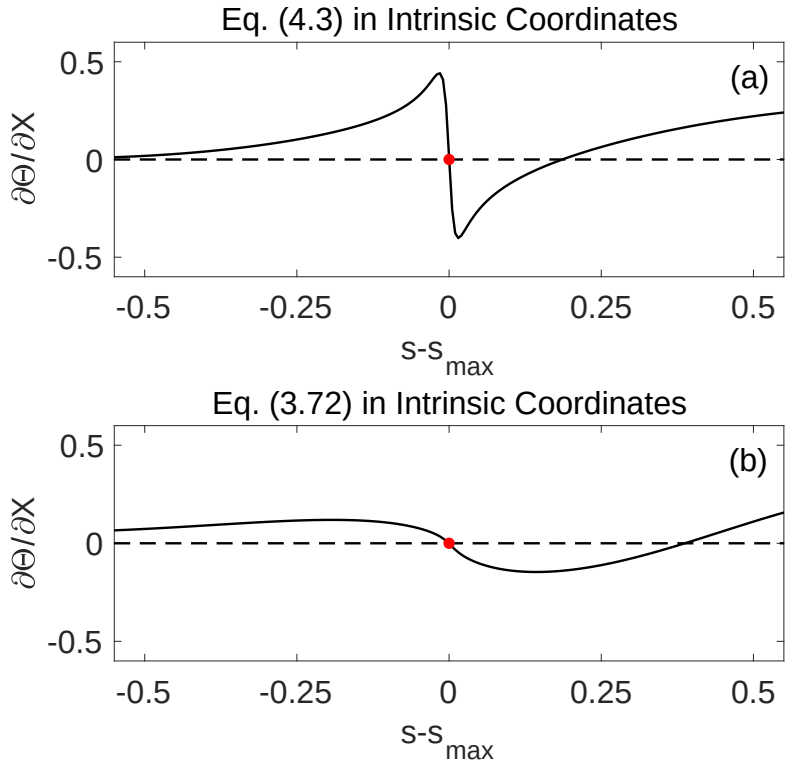

Figure 4.10: Initial spatial gradient in intrinsic coordinates predicted by (a) the fixed-frame evolution equation, Eq. (4.3), and (b) the viscoelastic evolution equation, Eq. (3.72). Here the initial condition Eq. (4.36) with $\epsilon = 10^{-4}$ is used while $N_2 = 0$, $N_3 = 2$, $\nu = 3/4$, and $\Omega = 0.1$.

tangent formation. In Fig. 4.11(b), the spatial gradient is negative at $s_{\max}$, indicating that an infinitesimal step forward in X will result in a decrease in Θ, i.e., the steepest part of the shock will relax. Once again, the present analysis confirms the prior result that a Burgers-type evolution equation with power-law attenuation characterized by the exponent $\nu > 1$ cannot form a vertical tangent.[53]

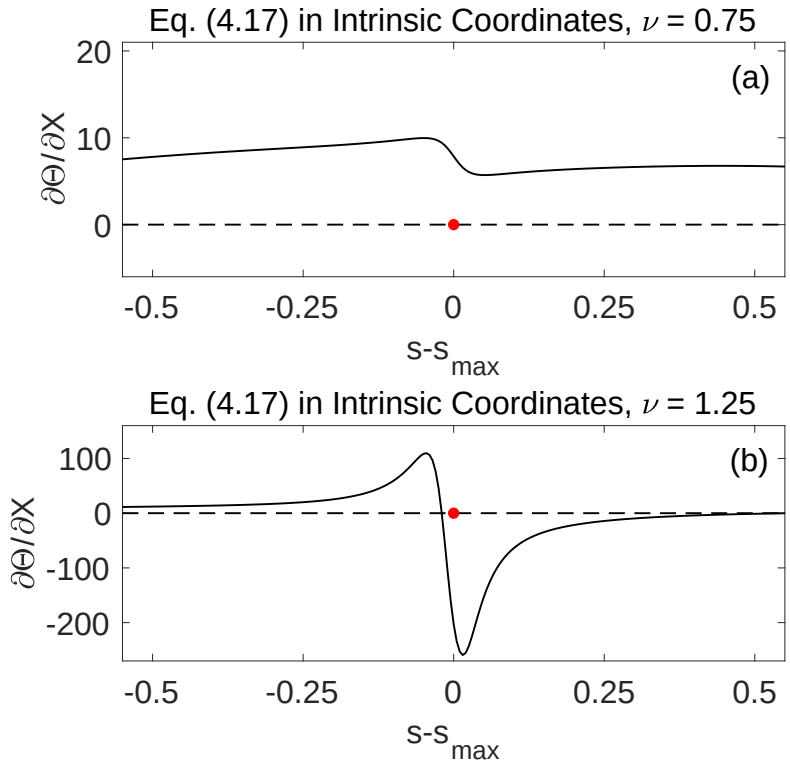

Figure 4.11: Initial spatial gradient in intrinsic coordinates predicted by the nonlinear Burgers equation in fixed coordinates, Eq. (4.17), (a) with $\nu = 3/4$ and (b) with $\nu = 5/4$. Here the initial condition Eq. (4.36) with $\epsilon = 10^{-3}$ is used while $N_2 = 0$ and $N_3 = 2$.

4.3.3 Limits on the moving-frame evolution equation

The moving-frame evolution equation for Lucassen wave propagation, Eq. (4.4), is a specific example of a Burgers equation with power-law attenuation with $\nu = 3/4 < 1$. Therefore, as hinted at in Sec. 3.3.6 and verified in Sec. 4.2, vertical tangent formation is possible for Eq. (4.4). Intrinsic coordinates can be used to precisely determine the limits in which conventional numerical schemes can be used for the moving-frame evolution equation. For

any given source waveform there is a closed curve $C(N_2, N_3)$ that separates the (N_2, N_3) parameter space into two regions. In the region where both $|N_2|$ and $|N_3|$ are sufficiently small that the values (N_2, N_3) are enclosed by C, solutions of the equation are uniformly valid out to any propagation distance. When the values (N_2, N_3) lie outside the region enclosed by C, the attenuation and dispersion are insufficient to stabilize shock formation beyond the distance where a vertical tangent first appears in the waveform and thus traditional numerical algorithms will fail.

Following the method of Cormack and Hamilton,[53] the curve C associated with Eq. (4.4) can be calculated using intrinsic coordinates with Eq. (4.20) by solving forward in X until either $|\Theta| = \pi/2$, indicating that shock formation has occurred in physical coordinates, or until $|\Theta|$ begins to decrease, indicating that attenuation is sufficient to prevent vertical tangent formation. Through multiple iterations the critical values of (N_2, N_3) that result in vertical tangent formation are found.

The curve C is presented in Fig. 4.12 for $N_2 \leq 0$ and $N_3 \geq 0$, corresponding to the coefficients of nonlinearity $\beta_2 < 0$ and $\beta_3 > 0$, which are defined in Eq. (3.52), associated with the interface elasticity parameters reported by Kappler et al.[20] The calculations were performed for an initially sinusoidal source waveform, $\Psi = \sin\theta$ at $X = 0$. For example, in the absence of cubic nonlinearity ($N_3 = 0$) and with $|N_2| \gtrsim 1$, Fig. 4.12 indicates that vertical tangent formation is predicted by Eq. (4.4) at a finite distance from the source, and beyond which waveform overturning will occur. When (N_2, N_3) lies

within the region enclosed by curve C, the moving-frame evolution equation is uniformly valid because it accounts for sufficient attenuation and dispersion to prevent vertical tangent formation, and it thus describes nonlinear evolution of the waveform out to any distance. This analysis indicates that the moving-frame evolution equation should only be used as an approximation to the KSSN fraction wave equation, Eq. (3.47), for a moderate to low amount of nonlinearity such that (N_2, N_3) are contained within the curve in Fig. 4.12.

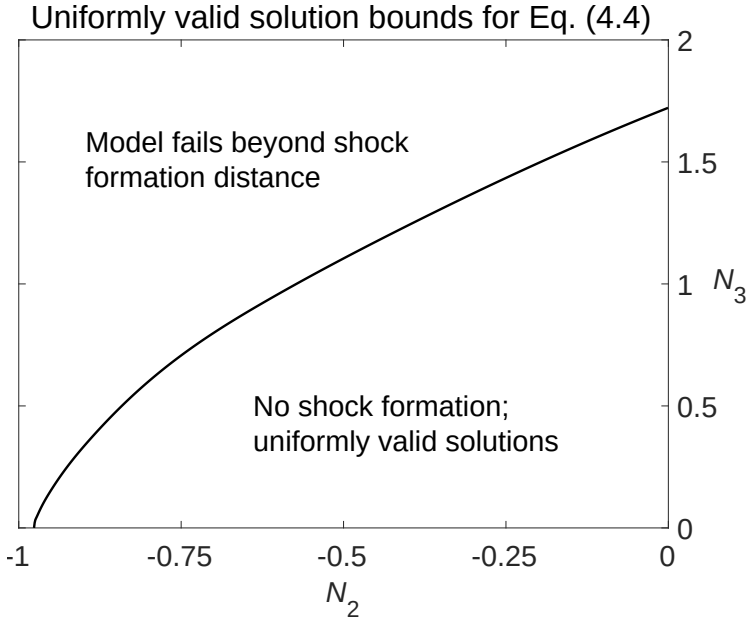

Figure 4.12: Parameter space enclosed by curve C for $N_2 < 0$ and $N_3 > 0$ where Eq. (4.4) yields uniformly valid solutions for nonlinear propagation of an initially sinusoidal waveform, because vertical tangent formation does not occur.

4.4 Conclusion

This chapter was devoted to analyzing nonlinear propagation of waveforms with steep gradients in both physical and intrinsic coordinates. The models considered include the fixed-frame [Eq. (4.3)], moving-frame [Eq. (4.3)], viscoelastic [Eq. (3.72)], and augmented Burgers [Eq. (4.17)] evolution equations.

Section 4.2 demonstrated that the moving-frame evolution equation permits the formation of a vertical tangent in the waveform provided the nonlinearity in the system is sufficiently strong. On the other hand, the fixed-frame evolution equation predicts relaxation of the given initial condition, regardless of the magnitude of nonlinearity, provided the condition (4.14) is not fulfilled for any region of the waveform. While the conclusion that the fixed-frame evolution equation does not allow vertical tangent formation holds only for the specific waveform defined in Eq. (4.5), it is reasonable to presume that this conclusion holds for any arbitrary waveform since any arbitrary waveform will have a lower gradient than the waveform defined in Eq. (4.5), which possesses an unbounded gradient. The difference in the possibility of vertical tangent formation during propagation for the fixed-frame evolution equation and the moving-frame evolution equation may be due to the difference in the functional form of each equation.

While the fixed-frame evolution may not permit vertical tangent formation, Sec. 4.3 demonstrated that the fixed-frame evolution equation can be unstable for waveforms with steep gradients. This conclusion follows from

the mathematical singularity that appears in intrinsic coordinates for the spatial derivative predicted by the fixed-frame evolution equation, as shown in Fig. 4.9. The added interface viscosity which leads to the viscoelastic evolution equation helps to stabilize the numerical calculation of the propagation of waveforms containing steep gradients. Therefore even though evidence in the present work suggests that the fixed-frame evolution equation does not permit vertical tangent formation, it still may be necessary to use the viscoelastic evolution equation in cases with steep waveform gradients, especially for computational purposes. It should also be noted that the viscosity in the interface that results in the viscoelastic evolution equation is not a form of artificial viscosity introduced *ad hoc* to increase numerical stability; it is a small, but physically present property of a given interface. Finally, intrinsic coordinates are used to place specific bounds on the nonlinearity of the moving-frame evolution equation such that vertical tangent formation will not occur and numerical solutions will be uniformly valid.

Chapter 5

Conclusion

The initial inspiration for this work was the possibility that a mechanical wave may play a role in neurological communication, as highlighted in a 2018 Scientific American article by Fox that provides historical perspective on this point of view.[1] Lucassen waves have been proposed for this mechanical disturbance, and at a minimum they share various properties with the electric action potential, as discussed in Chaps. 1 and 3. This line of research soon transitioned into an analysis of fractional waves in general, rather than a focus exclusively on the fractional Lucassen wave. The emphasis on fractional calculus is due to our belief that there is considerable untapped modeling potential for fractional wave equations. Fractional derivatives can be used to model dispersion and attenuation that more conventional integer-order derivatives cannot. As numerical methods for evaluating fractional derivatives become more efficient and standard,[37] it is anticipated that there will be an increase in the use of fractional derivatives for modeling lossy wave propagation in unconventional media.

5.1 Summary

In Chap. 2 the Caputo formalism of fractional derivatives is introduced. The traditional wave equation with a second-order space derivative and a second-order time derivatives is converted into a fractional wave equation by replacing the integer-order time derivative with a fractional time derivative. It is emphasized that this is different from adding a term with a fractional time derivative to the existing d'Alembertian wave operator in the wave equation, as is done for acoustic waves exhibiting power-law attenuation.[28] Fractional wave equations inherently predict dispersion and attenuation that satisfy Kramers-Kronig relations (see Chap. 2). In the case of a "superdiffusion" process, the fractional wave equation predicts behavior in between that predicted by the conventional wave equation (which possesses a second derivative with respect to time) and the diffusion (heat) equation (which possesses a first derivative with respect to time). Once considered a niche subject, fractional calculus is now being employed in modeling a wide variety of physical systems.[40,44–47]

As mentioned, the fractional wave that motivated this thesis research is the Lucassen wave, which is discussed in depth in Chap. 3. The nonlinear Lucassen wave shares a number of properties with the mechanical wave that accompanies the electric action potential in nerve axons during cell-to-cell communication, as has been shown both analytically and experimentally.[12–17,20] Two evolution equations for progressive nonlinear Lucassen waves, which are of reduced order relative to the original equation published by Kappler et al.[20] in 2017, are derived in Chap. 3. These equations are considerably easier

to integrate numerically, and also to investigate analytically, than the original equation of Kappler et al. One is referred to as the fixed-frame evolution equation and the other as the moving-frame evolution equation. The fixed-frame evolution equation exhibits better agreement with the equation of Kappler et al. when compared to the moving-frame evolution equation. While both the fixed- and moving-frame evolution equations exhibit the "all-or-none" principle that is associated with the electric action potential, the specific form of the moving-frame evolution equation reveals that this principle can be explained as competition between quadratic and cubic nonlinearity in the wave speed.[51] An evolution equation was also derived for nonlinear Lucassen waves taking into account viscosity in the membrane interface. The viscosity in the interface, which is traditionally assumed to be small and negligible in frequency ranges of interest, is included because nonlinear propagation produces harmonics at high frequencies. The high frequencies become important at amplitudes for which shock formation occurs because they ultimately define the structure and thickness of the shock front. Since attenuation increases with frequency, even a small increase in viscosity can result in a significant change in shock structure and thickness. For nonlinear propagation, the inclusion of interface viscosity thus results in greater attenuation of waveforms with large gradients (thin shocks) and also greater stability in numerical calculations.

A classical problem in nonlinear acoustics is the determination of whether a vertical tangent may form during nonlinear propagation of a wave. For example, a vertical tangent is predicted for sound waves in fluids by the lossless

Burgers equation. At the point where the vertical tangent forms, the equation fails because the next step in the calculation results in an unphysical multi-valued solution. The possibility of vertical tangent formation for an equation modeling fractional wave propagation has not previously been investigated in the literature, so this idea is explored in Chap. 4. Section 4.3.3 recovers the prior result that an equation in the form of the moving-frame evolution equation does permit vertical tangent formation.[51] For the cases considered in Chap. 4, the fixed-frame evolution equation does not appear to permit vertical tangent formation. Section 4.3 also employs intrinsic coordinates to explain why the evolution equation with interface viscosity is more stable numerically for very nonlinear propagation when compared with the fixed-frame evolution equation.

The question of whether a mechanical wave plays an essential role in neural cell-to-cell communication remains without a consentaneous answer. This question is not answered in the present thesis, but the insights gained regarding propagation of nonlinear Lucassen waves and more general nonlinear fractional waves may add to the discussion of neurological communication one day, as well as increase knowledge of fractional calculus within the acoustics community.

5.2 Possible future work

To model Lucassen waves as the mechanical disturbance in nerve axons, coupling with the electric action potential and with the internal pressure

wave in the internal axonic fluid must be taken into account. This has been considered previously,[19] but directly modeling the interface disturbance as a fractional wave has not yet been attempted. It is possible that a coupling mechanism is essential for the propagation of Lucassen waves over long distances because of how rapidly linear Lucassen waves are attenuated as a function of distance. Accounting for a feedback system between the interface wave and the energy from surrounding ion channels within the membrane of the axon is thus worthy of future pursuit.

There are also various experiments that can be performed to validate the conclusions in this thesis. Lucassen presents experimental results validating the linear Lucassen wave dispersion relation[22] and Kappler et al. present some experimental evidence[20] for their proposed nonlinear Lucassen wave equation, but more validation would be valuable, especially related to the "all-or-none" threshold phenomena discussed in Sec. 3.3.5. Experiments on longitudinal wave propagation at a viscoelastic interface where the interface viscosity is not negligible would be valuable as well to better understand the differences in the propagation of Lucassen waves with and without noticeable viscosity in the interface membrane, especially for nonlinear propagation.

Appendices

Appendix A

Numerical methods used

A.1 Numerical approximations of fractional derivatives in the time domain

Because a substantial portion of the analysis in this thesis involves fractional derivatives, it is essential to be able to evaluate them numerically. Fractional derivatives can be easily evaluated in the frequency domain using Eq. (2.1); however, this limits analysis to periodic waveforms. Instead, it is more convenient to evaluate the fractional derivatives numerically in the time domain using Eq. (2.2). The algorithm introduced in this section is based on the work of Li et al.[37]

Consider a fractional time derivative of the Caputo variety[25] with a lower integration limit of 0 written here as

$$ {}_0^C D_t^\eta f(t) = \frac{d^\eta f(t)}{dt^\eta} = \frac{1}{\Gamma(m-\eta)} \int_0^t \frac{d^m f(t')/dt'^m}{(t-t')^{\eta+1-m}} dt' \ , \quad m = \lceil \eta \rceil \qquad \text{(A.1)} $$

where η is the order of the fractional derivative, $\lceil \eta \rceil$ is the first integer greater than the value of the non-integer η, t is the time coordinate, $f(t)$ is some arbitrary time-dependent function, and Γ is the gamma function. The Caputo fractional derivative is thus evaluated in the time domain using a convolution

integral. For the following derivation, it is assumed that $0 < \eta < 1$ and therefore $m = 1$.

Let the time coordinate t be discretized according to $t_n = n\Delta t$, where Δt is the step size which is constant. To evaluate the fractional derivative numerically at time $t = t_n$ the convolution integral is expressed as follows:

$$\left.\frac{d^\eta f(t)}{dt^\eta}\right|_{t=t_n} = \frac{1}{\Gamma(1-\eta)} \sum_{j=0}^{n-1} \int_{t_j}^{t_{j+1}} \frac{df(t')/dt'}{(t_n - t')^\eta} dt' \tag{A.2}$$

No approximation has yet been made in Eq. (A.2). For sufficiently small Δt the derivative $df(t')/dt'$ can be approximated as a constant over the intervals in Eq. (A.2) and thus removed from the integrand in Eq. (A.2) to obtain the approximation

$$\left.\frac{d^\eta f(t)}{dt^\eta}\right|_{t=t_n} = \frac{1}{\Gamma(1-\eta)} \sum_{j=0}^{n-1} \left.\frac{df(t')}{dt'}\right|_{t'=t_{j+1/2}} \int_{t_j}^{t_{j+1}} \frac{1}{(t_n - t')^\eta} dt' \tag{A.3}$$

In Eq. (A.3) the derivative $df(t')/dt'$ is evaluated at the time $t_{j+1/2}$ for each term in the summation. This is accomplished using a central finite difference approximation, which is expressed as

$$\left.\frac{df(t')}{dt'}\right|_{t'=t_{j+1/2}} \simeq \frac{f(t_{j+1}) - f(t_j)}{\Delta t} \tag{A.4}$$

The remaining integral in Eq. (A.3) may now be evaluated:

$$\int_{t_j}^{t_{j+1}} \frac{1}{(t_n - t')^\eta} dt' = -\frac{1}{1-\eta}\Big[(t_n - t_{j+1})^{1-\eta} - (t_n - t_j)^{1-\eta}\Big] \tag{A.5}$$

Rewriting Eq. (A.5) in terms of the constant time step Δt yields

$$\int_{t_j}^{t_{j+1}} \frac{1}{(t_n - t')^\eta} dt' = -\frac{(\Delta t)^{1-\eta}}{1-\eta}\Big[(n-j-1)^{1-\eta} - (n-j)^{1-\eta}\Big] \tag{A.6}$$

Equations (A.4) and (A.6) are substituted into Eq. (A.3) to obtain the following numerical approximation for fractional derivatives in the time domain:

$$\begin{aligned}\left.\frac{d^\eta f(t)}{dt^\eta}\right|_{t=t_n} =& \frac{1}{\Gamma(1-\eta)}\sum_{j=0}^{n-1}\frac{f(t_{j+1})-f(t_j)}{\Delta t} \\ & \times\left\{\frac{-(\Delta t)^{1-\eta}}{1-\eta}\Big[(n-j-1)^{1-\eta}-(n-j)^{1-\eta}\Big]\right\} \\ =& -\frac{\Delta t^{-\eta}}{\Gamma(2-\eta)}\sum_{j=0}^{n-1}\left[f(t_{j+1})-f(t_j)\right]\Big[(n-j-1)^{1-\eta}-(n-j)^{1-\eta}\Big]\end{aligned} \tag{A.7}$$

Finally, it is convenient to rewrite Eq. (A.7) in the more compact form

$$\left.\frac{d^\eta f(t)}{dt^\eta}\right|_{t=t_n} = \frac{(\Delta t)^{-\eta}}{\Gamma(2-\eta)}\sum_{j=0}^{n} d_{n,j} f(t_j) \quad \text{for } 0<\eta<1 \tag{A.8}$$

where

$$d_{n,j} = \begin{cases}(n-1)^{1-\eta}-n^{1-\eta} & j=0 \\ (n-j-1)^{1-\eta}-2(n-j)^{1-\eta}+(n-j+1)^{1-\eta} & 1\le j\le n-1 \\ 1 & j=n\end{cases} \tag{A.9}$$

The approximation expressed by Eqs. (A.8) and (A.9) is given by Li et al.[37]

The steps in Eqs. (A.2)–(A.7) leading to Eq. (A.8) are not limited to $0<\eta<1$ in Eq. (A.1). For $\eta>1$, according to Eq. (A.1), the time derivative in Eq. (A.4) will be of higher-order than one. A finite difference stencil different from Eq. (A.4) would be necessary to approximate time derivatives of higher-order than one. The rest of the analysis in Eqs. (A.6) and (A.7) would be the same, although the resulting expression for $d_{n,j}$ would be different for $\eta>1$. Even for $0<\eta<1$, a different finite difference stencil can be used in

Eq. (A.4) to achieve higher-order accuracy for the numerical approximation of the derivative at time $t' = t_{j+1/2}$. The function $d_{n,j}$ is dependent not only on η, but also on the specific type of finite difference stencil that is used to approximate the derivative in Eq. (A.3). Li et al.[37] report error estimates for numerical schemes that solve simple fractional partial differential equations with a fractional derivative approximation similar to Eq. (A.8).

A.2 Numerical schemes for solving evolution equations

Numerical solutions of the fixed-frame, moving-frame, and viscoelastic evolution equations, Eqs. (3.48), (3.49), and (3.72), respectively, that are presented in this thesis were obtained using the method of lines.[64] The method of lines is a general numerical scheme for solving partial differential equations in which the derivatives with respect to every coordinate except for one are represented by finite difference approximations, and the remaining coordinate is integrated, either analytically or numerically, to obtain a solution. In the present work, the method of lines is used to reduce a partial difference equation into a system of coupled differential equations that are formulated as initial value problems.

In the case of the moving-frame evolution equation, Eq. (3.49), the θ derivative of order one is approximated with a second-order central difference and the fractional θ derivative is approximated with Eq. (A.8). The moving-frame evolution equation is integrated forward in the X coordinate. Let the θ coordinate be uniformly discretized with the mesh size $\Delta\theta$ such that $\theta_n = n\Delta\theta$.

At a given time the wave variable is discretized with $\Psi_n(X) = \Psi(X, \theta_n)$. The moving-frame evolution equation can then be written in the discretized form

$$\frac{\partial \Psi_n}{\partial X} = \left(1 + N_2 \Psi_n + N_3 \Psi_n^2\right)\left(\frac{\Psi_{n+1} - \Psi_{n-1}}{\Delta\theta}\right) - \frac{\gamma(\Delta\theta)^{-3/4}}{\Gamma(5/4)} \sum_{j=0}^{n} d_j \Psi_j \quad \text{(A.10)}$$

To accomplish forward integration of the discretized form of the moving-frame evolution equation, Eq. (A.10), a Runge-Kutta method with adaptive time stepping is used. We chose the RK3(4) method derived by Fehlberg.[65] The Butcher tableau[66] for RK3(4) is shown in Table A.1. To carry out the numerical integration of Eq. (A.10) the wave variable Ψ is stored as a column vector containing $\Psi_n(X)$ at each time θ_n so that Eq. (A.10) can be written as a system of coupled ordinary differential equations. The boundaries in time at $\theta = \theta_0$ and $\theta = \theta_{\max} = \theta_N$ (where $N + 1$ is the total number of mesh points in θ) must be treated carefully by either enforcing boundary conditions or using a lower-order forward or backward finite difference approximation at the boundaries.

Table A.1: Butcher tableau for RK4(3)5M.

α	β				c	$\hat{c}$
0	0				$\frac{79}{490}$	$\frac{229}{1470}$
$\frac{2}{7}$	$\frac{2}{7}$				0	0
$\frac{7}{15}$	$\frac{77}{900}$	$\frac{343}{900}$			$\frac{2175}{3626}$	$\frac{1125}{1813}$
$\frac{35}{38}$	$\frac{805}{1444}$	$-\frac{77175}{54872}$	$\frac{97125}{54872}$		$\frac{2166}{9065}$	$\frac{13718}{81585}$
1	$\frac{79}{490}$	0	$\frac{2175}{3626}$	$\frac{2166}{9065}$		$\frac{1}{18}$

The fixed-frame evolution equation, Eq. (3.48), is solved numerically in same manner as the moving-frame evolution equation, Eq. (3.49). The different functional form of the fixed-frame evolution equation compared to that of the moving-frame evolution equation does not impact implementation of the numerical scheme. Let the time coordinate ϕ be uniformly discretized with the constant step $\Delta\phi$ such that $\phi_n = n\Delta\phi$. The discretized form of the fixed-frame evolution equation is written here as

$$\frac{\partial \Psi_n}{\partial X} = -\left(\frac{\gamma}{1 + N_2\Psi_n + N_3\Psi_n^2}\right)\frac{\Delta\phi^{-3/4}}{\Gamma(5/4)}\sum_{j=0}^{n} d_j\Psi_j \tag{A.11}$$

The RK3(4) method is used for numerical integration of $\Psi_n(X)$ with respect to the X coordinate in Eq. (A.11).

The viscoelastic evolution equation, Eq. (3.72), is not as simple to solve numerically because of the convolution integral that is used to incorporate the interface viscosity. The difficulty is associated with the term

$$\int_0^{\phi} \frac{\partial^{3/4}\Psi(\phi')}{\partial\phi'^{\,3/4}}\frac{e^{-(\phi-\phi')/\Omega}}{\sqrt{\phi-\phi'}}d\phi' \tag{A.12}$$

In Eq. (A.12) the lower integration limit is 0 instead of $-\infty$, as it is in Eq. (3.72), because for the present analysis it is assumed that $\Psi(X,\phi) = 0$ for $\phi \leq 0$.

To approximate the expression in Eq. (A.12) numerically at $\phi = \phi_n$, the integral is discretized in the same way as Eq. (A.2):

$$\int_0^{\phi_n} \frac{\partial^{3/4}\Psi(\phi')}{\partial\phi'^{\,3/4}}\frac{e^{-(\phi_n-\phi')/\Omega}}{\sqrt{\phi_n-\phi'}}d\phi' = \sum_{j=0}^{n-1}\int_{\phi_j}^{\phi_{j+1}} \frac{\partial^{3/4}\Psi(\phi')}{\partial\phi'^{\,3/4}}\frac{e^{-(\phi_n-\phi')/\Omega}}{\sqrt{\phi_n-\phi'}}d\phi' \tag{A.13}$$

For sufficiently small $\Delta\phi$ the fractional derivative $\partial^{3/4}\Psi/\partial\phi^{3/4}$ can be approximated as a constant over the limits of the integral in Eq. (A.13) and thus removed from the integrand:

$$\int_0^{\phi_n} \frac{\partial^{3/4}\Psi(\phi')}{\partial\phi'^{\,3/4}} \frac{e^{-(\phi_n-\phi')/\Omega}}{\sqrt{\phi_n-\phi'}} d\phi' \simeq \sum_{j=0}^{n-1} \left.\frac{\partial^{3/4}\Psi(\phi')}{\partial\phi'^{\,3/4}}\right|_{\phi'=\phi_j} \int_{\phi_j}^{\phi_{j+1}} \frac{e^{-(\phi_n-\phi')/\Omega}}{\sqrt{\phi_n-\phi'}} d\phi' \tag{A.14}$$

The fractional derivative is assumed to be approximately constant in the neighborhood of $\phi' = \phi_j$, the lower integration limit, as opposed to its behavior in between the lower and upper limits at $\phi' \simeq \phi_{j+1/2}$. This is a lower-order approximation than was made in Eq. (A.3), but it allows the fractional derivative approximation, Eq. (A.8), to be easily incorporated in Eq. (A.14). The integral in Eq. (A.14) possesses the analytical solution

$$\int_{\phi_j}^{\phi_{j+1}} \frac{e^{-(\phi_n-\phi')/\Omega}}{\sqrt{\phi_n-\phi'}} d\phi' = \sqrt{\pi\Omega}\left[\operatorname{erf}\left(\sqrt{\frac{\phi_n-\phi_j}{\Omega}}\right) - \operatorname{erf}\left(\sqrt{\frac{\phi_n-\phi_{j+1}}{\Omega}}\right)\right] \tag{A.15}$$

where $\operatorname{erf}(x)$ is the error function. Substitution of Eq. (A.8) for the fractional derivative and Eq. (A.15) for the integral in Eq. (A.14) yields

$$\begin{aligned}\int_0^{\phi_n} \frac{\partial^{3/4}\Psi(\phi')}{\partial\phi'^{\,3/4}} \frac{e^{-(\phi_n-\phi')/\Omega}}{\sqrt{\phi_n-\phi'}} d\phi' \simeq & \frac{\sqrt{\pi\Omega}\Delta\phi^{-3/4}}{\Gamma(5/4)} \sum_{j=0}^{n-1} \left(\sum_{i=0}^{j} d_i\Psi_i\right) \\ & \times \left[\operatorname{erf}\left(\sqrt{\frac{\phi_n-\phi_j}{\Omega}}\right) - \operatorname{erf}\left(\sqrt{\frac{\phi_n-\phi_{j+1}}{\Omega}}\right)\right]\end{aligned} \tag{A.16}$$

When the wave variable Ψ is represented as a column vector containing all $\Psi_n(X)$, the double summation in Eq. (A.16) can be performed with matrix multiplication.

Equation (A.16) is used to write the viscoelastic evolution equation in the discretized form

$$\frac{\partial \Psi_n}{\partial X} = -\frac{\gamma(\Delta\phi)^{-3/4}/\Gamma(5/4)}{1+N_2\Psi_n+N_3\Psi_n^2} \times \sum_{j=0}^{n-1}\left(\sum_{i=0}^{j} d_i\Psi_i\right)\left[\operatorname{erf}\left(\sqrt{\frac{\phi_n-\phi_j}{\Omega}}\right)-\operatorname{erf}\left(\sqrt{\frac{\phi_n-\phi_{j+1}}{\Omega}}\right)\right] \tag{A.17}$$

Equation (A.17) is numerically integrated forward in X using the RK3(4) method.

To compare the numerical formulations of the moving-frame, fixed-frame, and viscoelastic evolution equations, Eqs. (A.10), (A.11), and (A.17), respectively, the initial condition

$$\Psi(0,\phi) = \Psi_0(\phi) = \operatorname{erf}\left[(\phi/\pi)^4\right]\sin\phi \tag{A.18}$$

is used (note that in the case of the moving-frame evolution equation, at $X = 0$ the relation $\theta = \phi$ holds). The error function in Eq. (A.18) smoothes the initial condition near $\phi = 0$ such that $\Psi_0(0) = 0$ and $\partial\Psi/\partial X(0,\phi) = 0$.

Figure A.1 shows propagation starting with the initial condition, Eq. (A.18) (dashed curve) from $X = 0$ out to $X = 2$ according to the moving-frame, fixed-frame, and viscoelastic evolution equations for $N_2 = -0.5$, $N_3 = 1.0$, and $\Omega = 0.1$. The chosen values for N_2 and N_3 represent moderate nonlinearity. The value of $\Omega = 0.1$ is chosen to be large enough to illustrate the influence of the interface viscosity taken into account by Eq. (A.17), but small enough such that the assumption of constant Ω is valid for nonlinear propagation (see

Sec. 3.4 for further discussion on valid choices of Ω in the viscoelastic evolution equation). In Fig. A.1, the numerical solution of the moving-frame evolution equation is plotted versus ϕ by employing the relation $\theta + X = \phi$. Figure A.1 shows that the solutions of the fixed-frame (red curve) and viscoelastic (blue curve) evolution equations are in very good agreement. The positive sections of the waveform predicted by the moving-frame evolution equation (green curve) are in good agreement with those of the other solid curves, but there are discrepancies in the negative portion. This is similar to what is observed in the model comparison in Fig. 3.4.

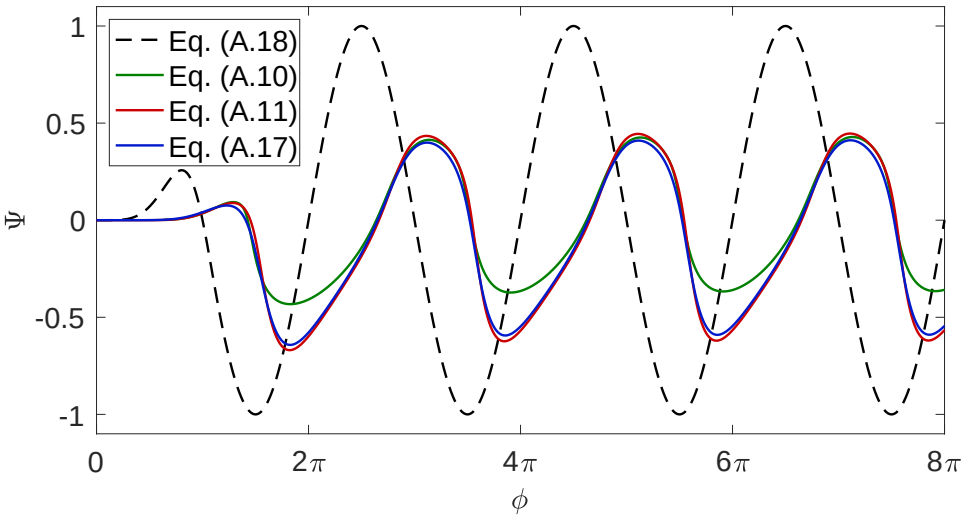

Figure A.1: Solutions of the moving-frame, fixed-frame, and viscoelastic evolution equations, Eqs. (A.10), (A.11), and (A.17), respectively, at $X = 2$. The initial condition at $X = 0$ is described by Eq. (A.18) and the constants $N_2 = -0.5$, $N_3 = 1.0$, and $\Omega = 0.1$ are used.

Table A.2 shows statistics for the RKF3(4) algorithm for the moving-

frame, fixed-frame, and viscoelastic evolution equations. In Table A.2 a step refers to calculation of the wave variable at the next step in X [i.e., $\Psi_n(X + \Delta X)$], a rejection refers to a step that is rejected because it does not meet the tolerance specifications, and function evaluations track how many times the evolution equation is evaluated. In the present work, the absolute tolerance for the RKF3(4) algorithm is 10^{-6}. There are 1000 time steps used with a maximum time of $\phi = 8\pi$. In Table A.2 the viscoelastic evolution equation required significantly fewer spatial steps and function evaluations to converge to a solution at $X = 2$. The viscoelastic evolution equation also did not reject any steps during the calculation, indicating that the algorithm is very stable and converges to a solution quickly. The increased numerical stability of the viscoelastic evolution equation is one added benefit of the included interface viscosity.

Table A.2: Statistics for RKF3(4) for the moving-frame, fixed-frame, and viscoelastic evolution equations, Eqs. (A.10), (A.11), and (A.17), respectively, after calculation of the propagation of the initial condition, Eq. (A.18), from $X = 0$ out to $X = 2$. The values $N_2 = -0.5$, $N_3 = 1.0$, and $\Omega = 0.1$ are used in the evolution equations. An absolute tolerance of 10^{-6} is used, along with 1000 time steps out to $\phi = 8\pi$.

	Total Steps	Rejected Steps	Function Evaluations
Eq. (A.10)	97	17	389
Eq. (A.11)	76	17	305
Eq. (A.17)	50	0	201

The numerical effects of the interface viscosity in the viscoelastic evo-

lution equation can be further investigated using the initial condition

$$\Psi(0,\phi) = \Psi_0(\phi) = \frac{1}{2} + \frac{1}{\pi}\arctan\left[50(\phi - \pi)\right] \tag{A.19}$$

with increased nonlinearity ($N_2 = -2$ and $N_3 = 10$). Figure A.2 shows solutions for the propagation of the initial condition, Eq. (A.19), from $X = 0$ out to $X = 3$ given by the fixed-frame (red curve) and viscoelastic (blue curve) evolution equations, Eqs. (A.11) and (A.17). The moving-frame evolution equation, Eq. (A.10), is not considered in Fig. A.2 because the moving-frame evolution equation fails at sufficiently high nonlinearity (see Sec. 3.3.6 or Chap. 4 for discussion of how the moving-frame evolution equation potentially admits unphysical multivalued solutions). In Fig. A.2(a) the value $\Omega = 0.1$ was chosen for the viscoelastic evolution equation while in Fig. A.2(b) the coefficient is considerably smaller, $\Omega = 0.01$. The predicted waveforms are nearly indistinguishable in Fig. A.2(b) while in (a) the viscoelastic evolution equation predicts a much smoother waveform.

Table A.3 shows the shows statistics for the RKF3(4) algorithm for the fixed-frame evolution equation and the viscoelastic evolution equation with $\Omega = 0.1$ and $\Omega = 0.01$, after calculation of the solution for the propagation of the initial condition at $X = 0$, Eq. (A.19), out to $X = 3$. Once again, an absolute tolerance of 10^{-6} is chosen and there are 1000 mesh points in time with a maximum time of $\phi = 2\pi$. For $\Omega = 0.1$ [Fig. A.2(a)] the viscoelastic evolution equation requires significantly less function evaluations than the fixed-frame evolution equation (685 versus 3869 evaluations, respectively). When there

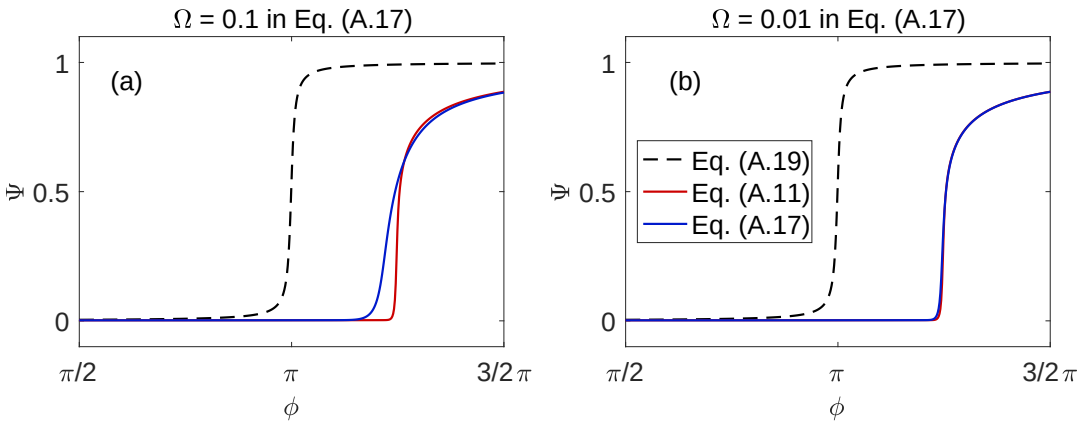

Figure A.2: Solutions of the moving-frame, fixed-frame, and viscoelastic evolution equations, Eqs. (A.10), (A.11), and (A.17), respectively, at $X = 3$. The initial condition at $X = 0$ is described by Eq. (A.19) and the constants $N_2 = -2$, $N_3 = 10$, $\Omega = 0.1$ in (a) and $\Omega = 0.1$ in (b) are used.

is less interface viscosity [$\Omega = 0.01$, Fig. A.2(b)] the viscoelastic evolution equation still uses less function evaluations than the fixed-frame evolution equation (2549 versus 3869 evaluations, respectively), but the predicted waveforms produced by each evolution equation are nearly the same. So even for small amounts of interface viscosity such that the fixed-frame and viscoelastic evolution equations produce nearly the same results, the viscoelastic evolution equation still exhibits better numerical stability and converges in fewer function evaluations. This does, however, come at a cost: the function evaluations required for the viscoelastic evolution are more expensive computationally (in terms of computation time) in comparison with those required for the fixed-frame evolution equation because in Eq. (A.17) there are two discrete summations that must be evaluated, as opposed to only one in the discretized

fixed-frame evolution equation, Eq. (A.11).

Table A.3: Statistics for RKF3(4) for the fixed-frame, and viscoelastic (with $\Omega = 0.1$ and $\Omega = 0.01$) evolution equations, (A.11), and (A.17), respectively, after calculation of the propagation of the initial condition, Eq. (A.19), from $X = 0$ out to $X = 3$. The nonlinearity is more significant than that of Table A.3 with $N_2 = -2$ and $N_3 = 10$. An absolute tolerance of 10^{-6} is used, along with 1000 time steps out to $\phi = 2\pi$.

	Total Steps	Rejected Steps	Function Evaluations
Eq. (A.11)	967	318	3869
Eq. (A.17) with $\Omega = 0.1$	171	18	685
Eq. (A.17) with $\Omega = 0.01$	637	180	2549

A.3 Numerical schemes for solving the KSSN equation

The method of lines scheme used in Sec. A.2 to numerically solve the fixed-frame, moving-frame, and viscoelastic evolution equations is not well suited for the KSSN equation, Eq. (3.47). Being a compound fractional wave equation, the KSSN equation is typically formulated as a boundary value problem in which the source is at the boundary $X = 0$.[20] Runge-Kutta methods cannot easily be applied to boundary value problems. One algorithm that uses Runge-Kutta methods for boundary value problems is the shooting method,[67] which is especially inefficient for large systems of coupled differential equations.

Instead, a finite difference[68] scheme is used to numerically integrate the KSSN equation. Simple finite difference methods are often easy to implement, but hard to optimize. While the RK3(4) method using in Sec. A.2 has adap-

tive time stepping, most finite differencing methods use uniform spacing that does not account for potentially unstable regions of the solution that exhibit large gradients. Nonuniform finite difference schemes have certainly been used before,[69] but these schemes are not as easily implemented and are not used in the present work.

Since the order of the fractional time derivative in the present work falls in the range $1 < \eta < 2$ the discretized convolution integral for the fractional derivative, derived from Eq. (A.1), is

$$\left.\frac{d^{\eta} f(t)}{dt^{\eta}}\right|_{t=t_n} = \frac{1}{\Gamma(2-\eta)} \sum_{j=0}^{n-1} \int_{t_j}^{t_{j+1}} \frac{d^2 f(t')/dt'^2}{(t_n - t')^{\eta-1}} dt' \tag{A.20}$$

A central finite difference stencil is used to approximate the derivative at the upper limit of the integrand in Eq. (A.20):

$$\left.\frac{d^2 f(t')}{dt'^2}\right|_{t'=t_{j+1}} \simeq \frac{f(t_{j+2}) - 2f(t_{j+1}) + f(t_j)}{(\Delta t)^2} \tag{A.21}$$

The stencil in Eq. (A.21), along with the steps in Sec. A.1, is used to derive the numerical representation of the fractional derivative for $1 < \eta < 2$

$$\frac{d^{\eta} f(t)}{dt^{\eta}} = \frac{(\Delta t)^{-\eta}}{\Gamma(3-\eta)} \sum_{j=0}^{n+1} d_{n,j} f(t_j) \quad \text{for } 1 < \eta < 2 \tag{A.22}$$

where $d_{n,j}$ in Eq. (A.22) is now defined by

$$d_{n,j} = \begin{cases} n^{2-\eta} - (n-1)^{2-\nu} & j = 0 \\ -2n^{2-\nu} + 3(n-1)^{2-\nu} - (n-2)^{2-\nu} & j = 1 \\ (n-j+2)^{2-\nu} - 3(n-j+1)^{2-\nu} \\ \quad + 3(n-j)^{2-\nu} - (n-j-1)^{2-\nu} & 2 \le j \le n-1 \\ 2^{2-\nu} - 3 & j = n \\ 1 & j = n+1 \end{cases} \tag{A.23}$$

Let the ϕ and X coordinates of the KSSN equation be uniformly spaced according to $\Delta\phi$ and ΔX, respectively, such that $\phi_n = n\Delta\phi$ and $X_m = m\Delta X$. For the wave variable U, let $U_n^m = U(X_m, \phi_n)$. The finite difference representation of the KSSN equation at time step ϕ_n is

$$\frac{\gamma^2(\Delta t)^{-\eta}}{\Gamma(3-\eta)} \sum_{j=0}^{n+1} d_{n,j} U_j^m = \left[1 - 2N_2 \left(\frac{U_n^{m+1} - U_n^{m-1}}{\Delta X} \right) + 2N_3 \left(\frac{U_n^{m+1} - U_n^{m-1}}{\Delta X} \right)^2 \right] \times \left(\frac{U_n^{m+1} - 2U_n^m + U_n^{m-1}}{(\Delta X)^2} \right) \tag{A.24}$$

Finally, the last term corresponding to the upper limit $j = n+1$ in the summation on the left-hand side of Eq. (A.24) is written separately, and the remaining terms of the summation are moved to the right-hand side, which yields an explicit relation for the next step in time, $\phi = \phi_{n+1}$:

$$U_{n+1}^m = \frac{\Gamma(3-\eta)}{\gamma^2 \Delta t^{-\eta}} \left[1 - 2N_2 \left(\frac{U_n^{m+1} - U_n^{m-1}}{\Delta X} \right) + 2N_3 \left(\frac{U_n^{m+1} - U_n^{m-1}}{\Delta X} \right)^2 \right] \times \left(\frac{U_n^{m+1} - 2U_n^m + U_n^{m-1}}{\Delta X^2} \right) - \sum_{j=0}^{n} d_{n,j} U_j^m \tag{A.25}$$

Equation (A.25) is straightforward and easy to implement, but like many explicit finite difference formulations, it is not stable, especially for very nonlinear problems. On the other hand, a fully implicit finite difference algorithm for the KSSN equation is not easily obtained because the KSSN equation is nonlinear and contains the fractional time derivative. Instead, a hybrid explicit-implicit algorithm is used.

To derive the hybrid explicit-implicit finite difference method for the KSSN equation, begin by using the following finite difference approximation for the derivative in Eq. (A.20):

$$\left.\frac{d^2 f(t')}{dt'^2}\right|_{t'=t_j} \simeq \frac{f(t_{j+1}) - 2f(t_j) + f(t_{j-1})}{(\Delta t)^2} \tag{A.26}$$

Equation (A.26) now approximates the derivative at the lower limit ($t = t_j$) in Eq. (A.20) as opposed to the upper limit. The stencil in Eq. (A.26) will be used to derive a numerical approximation of the fractional time derivative at time $t = t_{n+1}$ rather than $t = t_n$ [i.e., the upper limit of the discrete summation in Eq. (A.20) is now $j = n$ instead of $j = n - 1$]. The new numerical approximation for the fractional time derivative is

$$\frac{d^\eta f(t)}{dt^\eta} = \frac{(\Delta t)^{-\eta}}{\Gamma(3-\eta)} \sum_{j=-1}^{n+1} d_{n+1,j+1} f(t_j) \quad \text{for } 1 < \eta < 2 \tag{A.27}$$

In Eq. (A.27), because the summation begins at $j = -1$, a pre-initial condition $f(t)$ at $t = t_{-1}$ (recall that $t_n = n\Delta t$) must be specified. Two initial conditions are needed to uniquely define the second-order derivative that appears in the definition of the fractional derivative with $1 < \eta < 2$, Eq. (A.20). In the

present work, $f(t_{-1})$ is either set to zero or is chosen such that $f(t_{-1}) = f(t_0)$. The new finite difference representation of the KSSN equation at $\phi = \phi_{n+1}$ is now written

$$\frac{\gamma^2(\Delta\phi)^{-\eta}}{\Gamma(3-\eta)} \sum_{j=-1}^{n+1} d_{n+1,j+1} U_j^m = \left[1 - 2N_2 \left(\frac{U_{n+1}^{m+1} - U_{n+1}^{m-1}}{\Delta X}\right) + 2N_3 \left(\frac{U_{n+1}^{m+1} - U_{n+1}^{m-1}}{\Delta X}\right)^2\right] \times \left(\frac{U_{n+1}^{m+1} - 2U_{n+1}^{m} + U_{n+1}^{m-1}}{(\Delta X)^2}\right) \tag{A.28}$$

It is observed that Eq. (A.28) is a fully implicit equation for the presently unknown variable U_{n+1}^m at each mesh point in X. It is convenient to rewrite Eq. (A.28) in matrix notation. Let the vector $\vec{U}_j$ containing the values of $U(X, \phi)$ at all mesh points in X at time $\phi = \phi_j$ be defined by

$$\vec{U}_j = \begin{bmatrix} U_j^1 \\ U_j^2 \\ \vdots \\ U_j^M \end{bmatrix} \tag{A.29}$$

where M is the number of mesh points in X. The vector $\vec{U}_j$ has length M, and $X = X_0$ and $X = X_{M+1}$ are the boundaries of the physical domain. Let $\mathbf{D_1}$ and $\mathbf{D_2}$ be matrices that carry out the central difference approximations for the first- and second-order derivatives, respectively, of $U(X, \phi)$ with respect to

X. These matrices are written here as

$$\mathbf{D_1} = \frac{1}{2\Delta X}\begin{bmatrix} 0 & 1 & 0 & 0 & \dots & \dots & 0 \\ -1 & 0 & 1 & 0 & & & 0 \\ \vdots & & & \ddots & & & \vdots \\ \vdots & & & & \ddots & & 0 \\ 0 & \dots & 0 & 0 & -1 & 0 & 1 \\ 0 & \dots & 0 & 0 & 0 & -1 & 0 \end{bmatrix} \tag{A.30}$$

$$\mathbf{D_2} = \frac{1}{(\Delta X)^2}\begin{bmatrix} -2 & 1 & 0 & 0 & \dots & \dots & 0 \\ 1 & -2 & 1 & 0 & & & 0 \\ \vdots & & & \ddots & & & \vdots \\ \vdots & & & & \ddots & & 0 \\ 0 & \dots & 0 & 0 & 1 & -2 & 1 \\ 0 & \dots & 0 & 0 & 0 & 1 & -2 \end{bmatrix} \tag{A.31}$$

The matrices $\mathbf{D_1}$ and $\mathbf{D_2}$ are size $M \times M$. For convenience we also define

$$A = \frac{\gamma^2(\Delta t)^{-\eta}}{\Gamma(3-\eta)} \tag{A.32}$$

The explicit finite difference scheme for the KSSN equation, Eq. (A.25), can now be written in vector notation as

$$\vec{U}^E_{n+1} = \frac{1}{A}\left[1 - 2N_2\mathbf{D_1}\vec{U}_n + 2N_3\left(\mathbf{D_1}\vec{U}_n\right)^2\right]\mathbf{D_2}\vec{U}_n - \sum_{j=0}^{n} d_{n,j}\vec{U}_j \tag{A.33}$$

where the superscript $n+1$ for the solution $\vec{U}^E_{n+1}$ indicates that the solution has been found using the explicit formula Eq. (A.33). Using Eqs. (A.29)–(A.32) and separating out the final term from the summation in Eq. (A.28) one obtains for the finite difference representation of the KSSN equation, Eq. (A.28),

$$A\left(\vec{U}_{n+1} + \sum_{j=-1}^{n} d_{n+1,j+1}\vec{U}_j\right) = \left[1 - 2N_2\mathbf{D_1}\vec{U}_{n+1} + 2N_3\left(\mathbf{D_1}\vec{U}_{n+1}\right)^2\right]\mathbf{D_2}\vec{U}_{n+1} \tag{A.34}$$

As with Eq. (A.28), Eq. (A.34) is an implicit representation of the KSSN equation at time step $\phi = \phi_{n+1}$.

Equation (A.34) is difficult to solve for $\vec{U}_{n+1}$ because of the nonlinear terms. To get around this problem the explicit solution for the KSSN equation, the left-hand side of Eq. (A.33), is substituted in for the nonlinear terms $\vec{U}_{n+1}$ within the brackets of Eq. (A.34). The vector containing the explicit numerical solutions found from Eq. (A.33) at time $\phi = \phi_{n+1}$ is labeled $\vec{U}^E_{n+1}$ as it is in Eq. (A.33). After some rearrangement, Eq. (A.34) is rewritten

$$\left\{ A - \left[1 - 2N_2 \mathbf{D_1} \vec{U}^E_{n+1} + 2N_3 \left(\mathbf{D_1} \vec{U}^E_{n+1} \right)^2 \right] \mathbf{D_2} \right\} \vec{U}_{n+1} = -A \sum_{j=0}^{n} d_{n+1,j} \vec{U}_j \tag{A.35}$$

Define the matrix $\mathbf{E}$ to be

$$\mathbf{E} = A - \left[1 - 2N_2 \mathbf{D_1} \vec{U}^E_{n+1} + 2N_3 \left(\mathbf{D_1} \vec{U}^E_{n+1} \right)^2 \right] \mathbf{D_2} \tag{A.36}$$

The matrix $\mathbf{E}$ has size $M \times M$ and is dependent on the explicit solutions $\vec{U}^E_{n+1}$ that are found using Eq. (A.33). Matrix $\mathbf{E}$ is not a function of $\vec{U}_{n+1}$, which will be solved for implicitly in Eq. (A.35). In summary, the matrix which contains the nonlinearity of the system, matrix $\mathbf{E}$, has now been reduced to a linear operator by using the explicit solution in Eq. (A.33). Therefore, $\mathbf{E}$ can be inverted like any non-singular square matrix. The solution, $\vec{U}_{n+1}$, can now be expressed explicitly by rewriting Eq. (A.35) as

$$\vec{U}_{n+1} = -A\mathbf{E}^{-1} \sum_{j=0}^{n} d_{n+1,j} \vec{U}_j \tag{A.37}$$

To move forward one time step, a function evaluation of the explicit and implicit formulation of the KSSN equation are necessary, for a total of two function evaluations.

The numerical scheme described in Sec. A.3 combines the stability of an implicit finite difference formulation with the simplicity and efficiency of an explicit finite difference formulation. This is accomplished by approximating the nonlinear terms in Eq. (A.34) with the numerical solution from the explicit formulation, Eq. (A.24). Thus, the nonlinear implicit formulation of the KSSN equation, Eq. (A.34), is reduced to a linear system of equations that can be solved by matrix inversion of $\mathbf{E}$. The hybrid implicit explicit method described in this section is similar to the Crank-Nicholson method[70] for partial differential equations insofar as both methods combine elements of fully explicit and fully implicit schemes. However, the two methods are not the same because the present method described in Sec. A.3 mixes explicit and implicit methods only to simplify the nonlinearity of the KSSN equation, whereas the Crank-Nicholson is based on the trapezoidal rule and thus is used to achieve higher-order accuracy.

In the present derivation, central difference approximations are used for derivatives, but forward and backward finite difference approximations can be used as well (the matrices $\mathbf{D_1}$ and $\mathbf{D_2}$ will be defined differently if a different finite difference stencil is used). Initial and boundary conditions also must be addressed for the discretized KSSN equation. The finite difference matrices $\mathbf{D_1}$ and $\mathbf{D_2}$ are constrained by homogeneous Dirichlet boundary conditions at

$X = 0$ and $X = X_{M+1}$ (i.e., $U_n^0 = 0$ and $U_n^{M+1} = 0$). If different boundary conditions are required, such as a source condition at $X = 0$, then $\mathbf{D_1}$ and $\mathbf{D_2}$ must be adjusted accordingly. For the initial and pre-initial conditions $\vec{U}_0$ and $\vec{U}_{-1}$, respectively, it is typically convenient to choose $\vec{U}_0$ and $\vec{U}_{-1}$ such that $\partial U/\partial\phi(X, \phi) = 0$ for $\phi \leq 0$ because fractional derivatives are history dependent. Any dynamical history in the physical system for $\phi \leq 0$ is left out of Eq. (A.1), and thus calculation of the fractional derivative will be inaccurate. In other words, it is convenient to choose $\phi = 0$ at the beginning of the dynamical event that is being modeled.

Figure A.3 shows the numerical solution of the KSSN equation, Eq. (A.37), and the fixed-frame evolution equation, Eq. (A.11), all with $N_2 = -0.5$ and $N_3 = 1.0$, at $X = 2$ with an initial condition described by Eq. (A.18). The KSSN equation is formulated with Neumann boundary conditions in order for the relation $\Psi = -\partial U/\partial X$ to hold (see discussion at the end of Sec. 3.3.3 for why Neumann boundary conditions are required for the relation $\Psi = -\partial U/\partial X$ to be true). The solution of the fixed-frame evolution equation (red curve) is the same as shown in Fig. A.1. For the discrete formulation of the KSSN equation the values $\Delta X = 0.02$ and $X_M = 20.02$ (resulting in 1000 mesh points in X) are chosen so that each evaluation of Eq. (A.37) is comparable to an evaluation of the discretized fixed-frame evolution equation (i.e., the number of mesh points in X for the KSSN equation is equal to the number of mesh points in ϕ for the fixed-frame evolution equation). One disadvantage of the finite difference method used to solve the KSSN equation is that

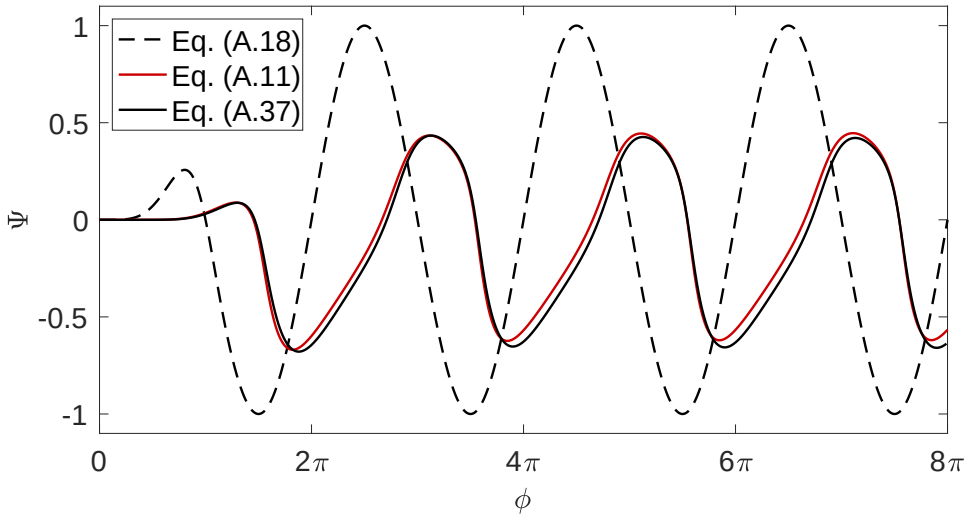

Figure A.3: Solutions of the fixed-frame evolution equation and the KSSN equations, Eqs. (A.11) and (A.37), respectively, at $X = 2$. The initial condition at $X = 0$ is described by Eq. (A.18) and the constants $N_2 = -0.5$ and $N_3 = 1.0$ are used.

adaptive time stepping and specification of tolerance are not available, unlike the method of lines that is used to solve the evolution equations. Because the tolerance cannot be specified for the KSSN equation, it is hard to compare function evaluations of the KSSN equation in a consistent way with function evaluations of the fixed-frame evolution equation for a given tolerance. To produce the black curve in Fig. A.3, 1004 function evaluations of Eq. (A.37) were necessary, which is significantly greater than that of any of the evolution equations shown in Table A.2.

Another shortcoming of the finite difference method used to solve the KSSN equation numerically is that for the signaling problem[25] (see Sec. 2.3.2

for an explanation of the signaling problem) the vector in Eq. (A.29) must be chosen to include values of U at much larger distances X than what is sought in order to prevent spurious unphysical reflections from the boundary at $X = X_M$. For example, in Fig. A.3 the propagated waveforms are compared at $X = 2$. The discretized fixed-frame evolution equation (red curve), Eq. (A.11), only had to be evaluated up to exactly $X = 2$, but the discretized KSSN equation, Eq. (A.37), had to be solved for $\vec{U}_n$ containing values of U out to $X = 20.02$ in order for the fractional time derivative to introduce sufficient attenuation for reflections from the boundary at $X = 20.02$ to be negligible.

In summary, the downsides of the finite difference scheme used to solve the KSSN equation, Eq. (A.37), including the lack of adaptive stepping, no way to rigorously control the tolerance, the need to include values of U at large distances, leading to significantly more function evaluations, and complexity of implementation, motivate the use of the moving-frame, fixed-frame, and viscoelastic evolutions equations, Eqs. (A.10), (A.11), and (A.17), respectively.

While only the KSSN equation without interface viscosity is addressed in this section, the KSSN equation with interface viscosity, Eq. (3.71), is solved in a very similar manner.

Appendix B

Application of Whitham's analysis to fractional waves

In Sec. 2.7 of his book *Linear and Nonlinear Waves*,[30] Whitham investigates whether solutions with discontinuities satisfy the weak formulation of a set of conservation equations associated with nonlinear evolution equations. If a partial differential equation admits discontinuous solutions, then shock formation (formation of a discontinuity) should be possible for sufficient nonlinearity. If discontinuous solutions are not permitted, then the propagation of true shock fronts will not be possible.

A loose form of Whitham's method will be used in this section. Begin with the general evolution equation

$$c_0 \frac{\partial \xi}{\partial x} + \frac{\partial \xi}{\partial t} = 0 \tag{B.1}$$

for propagation of a waveform described by $\xi(x,t)$ at a constant wave speed c_0. Now assume a discontinuous solution of Eq. (B.1) in the form

$$\xi(x,t) = \xi_{\text{sh}}(x) H(t - x/u_{\text{sh}}) + \xi_1(x,t) \tag{B.2}$$

where $H(x)$ is the Heaviside step function, $\xi_{\text{sh}}(x)$ describes the amplitude of the discontinuity and the tail that follows it, u_{sh} is the speed of the discontinuity, and $\xi_1(x,t)$ is a continuous function that is the "background" of the

propagating solution that is added to the continuous sections of the waveform behind and ahead of the shock. Figure B.1 shows an arbitrary waveform that is in the form of Eq. (B.2). The shock is located at $x = u_{\rm sh}t$ and is followed by a shock tail $\xi_{\rm sh}(x)$ that is added on top of the continuous waveform $\xi_1(x,t)$.

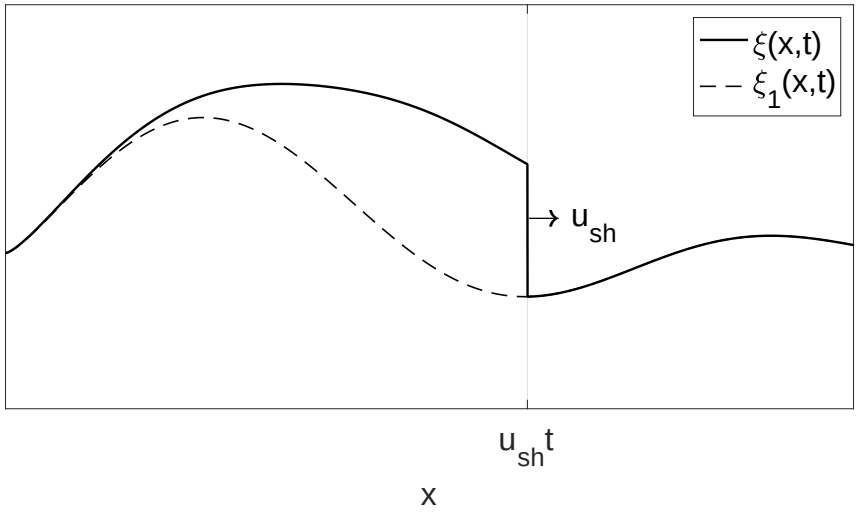

Figure B.1: Graphical depiction of Eq. (B.2) at a fixed time t. The discontinuity at $x = u_{\rm sh}t$ travels forward with speed $u_{\rm sh}$.

The x and t derivatives of Eq. (B.2) are

$$\frac{\partial \xi}{\partial x} = \frac{d\xi_{\rm sh}}{dx} H(t - x/u_{\rm sh}) - \frac{\xi_{\rm sh}}{u_{\rm sh}} \delta(t - x/u_{\rm sh}) + \frac{\partial \xi_1}{\partial x} \tag{B.3}$$

$$\frac{\partial \xi}{\partial t} = \xi_{\rm sh} \delta(t - x/u_{\rm sh}) + \frac{\partial \xi_1}{\partial t} \tag{B.4}$$

where δ is the Dirac delta function. Substitution of Eqs. (B.3) and (B.4) into the evolution equation, Eq. (B.1), yields

$$\left(1 - \frac{c_0}{u_{\rm sh}}\right) \xi_{\rm sh} \delta(t - x/u_{\rm sh}) + c_0 \frac{d\xi_{\rm sh}}{dx} H(t - x/u_{\rm sh}) + c_0 \frac{\partial \xi_1}{\partial x} + \frac{\partial \xi_1}{\partial t} = 0 \tag{B.5}$$

Equation (B.5) has a mathematical singularity due to the δ function. For a partial differential equation to admit discontinuous solutions in the form of Eq. (B.2), the singular terms must be eliminated, or else physical interpretation is impossible. The singularity in Eq. (B.5) can be eliminated if the speed of the discontinuity is $u_{\text{sh}} = c_0$. Under this condition, Eq. (B.2) is a valid solution of Eq. (B.1). It follows that shock fronts can exist for the simple evolution equation, Eq. (B.1), and will travel at the constant wave speed c_0. This is an expected result, as Eq. (B.1) is simply the linear evolution equation for a lossless forward traveling progressive wave.

However, the proposed solution in Eq. (B.2) will not be suitable for every partial differential equation. For example, consider the evolution equation for a forward traveling progressive wave with viscous losses characterized by the constant μ_k, which represents kinematic viscosity:

$$c_0 \frac{\partial \xi}{\partial x} + \frac{\partial \xi}{\partial t} = \mu_k \frac{\partial^2 \xi}{\partial x^2} \tag{B.6}$$

The second derivative of ξ with respect to x is

$$\frac{\partial^2 \xi}{\partial x^2} = \frac{d^2 \xi_{\text{sh}}}{dx^2} H(t - x/u_{\text{sh}}) - \frac{2}{u_{\text{sh}}} \frac{d\xi_{\text{sh}}}{dx} \delta(t - x/u_{\text{sh}}) + \frac{\xi_{\text{sh}}}{u_{\text{sh}}^2} \delta'(t - x/u_{\text{sh}}) + \frac{\partial^2 \xi_1}{\partial x^2} \tag{B.7}$$

where δ' is the derivative of the δ function with respect to its argument, which is still singular at $t = x/u_{\text{sh}}$.

One way to define $\delta'(t)$ is the relation[71]

$$t\delta'(t) = -\delta(t) \tag{B.8}$$

But before proceeding, it is necessary to discuss what the function $\delta'(t)$ means within the context of the present work. Loosely speaking, $\delta'(t)$ is *more* singular than $\delta(t)$. To see this, divide $\delta'(t)$ by $\delta(t)$ using Eq. (B.8) (setting aside the fact that it can be problematic to divide by a delta function):

$$\frac{\delta'(t)}{\delta(t)} = -\frac{1}{t} = -\infty \quad \text{at } t = 0 \tag{B.9}$$

An interpretation of Eq. (B.9) is that $\delta'(t)$ is infinitely larger in magnitude than $\delta(t)$ at $t = 0$.

The relation between $\delta'(t)$ and $\delta(t)$ is further contextualized in the study of singularity functions.[72] Singularity functions are typically used to study deflection in beams, but in the present work the formalism of singularity functions is used to compare functions with different degrees of singularity (typically called singularity brackets). Singularity functions, which will be denoted as $\sigma_n(t)$, specifically those centered at $t = 0$, are denoted using brackets as follows:

$$\sigma_n(t) = \langle t \rangle^n \tag{B.10}$$

where n is traditionally an integer. A few examples of singularity functions are listed in Table B.1. In one sense, higher values of n indicate greater smoothness for singularity functions at the point where they are centered. For example, $n = 0$ in Table B.1 corresponds to the Heaviside step function, which has a discontinuity at $x = 0$, and $n = 1$ corresponds to a ramp function that has a discontinuity in slope at $t = 0$ but is still functionally continuous. All singularity functions with $n < 0$ are singular at $t = 0$. Lower values of n

indicate that a function is more singular. For example, $\delta'(t)$ ($n = -2$) is more singular than $\delta(t)$ ($n = -1$), which is consistent with Eq. (B.9).

Table B.1: Examples of singularity functions for $-2 \leq n \leq 2$.

n	$\sigma_n(t) = \langle t \rangle^n$
-2	$\delta'(t)$
-1	$\delta(t)$
0	$H(t)$
1	$tH(t)$
2	$t^2H(t)$

The analysis now returns to Eq. (B.6). Substitution of Eqs. (B.3), (B.4), and (B.7) into the evolution equation, Eq. (B.6), yields

$$-\mu_k \frac{\xi_{\text{sh}}}{u_{\text{sh}}^2}\delta'(t - x/u_{\text{sh}}) + \left(\xi_{\text{sh}} - \xi_{\text{sh}}\frac{c_0}{u_{\text{sh}}} + \mu_k \frac{2}{u_{\text{sh}}}\frac{d\xi_{\text{sh}}}{dx}\right)\delta(t - x/u_{\text{sh}}) + \left(c_0\frac{d\xi_{\text{sh}}}{dx} - \mu_k\frac{d^2\xi_{\text{sh}}}{dx^2}\right)H(t - x/u_{\text{sh}}) + c_0\frac{\partial\xi_1}{\partial x} + \frac{\partial\xi_1}{\partial t} - \mu_k\frac{\partial^2\xi_1}{\partial x^2} = 0 \tag{B.11}$$

Assuming that μ_k is nonzero, the most singular term, which is δ', in Eq. (B.11) can only be eliminated if $\xi_{\text{sh}} = 0$. The singularity associated with δ' cannot be balanced by the terms multiplying δ because δ is less singular than δ'. No finite choice of the coefficients multiplying δ can balance the singularity associated with δ'. However, if $\xi_{\text{sh}} = 0$ is chosen, this implies that there is no discontinuity at all, because from Eq. (B.2), $\xi = \xi_1$, where ξ_1 is a continuous function. Therefore stable discontinuous solutions in the form of Eq. (B.2) cannot exist for the evolution equation with viscosity, Eq. (B.6).

Now apply this analysis to a fractional partial differential equation for progressive wave motion exhibiting power-law attenuation proportional to ω^ν, written in the form

$$c_0 \frac{\partial \xi}{\partial x} + \frac{\partial \xi}{\partial t} + a_\nu \frac{\partial^\nu \xi}{\partial t^\nu} = 0 \tag{B.12}$$

where a_ν is a constant with dimensions of $\mathrm{T}^{\nu-1}$ that characterizes the magnitude of the attenuation. A solution in the form of Eq. (B.2) will once again be assumed for Eq. (B.12). The Caputo fractional derivative definition, Eq. (2.2), with the lower limit of integration equal to zero and $0 < \nu < 1$, is used to calculate the fractional derivative of $H(t)$:

$$\begin{aligned} \frac{\partial^\nu H(t)}{\partial t^\nu} &= \frac{1}{\Gamma(1-\nu)} \int_0^t \frac{dH(t')/dt'}{(t-t')^\nu} dt' \\ &= \frac{1}{\Gamma(1-\nu)} \int_0^t \frac{\delta(t')}{(t-t')^\nu} dt' \\ &= \frac{H(t)}{t^\nu \Gamma(1-\nu)} \end{aligned} \tag{B.13}$$

Although it is assumed that $0 < \nu < 1$ in Eq. (B.13), the result in Eq. (B.13) is true more generally for $\nu > 0$. For example, consider the fractional derivative of $H(t)$ where $1 < \nu < 2$:

$$\begin{aligned} \frac{\partial^\nu H(t)}{\partial t^\nu} &= \frac{1}{\Gamma(2-\nu)} \int_0^t \frac{d^2 H(t')/dt'^2}{(t-t')^{\nu-1}} dt' \\ &= \frac{1}{\Gamma(2-\nu)} \int_0^t \frac{\delta'(t')}{(t-t')^{\nu-1}} dt' \\ &= \frac{H(t)(1-\nu)}{t^\nu \Gamma(2-\nu)} \\ &= \frac{H(t)}{t^\nu \Gamma(1-\nu)} \end{aligned} \tag{B.14}$$

There is a connection between the fractional derivative of $H(t)$, Eq. (B.14), and $\delta(t)$, the first order derivative of $H(t)$. Gel'fand and Shilov[71] analyze δ as a generalized function and prove the following relation:

$$\delta(t) = \frac{H(t)}{t\Gamma(0)} \tag{B.15}$$

Gel'fand and Shilov[71] also define the integer-order derivatives of $\delta(t)$ [and thus the integer-order derivatives of $H(t)$] as

$$\delta^{m-1}(t) = \frac{H(t)}{t^m\Gamma(1-m)} \tag{B.16}$$

where m is an integer corresponding to the mth derivative of $H(t)$. The definition of the mth integer order of $H(t)$, Eq. (B.16), is consistent with the definition of the fractional derivative of non-integer order ν, Eq. (B.13).

Fractional derivatives of $H(t)$ can also be interpreted in the context of singularity functions. While the first derivative of $H(x)$ corresponds to $n = -1$ in Table B.1, the fractional derivative of $H(x)$ corresponds to $n = -\nu$. As with $\delta(t)$, the fractional derivatives of $H(t)$ are singular at $t = 0$. The higher the fractional order ν is, the more singular the fractional derivative will be.

Based on the result in Eq. (B.13), the singular terms in the evolution equation, Eq. (B.12), may be written explicitly here as

$$\frac{a_\nu H(t - x/u_{\text{sh}})}{(t - x/u_{\text{sh}})^\nu \Gamma(1-\nu)}\xi_{\text{sh}} + \left(1 - \frac{c_0}{u_{\text{sh}}}\right)\xi_{\text{sh}}\delta(t - x/u_{\text{sh}}) + \text{non-singular terms} = 0 \tag{B.17}$$

The left-hand side of Eq. (B.17) is singular at $t = x/u_{\text{sh}}$. The $\sigma_1(t)$ singularities associated with the integer-order derivatives $\partial\xi/\partial x$ and $\partial\xi/\partial t$, and therefore

$\delta(t - x/u_{\text{sh}})$, can be balanced by setting $u_{\text{sh}} = c_0$. However, the singularity associated with the fractional derivative $\partial^\nu \xi / \partial t^\nu$ cannot be eliminated unless the shock amplitude is zero (i.e., $\xi_{\text{sh}} = 0$), which implies that no discontinuity exists in the proposed solution Eq. (B.2). Therefore, discontinuous solutions in the form of Eq. (B.2) are not permitted for partial differential equations with one fractional derivative. This result also holds for the fractional evolution equation

$$c_0 \frac{\partial \xi}{\partial x} + a_\nu \frac{\partial^\nu \xi}{\partial t^\nu} = 0 \tag{B.18}$$

because, once again, with the discontinuous solution, Eq. (B.2), substituted into Eq. (B.18), the singularity associated with the fractional derivative cannot be eliminated unless $\xi_{\text{sh}} = 0$.

While the discontinuous solution, Eq. (B.2), is not permitted for Eq. (B.12) according to this analysis, a separate question is whether vertical tangent formation is possible for an initially continuous waveform without a vertical tangent, which is the primary focus of Chap. 4. While the equations in this appendix are only linear, insight is gained by examining the singular terms that occur when the proposed solution, Eq. (B.2), is substituted into Eq. (B.12). The order of these singularities can be expressed concisely in the notation of singularity functions, where the singularities associated with the discrete derivatives have $n = -1$ and the singularity associated with the fractional derivative is $n = -\nu$.

For $0 < \nu < 1$ in Eq. (B.17), $\sigma_1(t) = \delta(t - x/u_{\text{sh}})$ is more singular than the σ_ν singularity associated with the fractional derivative. For the evolution

equation, Eq. (B.12), the attenuation comes exclusively from the fractional derivative. However, because the σ_ν singularity associated with the fractional derivative is negligibly small compared with the σ_1 singularity associated with δ near regions in the waveform with very large gradients (i.e., nearly discontinuous shock fronts), the attenuation in the system is not necessarily sufficient to prevent vertical tangent formation for a nonlinear form of Eq. (B.12) (i.e., for an amplitude-dependent sound speed instead of the constant c_0). For example, the moving-frame evolution equation, Eq. (4.4), which has a linear form similar to Eq. (B.12), permits vertical tangent formation for sufficiently large nonlinearity.[51] Once a vertical tangent forms for the moving-frame evolution equation, calculation cannot proceed because of the singularity associated with the fractional derivative. There are no known published implicit multivalued solutions for a fractional partial differential equation in the form of Eq. (B.12). Calculation past vertical tangent formation is nonsensical even using the intrinsic coordinates of Hammerton and Crighton[56] (see Sec. 4.3 for an explanation of intrinsic coordinates) because the loss term becomes complex [see Eqs. (42) and (44) for $\psi > \pi/2$ in Cormack and Hamilton[53]].

However, if $1 < \nu < 2$ in Eq. (B.12) with the proposed solution in Eq. (B.2), then the most singular term is the σ_ν term that is associated with the fractional derivative. Now the most significant term in Eq. (B.12) near regions with very steep gradients is the fractional derivative, which is responsible for the attenuation in the system. Therefore vertical tangent formation is always prevented for a nonlinear form of Eq. (B.12). This is consistent with the

analyses of Cormack and Hamilton[53] and Kashcheeva et al.[73] for a nonlinear acoustic wave with power-law attenuation proportional to ω^ν for which $1 < \nu < 2$.

In summary, Whitham's analysis[30] was used to consider the possibility of discontinuous solutions for fractional evolution equations. It was found that discontinuous solutions are not possible for the fractional evolution equations, Eqs. (B.12) and (B.18). However, by examining the singularities that arise at waveform discontinuities in Eq. (B.12), one finds that this analysis still implies the possibility of vertical tangent formation for $0 < \nu < 1$ in a nonlinear form of Eq. (B.12). It should be reiterated that just because vertical tangent formation is possible for $0 < \nu < 1$, this does not mean that a discontinuous solution in the form of Eq. (B.2) is allowed. As Whitham notes in his book,[30] δ is used in a "slightly dubious way" for this study. While the results of this section cannot be considered rigorous, Whitham's analysis is, in his words, very useful as a "preliminary tool."

Bibliography

[1] D. Fox, "The brain, reimagined," Sci. Am. **318**, 60–67 (April 2018).

[2] A. L. Hodgkin and A. F. Huxley, "A quantitative description of membrane current and its application to conduction and excitation in nerve," J. Physiol. **117**, 500–544 (1952).

[3] S. Shrivastava, "Action potentials are all in one: The false dichotomy of electrical vs mechanical." Medium, September 2018.

[4] T. Heimburg and A. D. Jackson, "On soliton propagation in biomembranes and nerves," Proc. Natl. Acad. Sci. U.S.A. **102**, 9790–9795 (2005).

[5] K. Kaufmann, "Book 4: Action potentials and electromechanical coupling in the macroscopic chiral phospholipid bilayer." Unpublished. Caruara, Brazil, 1989.

[6] I. Tasaki, "A macromolecular approach to excitation phenomena: Mechanical and thermal changes in nerve during excitation," Physiol. Chem. Phys. Med. NMR **20**, 251–268 (1988).

[7] I. Tasaki, K. Kusano, and P. Byrne, "Rapid mechanical and thermal changes in the garfish olfactory nerve associated with a propagated impulse," Biophys. J. **55**, 1033–1040 (1989).

[8] I. Tasaki, "Rapid structural changes in nerve fibers and cells associated with their excitation processes," Jpn. J. Physiol. **49**, 125–138 (1999).

[9] G. Kim, P. Kosterin, A. Obaid, and B. Salzberg, "A mechanical spike accompanies the action potential in mammalian nerve terminals," Biophys. J. **92**, 3122–3129 (2007).

[10] A. El Hady and B. B. Machta, "Mechanical surface waves accompany action potential propagation," Nat. Commun. **6**, 6697 (2015).

[11] Y. Yang, X.-W. Liu, H. Wang, H. Yu, Y. Guan, S. Wang, and N. Tao, "Imaging action potential in single mammalian neurons by tracking the accompanying sub-nanometer mechanical motion," ACS Nano **12**, 4186–4193 (2018). PMID: 29570267.

[12] J. Griesbauer, A. Wixforth, and M. F. Schneider, "Wave propagation in lipid monolayers," Biophys. J. **97**, 2710–2716 (2009).

[13] J. Griesbauer, S. Bössinger, A. Wixforth, and M. F. Schneider, "Propagation of 2D pressure pulses in lipid monolayers and its possible implications for biology," Phys. Rev. Lett. **108**, 198103 (May 2012).

[14] S. Shrivastava and M. F. Schneider, "Evidence for two-dimensional solitary sound waves in a lipid controlled interface and its implications for biological signalling," J. R. Soc. Interface **11**, 20140098 (2014).

[15] S. Shrivastava, K. H. Kang, and M. F. Schneider, "Solitary shock waves and adiabatic phase transition in lipid interfaces and nerves," Phys. Rev. E **91**, 012715 (2015).

[16] S. Shrivastava, K. H. Kang, and M. F. Schneider, "Collision and annihilation of nonlinear sound waves and action potentials in interfaces," J. R. Soc. Interface **15**, 20170803 (2018).

[17] M. Mussel and M. F. Schneider, "Similarities between action potentials and acoustic pulses in a van der Waals fluid," Scientific Reports **9**, 2467 (2019).

[18] K. Lucas, "The 'all or none' contraction of the amphibian skeletal muscle fibre," J. Physiol. **38**, 113–133 (1909).

[19] J. Engelbrecht, T. Peets, and K. Tamm, "Electromechanical coupling of waves in nerve fibres," Biomech. Model. Mechanobiol. **17**, 1771–1783 (December 2018).

[20] J. Kappler, S. Shrivastava, M. F. Schneider, and R. R. Netz, "Nonlinear fractional waves at elastic interfaces," Phys. Rev. Fluids **2**, 114804 (November 2017).

[21] J. Lucassen, "Longitudinal capillary waves. Part 1.–Theory," Trans. Faraday Soc. **64**, 2221–2229 (1968).

[22] J. Lucassen, "Longitudinal capillary waves. Part 2.–Experiments," Trans. Faraday Soc. **64**, 2230–2235 (1968).

[23] J. Kappler and R. R. Netz, "Multiple surface wave solutions on linear viscoelastic media," EPL (Europhysics Letters) **112**, 19002 (October 2015).

[24] J. Lucassen and M. van den Tempel, "Longitudinal waves on visco-elastic surfaces," J. Colloid Interface Sci. **41**, 491–498 (December 1972).

[25] F. Mainardi, *Fractional Calculus and Waves in Linear Viscoelasticity: An Introduction to Mathematical Models* (Imperial College Press, London, 2010).

[26] G. W. Leibniz, "Letter to l'Hôpital, September 30, 1695," pp. 301–302 in *Leibniz Mathematische Schriften* Vol. 1, (Verlag von A. Asher & Comp., 1849).

[27] S. Holm and S. P. Näsholm, "A causal and fractional all-frequency wave equation for lossy media," J. Acoust. Soc. Am. **130**, 2195–2202 (2011).

[28] S. Holm, *Waves with Power-Law Attenuation* (Springer Nature, Switzerland, 2018).

[29] F. Mainardi, "The time fractional diffusion-wave equation," Radiophys. Quantum Electron. **38**, 13–24 (1995).

[30] G. B. Whitham, *Linear and Nonlinear Waves* (John Wiley & Sons, Inc., New York, 1999).

[31] K. R. Waters, J. Mobley, and J. G. Miller, "Causality-imposed (Kramers-Kronig) relationships between attenuation and dispersion," IEEE Trans. Ultrason. Ferroelectr. Freq. Control **52**, 822–823 (May 2005).

[32] M. Caputo, "Linear models of dissipation whose Q is almost frequency independent–II," Geophys. J. Int. **13**, 529–539 (November 1967).

[33] E. C. de Oliveira and J. A. T. Machado, "A review of definitions for fractional derivatives and integral," Math Probl. Eng. **2014**, 238459 (June 2014).

[34] D. Pang, W. Jiang, and A. U. K. Niazi, "Fractional derivatives of the generalized Mittag-Leffler functions," Advances in Difference Equations **2018**, 415 (2018).

[35] H. Haubold, A. Mathai, and R. Saxena, "Mittag-Leffler functions and their applications," J. Appl. Math. **2011**, 298628 (2011).

[36] R. Gorenflo and F. Mainardi, "Fractional calculus: Integral and differential equations of fractional order." International Centre for Mechanical Sciences Lecture Notes, 2008.

[37] C. Li, Z. Zhao, and Y. Chen, "Numerical approximation of nonlinear fractional differential equations with subdiffusion and superdiffusion," Comput. Math. Appl. **62**, 855–875 (2011).

[38] B. J. West, *Fractional Calculus View of Complexity: Tomorrow's Science*, Chap. 3 (Taylor & Francis Group, Boca Raton, 2016).

[39] S. Holm and S. P. Näsholm, "A causal and fractional all-frequency wave equation for lossy media," J. Acoust. Soc. Am. **130**, 2195–2202 (2011).

[40] S. P. Näsholm and S. Holm, "Linking multiple relaxation, power-law attenuation, and fractional wave equations," J. Acoust. Soc. Am. **130**, 3038–3045 (2011).

[41] D. T. Blackstock, *Fundamentals of Physical Acoustics*, Chap. 6 (John Wiley & Sons, New York, 2000).

[42] J. F. Kelly, R. J. McGough, and M. M. Meerschaert, "Analytical time-domain green's functions for power-law media," J. Acoust. Soc. Am. **124**, 2861–2872 (2008).

[43] F. Mainardi, "The fundamental solutions for the fractional diffusion-wave equation," Appl. Math. Lett. **9**, 23–28 (1996).

[44] A. A. Tateishi, H. V. Ribeiro, and E. K. Lenzi, "The role of fractional time-derivative operators on anomalous diffusion," Front. Phys. **5**, 52 (2017).

[45] T. A. M. Langlands, B. Henry, and S. Wearne, "Fractional cable equation models for anomalous electrodiffusion in nerve cells: infinite domain solutions," J. Math. Biol. **59**, 761 (2009).

[46] E. Scalas, R. Gorenflo, and F. Mainardi, "Fractional calculus and continuous-time finance," Physica A **284**, 376–384 (2000).

[47] S. Arshad, A. Sohail, and K. Maqbool, "Nonlinear shallow water waves: A fractional order approach," Alex. Eng. J. **55**, 525–532 (2016).

[48] G. B. Whitham, "Variational methods and applications to water waves," Proc. Royal Soc. A **299**, 6–25 (1967).

[49] F. Dias, A. Dyachenko, and V. Zakharov, "Theory of weakly damped free-surface flows: A new formulation based on potential flow solutions," Phys. Lett. **372**, 1297–1302 (2008).

[50] G. D. Meegan, M. F. Hamilton, Yu. A. Il'inskii, and E. A. Zabolotskaya, "Nonlinear Stonely and Scholte waves," J. Acoust. Soc. Am. **106**, 1712–1723 (October 1999).

[51] B. E. Simon, J. M. Cormack, and M. F. Hamilton, "Evolution equations for nonlinear Lucassen waves," Proc. Meet. Acoust. **36**, 045001 (2019).

[52] M. F. Hamilton, "Effective Gol'dberg number for diverging waves," J. Acoust. Soc. Am. **140**, 4419–4427 (2016).

[53] J. M. Cormack and M. F. Hamilton, "Overturning of nonlinear compressional and shear waves subject to power-law attenuation or relaxation," Wave Motion **85**, 18–33 (2019).

[54] T. T. Hormel, S. Q. Kurihara, M. K. Brennan, M. C. Wozniak, and R. Parthasarathy, "Measuring lipid membrane viscosity using rotational and translational probe diffusion," Phys. Rev. Lett. **112**, 188101 (May 2014).

[55] C. C. Pugh, *Real Mathematical Analysis*, 2nd ed., Chap. 5 (Springer International Publishing AG, Switzerland, 2015).

[56] P. W. Hammerton and D. G. Crighton, "Overturning of nonlinear acoustic waves. Part 1: A general method," J. Fluid Mech. **252**, 585–599 (1993).

[57] P. W. Hammerton and D. G. Crighton, "Overturning of nonlinear acoustic waves. Part 2: Relaxing gas dynamics," J. Fluid Mech. **252**, 601–615 (1993).

[58] D. T. Blackstock, "History of nonlinear acoustics: 1750s–1930s," Chap. 1 in *Nonlinear Acoustics*, M. F. Hamilton and D. T. Blackstock, eds. (Acoustical Society of America, New York, 2008).

[59] J. H. Ginsberg and M. F. Hamilton, "Computational methods," Chap. 11 in *Nonlinear Acoustics*, M. F. Hamilton and D. T. Blackstock, eds. (Acoustical Society of America, New York, 2008).

[60] A. Kadem and D. Baleanu, "Solution of a fractional transport equation by using the generalized quadratic form," Commun. Nonlinear Sci. Numer. Simul. **16**, 3011–3014 (2011).

[61] D. A. Benson, S. W. Wheatcraft, and M. M. Meerschaert, "Application of a fractional advection–dispersion equation," Water Resour. Res. **36**, 1403–1412 (2000).

[62] S. Momani, "An algorithm for solving the fractional convection–diffusion equation with nonlinear source term," Commun. Nonlinear Sci. Numer. Simul. **12**, 1283–1290 (2007).

[63] D. T. Blackstock, M. F. Hamilton, and A. D. Pierce, "Progressive waves in lossless and lossy fluids," Chap. 4 in *Nonlinear Acoustics*, M. F. Hamilton and D. T. Blackstock, eds. (Acoustical Society of America, New York, 2008).

[64] S. Hamdi, W. E. Schiesser, and G. W. Griffiths, "Method of lines," Scholarpedia **2**, 2859 (2007). Revision #124335.

[65] E. Fehlberg, "Low-order classical Runge-Kutta formulas with step-size control and their application to some heat-transfer problems," Tech. Rep. TR R-315, NASA, 1969.

[66] J. C. Butcher, "Coefficients for the study of Runge-Kutta integration processes," J. Aust. Math. Soc. **3**, 185–201 (1963).

[67] U. M. Ascher, R. M. M. Mattheij, and R. D. Russell, *Numerical Solution of Boundary Value Problems for Ordinary Differential Equations* (Prentice-Hall, Englewood Cliffs, New Jersey, 1988).

[68] R. W. Hamming, *Numerical Methods for Scientists and Engineers*, 2nd ed. (Dover Publications, Inc., New York, 1986).

[69] J. Liu, G. A. Pope, and K. Sepehrnoori, "A high-resolution finite-difference scheme for nonuniform grids," Appl. Math. Model. **19**, 162–172 (1995).

[70] J. Crank and P. Nicolson, "A practical method for numerical evaluation of solutions of partial differential equations of the heat-conduction type," Math. Proc. Camb. Philos. Soc. **43**, 50–67 (1947).

[71] I. Gel'fand and G. Shilov, *Generalized Functions*, Vol. 1 (Academic Press, New York, 1964).

[72] J. Lubliner and P. Papadopoulos, *Introduction to Solid Mechanics*, App. A: Singularity Functions (Springer Science+Business Media, New York, 2014).

[73] S. S. Kashcheeva, O. A. Sapozhnikov, V. A. Khokhlova, M. A. Averkiou, and L. A. Crum, "Nonlinear distortion and attenuation of intense acoustic waves in lossy media obeying a frequency power law," Acoust. Phys. **46**, 211–219 (2000).

Vita

Blake Elliott Simon was born in Coppell, Texas on 28 November 1995. He studied mechanical engineering at The University of Texas in Austin as an undergraduate. During this time he worked at the Applied Research Laboratories at UT Austin where he acquired an interest in the science of acoustics. After completing his Bachelor of Science degree in 2018, Blake began graduate studies at UT Austin in the Department of Mechanical Engineering with a focus on acoustics. Blake's passion for acoustics extends beyond the classroom; he enjoys music theory, speaker design, playing guitar, and listening to country and blues music.

Electronic mail: blakesimon8@utexas.edu